Fabricating van der Waals Heterostructures

Justin Boddison-Chouinard

A thesis submitted in partial fulfillment
of the requirements for the degree of

MASTER OF SCIENCE

in Physics

Department of Physics
Faculty of Science
University of Ottawa

Fabricating van der Waals heterostructures

Justin Boddison-Chouinard

Abstract

The isolation of single layer graphene in 2004 by Geim and Novoselov introduced a method that researchers could extend to other van der Waals materials. Interesting and new properties arise when we reduce a crystal to two dimensions where they are often different from their bulk counterpart. Due to the van der Waals bonding between layers, these single sheets of crystal can be combined and stacked with different sheets to create novel materials.

With the goal to study the interesting physics associated to these stacks, the focus of this work is on the fabrication and characterization of van der Waals heterostructures. In this work, we first present a brief history of 2D materials, the fabrication of heterostructures, and the various tools used to characterize these materials. We then give a description of the custom-built instrument that was used to assemble various 2D heterostructures followed by the findings associated with the optimization of the cleanliness of the stack's interface and surface. Finally, we discuss the results related to the twisting of adjacent layers of stacked MoS_2 and its relation to the interlayer coupling between said layers.

Acknowledgments

I would like to especially thank Professor Adina Luican-Mayer for her support, encouragement and guidance over the past couple years. This thesis would not have been made possible without her assistance.

I would also like to thank all the other students that have been part of Prof. Luican-Mayer's group throughout the years. Namely Ryan Plumadore for being a much appreciated sounding board in the many discussions we had together, Rouzbeh Majidi for his help in the early fabrication stages of the transfer setup, Andrew Nagarajah for his help in determining a functional recipe for the stamping technique, and Emmanuelle Launay for producing many beautiful AFM images.

A very special thank you to Tony Olivieri for spearheading so many trainings on a variety of instruments and for providing insightful tips and tricks.

I would like to thank Lukasz Andrzejewski for providing his expertise in the electronics department of the transfer setup as well as the Godin Lab for sharing the recipe and assisting in the fabrication of the PDMS stamps.

For allowing to use their Raman setups which were used to study the heterostructures, I would like to thank both the Fabio Variola Surface Nanoengineering Lab and the Centre for Catalysis Research and Innovation.

Finally, thank you to my family and friends for their unconditional support during this time. A special thank you to my parents for always nurturing my passion for mathematics and physics.

Un tout dernier merci à Émilie Loiselle.

August 2018

Contents

List of Figures

List of Tables

Chapter 1

Introduction

1.1 2D Materials

Research in two-dimensional materials really began to bloom after a technique was developed by Andre Geim and Konstantin Novoselov in 2004 which would enable the isolation of graphene.[1] Demonstrating superior properties such as electrical and mechanical properties,[2,3] graphene quickly became a topic of interest across a multitude of research fields[4–10] where it was seen to be the material of the future. With the first isolation of graphene, this quick and reproducible technique paved the way for researchers to begin the study of the broader family of 2D materials.

Graphene is the most known and most commonly studied 2D material. It comes from graphite, a three dimensional crystal where in plane, atoms are held together by strong sp^2 covalent bonds and out-of-plane, the layers are held together by weak van der Waals forces. These weak van der Waals forces are what allow us to easily cleave the graphite and reduce it down to a single layer – graphene. The basis for 2D materials is that they possess this same bonding scheme; strong covalent intralayer bonding and weak van der Waals interlayer coupling. For this reason, 2D materials are also known as van der Waals materials.

The family of 2D materials expands much further than just graphene where graphene is a semi-metal, but we can also find insulating materials (hBN[11,12]), semiconductors with various bandgaps (WS_2, ReS_2),[13] metals (VSe_2[13]) or even some that demonstrate superconducting states below particular temperatures (NbS_2[14]).[15,16] As a result of low dimensionality, the properties found in single layers are frequently distinct from their bulk counterpart. For example, MoS_2 is an indirect band gap semiconductor in its bulk

form but transitions to a direct gap semiconductor when it is reduced to one layer.[17] Even though these 2D materials already cover a long list of optical and electrical properties, the fact that they are reducible to a single layer expands this list even further.

As this family of 2D materials is quite large and essentially covers all possible properties, interesting physics arises when you consider pairing up and stacking two materials together. Such stacks are known as van der Waals heterostructures. Due to the reduction of dimensionality, the two-dimensional sheets of material which form these van der Waals heterostructures are extremely sensitive to their surroundings. For one, this makes for interesting physics as one sheet can induce its properties into the second material by proximity,[18] but it also means that a clean interface is a necessity as impurities will play an important role.

Implementing methods of stacking such materials at a micrometer scale precision and ensuring interface cleanliness is a fundamental challenge in the field and the main topic of this work.

1.2 van der Waals Heterostructures and Device Fabrication

Just as the van der Waals bonds holding adjacent layers of two-dimensional materials together can be broken, they can also be put back together. However, novel 2D materials can be created by re-assembling the layers from the initial material in a different stacking orientation or by mixing and matching layers of different crystals.

The first reason for creating heterostructures came when Dean *et al.* showed that devices made by placing graphene on hBN have carrier mobilities that are almost an order of magnitude better than a typical device made on SiO_2.[19] Later, Wang *et al.* showed that the performance of these devices can be further improved by encapsulating it with another hBN flake.[20]

Encapsulation of materials can not only boost device performance, but it can also prevent degradation of materials that are not inert in air such as black phosphorus.[21,22]

van der Waals heterostructures also have great potential for photovoltaic applications.

As an example, Yu *et al.* demonstrated highly efficient photocurrent generation in a graphene-MoS_2-graphene heterostructure.[23] Furthermore, as some of these two-dimensional materials are inherently n-doped while others are p-doped, by placing them together we can create atomically sharp p-n junctions.[24] These devices are extremely efficient in carrier separation and could act as a building block for a wide range of optoelectronic applications.

Another exciting reason for creating van der Waals heterostructures is the possibility of inducing properties such as strong spin-orbit coupling, charge density waves, or superconductivity found in one material into the other by proximity and studying its effects.[18]

To assemble these novel materials, two common approaches can be taken: a growth approach or mechanical stacking. Growth methods include methods such as chemical vapor deposition (CVD), van der Waals epitaxy, and physical vapor deposition (PVD) and have been used so far to create a variety of vertical[25–27] and lateral heterostructures.[28,29] These growing methods are also promising techniques as they offer a method for producing van der Waals heterostructures at an industrial scale. However, a relatively high density of defects are found in these crystals leading to highly variable electronic properties.[30]

Mechanical stacking on the other hand is more versatile and does not face limitations such as lattice mismatching, an impasse some growth methods cannot overcome. Compared to growth methods, mechanical stacking utilizes high-quality crystals which allow us to study the properties of pristine heterostructures. For this reason, mechanical stacking is often used in research laboratories and is continuously looking for improvement. Here we will present the steps leading up to mechanical stacking and its various techniques.

Mechanical Exfoliation: To isolate these materials on a particular substrate, one typically uses a technique that was first proposed by Andre Geim and Konstantin Novoselov[1,2] called mechanical exfoliation. This technique was first used to obtain graphene starting from highly oriented pyrolytic graphite (HOPG) by simply using strips of adhesive tape and peeling back layers of graphene. The normal force applied to the HOPG when peeling away the adhesive tape is strong enough to overcome the van der Waals attraction between adjacent layers of graphene hence separating the graphite in two thinner graphite crystals. After much repetition, the graphitic layers become thin enough that you are left with a single layer, graphene.

Just like graphite, transition metal dichalcogenides (TMDC), a class of material that forms a big part of the 2D material family, consists of two-dimensional sheets of atoms weakly bound together by van der Waals forces. This means that we can apply the mechanical exfoliation method to isolate single layers of the crystal, also known as a monolayer, just as we did for graphene.

Mechanical exfoliation protocol: We first start with commercial silicon (Si) wafer with a 285nm oxide layer (Nova Electronic Materials). The wafer is then cut using a diamond scribe into 1cm x 1cm individual substrates. The substrates are placed in an acetone bath and cleaned by ultrasonication, followed by an isopropanol (IPA) rinse to wash off the acetone and are immediately dried off with the use of a nitrogen (N_2) gun. Finally, the substrates are placed on a hot plate for approximately 10 minutes and heated to 110°C to clean off any remaining contaminants or accumulated water vapor. Once the substrates have cooled off to room temperature, we can proceed to the mechanical exfoliation of the crystal. First, a small piece of crystal is taken from the mother crystal and placed on a piece of tape. Another piece of tape is applied onto the crystal/tape and peeled away which then divides the initial crystal into two thinner crystals. We repeat this process until the crystal on the tape appears to be of the desired thickness. The tape is then pressed onto the freshly cooled off substrate such that the crystal is sandwiched between the tape and substrate. When we peel back the tape, exfoliated crystal of various thicknesses will be left on the substrate. The substrate is then placed in another acetone bath, rinsed with IPA, and dried off with N_2 to remove any adhesive tape residues that may have been left behind. The entire procedure is done in a clean room environment (CRPuO facilities) to limit any air contamination.

1.2.1 Mechanical Assembly

The goal of mechanical stacking is to precisely place a crystal at a desired location. This could either mean placing a crystal on a pre-patterned substrate or onto another crystal, creating a stack. In its most general form, a first substrate, the accepting substrate or bottom substrate, is prepared and placed under an optical microscope. A second substrate, the substrate which supports the crystal to be transferred, is also placed under the optical microscope. This substrate is referred to as the top substrate and it must meet certain requirements: it must be transparent and sacrificial. The optical microscope is used to align the crystal from the top substrate with the target substrate,

hence the need for a transparent substrate. Once proper alignment is made, the two substrates can be brought into contact. Usually, the top substrate is not intended to be part of the stack and therefore, a cleaning step is required to remove it.

There are many methods that allow us to create such stacks. Here, we will introduce some of these methods and go in detail on the methods that we have experimented.

The Wedging Method: The wedging method[31] was first demonstrated in 2010 and utilizes the hydrophobic effect. In this technique, a first crystal is mechanically exfoliated on a Si/SiO_2 substrate and placed at the bottom of a water bath with the crystal facing upwards. A second substrate is prepared by exfoliating crystal on a plasma oxidized Si/SiO_2 substrate. This hydrophilic substrate is then dipped in a hydrophobic solution of cellulose acetate butyrate which forms a polymer film. Afterwards, the substrate is dipped in the water bath at an angle of 30° resulting in the hydrophobic polymer to detach from the substrate while lifting off the underlying flakes. The Si/SiO_2 substrate will sink to the bottom of the bath while the polymer and flakes will remain afloat. A sewing needle is attached to a set of micromanipulators and is brought into contact with the polymer. These micromanipulators will allow us to adjust the XY position of the polymer. By using a syringe, one can pump out the water from the bath and hence slowly bring the polymer closer to the bottom substrate while maintaining proper alignment. Eventually, the flake and polymer will contact the bottom flake where the final step is to wash away the polymer.

The Bipolymer Technique: In the same year as the wedging method was introduced, another mechanical transfer method was demonstrated where the goal was to transfer graphene onto a cleaner substrate:[19] hexagonal boron nitride (hBN). Fabrication of these stacks began with the exfoliation of hBN on a Si/SiO_2 substrate. Graphene was mechanically exfoliated on a second substrate that had previously been spin-coated with a water-soluble layer of Mitsubishi Rayon aquaSAVE followed by a layer of poly(methyl methacrylate) (PMMA). The substrate with the graphene and polymer stack was placed in a bath of deionized water which caused the water-soluble layer to dissolve and the PMMA/graphene to float. The PMMA/graphene was then picked up, fixed to a glass slide, and placed in a set of micromanipulators such that the graphene flake is facing the hBN flake. Using a microscope, one can then bring the two flakes into contact. Once contact is made, the substrate is heated to 110°C to ensure proper adhesion between the PMMA and the bottom substrate as well as to evaporate any water that may have been

adsorbed to the surface of either flake. Finally, the PMMA is washed away by cleaning it in acetone.

PMMA-PVA Technique

The following year (2011), the same group that developed the bi-polymer technique made a small adjustment to their transfer method.[32] In the previous method, the group uses water to separate the two polymers and at this step there is a strong possibility of contaminating the flake. To avoid this contamination, the first layer of polymer that is spun on the substrate is a thin layer of polyvinyl alcohol (PVA). This layer allows us to mechanically peel away the PMMA film and separate it from the substrate without the use of any solvent coining it as a dry transfer method. As this is a method that we use in our lab, we will provide details associated to each step.

Bottom Substrate Preparation: A crystal is mechanically exfoliated on a freshly cleaned Si/SiO_2 substrate. This substrate is then placed under an optical microscope operating in brightfield microscopy and is examined until the desired bottom flake is found. A quality flake is usually free of large steps, optically clean and has no other defect. To ensure cleanliness, the bottom flake is usually exfoliated directly before the transfer to avoid any kind of extra contamination such as moisture.

Top Substrate Preparation: Compared to the bottom substrate, the top substrate requires more preparation. We once again start the process off with a freshly cleaned 1cm x 1cm Si/SiO_2 substrate. We place the substrate into a spin coater and apply a layer of PVA by spinning the substrate at an angular velocity of 3000rpm for the duration of one minute. The PVA used is the PVA Partall Film #10 purchased from Composites Canada. The substrate is then taken off the spin coater and placed on a hot plate to bake in air at 75°C for 5 minutes resulting in a film thickness of 450nm. Once the substrate has returned to room temperature, it is put back into the spin coater to receive an additional polymer coating. This time, we spin coat a thin film of PMMA at 1500rpm for 1 minute. The PMMA used is the 950PMMA A6 purchased from MicroChem. Once the spinning is completed, the substrate is removed from the spin coater and placed on a hot plate where it will once again bake in air at 75°C for 5 minutes resulting in PMMA thickness of 820nm.

We now mechanically exfoliate the top crystal on this polymer coated substrate. To prevent the polymer from lifting off during the mechanical exfoliation, we place extra tape on the edges of the substrate creating a tape frame. The exfoliation procedure must be done in a controlled manner and is recommended to do immediately after the spin coating. Since the polymer layers are so thin, the mechanical exfoliation may cause them to rip. Once the mechanical exfoliation is completed, we can manually peel off the PMMA layer by carefully lifting the tape frame and separating it from the PVA. Once again, a tearing of the PMMA layer may occur during this step.

The tape frame and polymer is now placed on a machined support (a piece of plastic with a hole in the middle) such that the crystal is face down and located in the hole. This allows us to place the support under an optical microscope and optically search for a transferable top flake. This step can take longer than usual for many reasons. The first being that the crystal is no longer on a Si/SiO_2 substrate with a 285nm oxide layer but is instead on PMMA which results in reduced contrast. Secondly, as the PMMA is a thin layer of polymer and is freely hanging in the hole of the machined support, the PMMA has a wavy profile and demands a constant adjustment of the focus. Nonetheless, it is still possible to find monolayers of the crystals and to optically deduce cleanliness.

When the top flake has been determined, a small washer (0.5mm radius) is placed on the polymer such that it is surrounding this flake. Next a glass slide is pressed onto the polymer and stuck to the tape frame. The goal of the washer is to create a bump in the PMMA for the area in which the flake resides.

The resulting top substrates is made of a glass slide, followed by a washer, then a thin PMMA film and finally the exfoliated crystal.

Transfer Procedure: The bottom substrate is placed on the bottom sample holder with the crystal facing upwards. The glass slide is placed in the top sample holder such that the top crystal is facing downwards. Starting at a lower magnification, the bottom substrate is brought into focus and the desired flake is centered. The top substrate is slowly lowered until it enters the depth of field of the objective. At this point we can adjust the X and Y coordinates of the top flake so that it is centered and appears aligned with the bottom flake. By switching over to a higher magnification objective, we may properly align the position of the top flake and continue to slowly lower the top substrate. Eventually, the PMMA will come in contact with the bottom substrate,

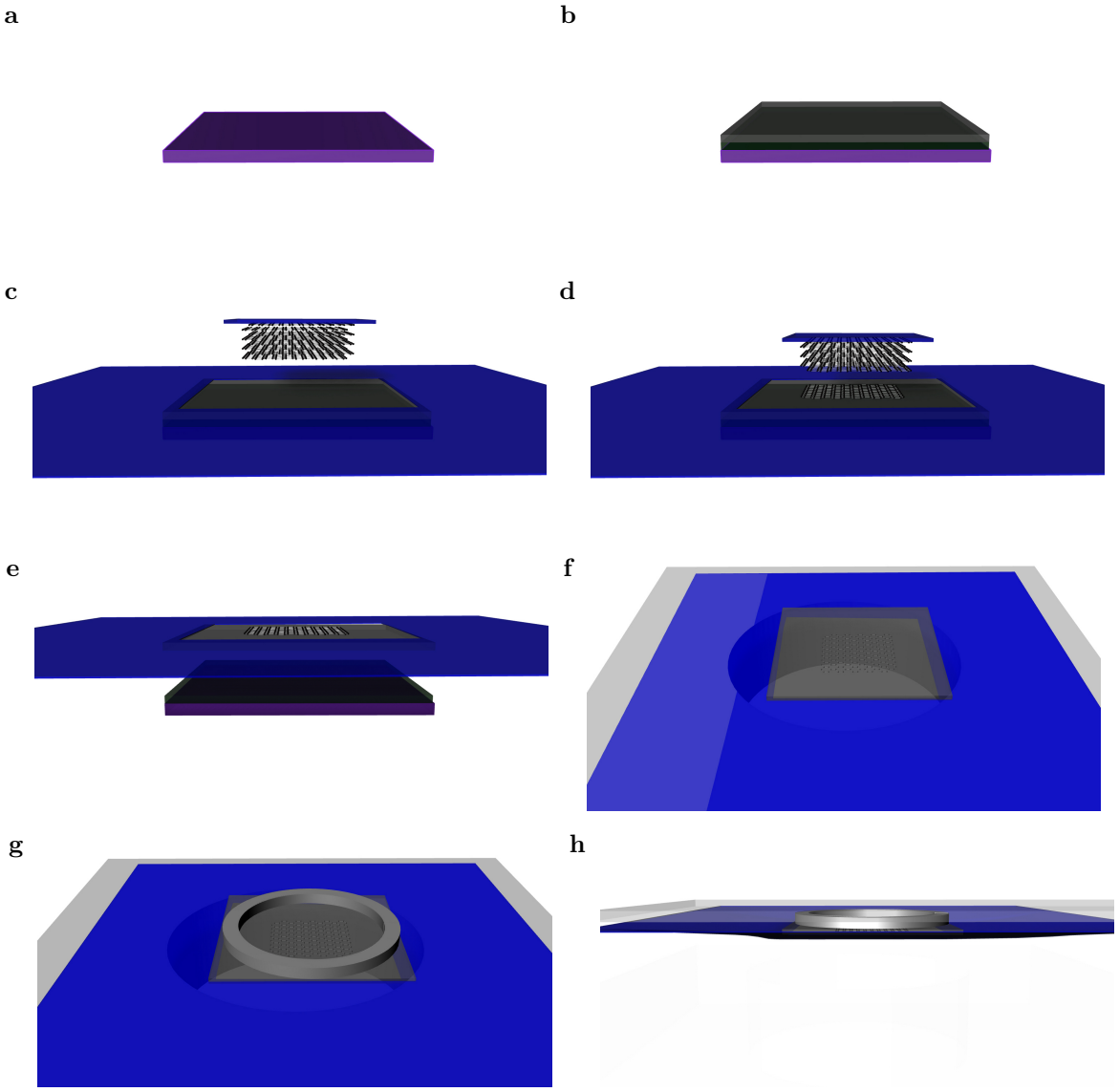

Figure 1.1: PMMA-PVA top substrate preparation. **a)** A bare Si/SiO_2 substrate **(b)** is first spin coated with PVA followed by PMMA. **c)** A tape frame is placed on the substrate to hold down the polymers **(d)** during the mechanical exfoliation step. **e)** The PMMA layer with exfoliated crystal is manually peeled away from the remaining susbtrate. **f)** It is inverted and placed on a machined support where we can use an optical microscope to search for a desirable flake. **g)** A washer is placed suched that the desired flake apears in the center of the washer and finally **h)** a glass slide is adhered to the tape frame.

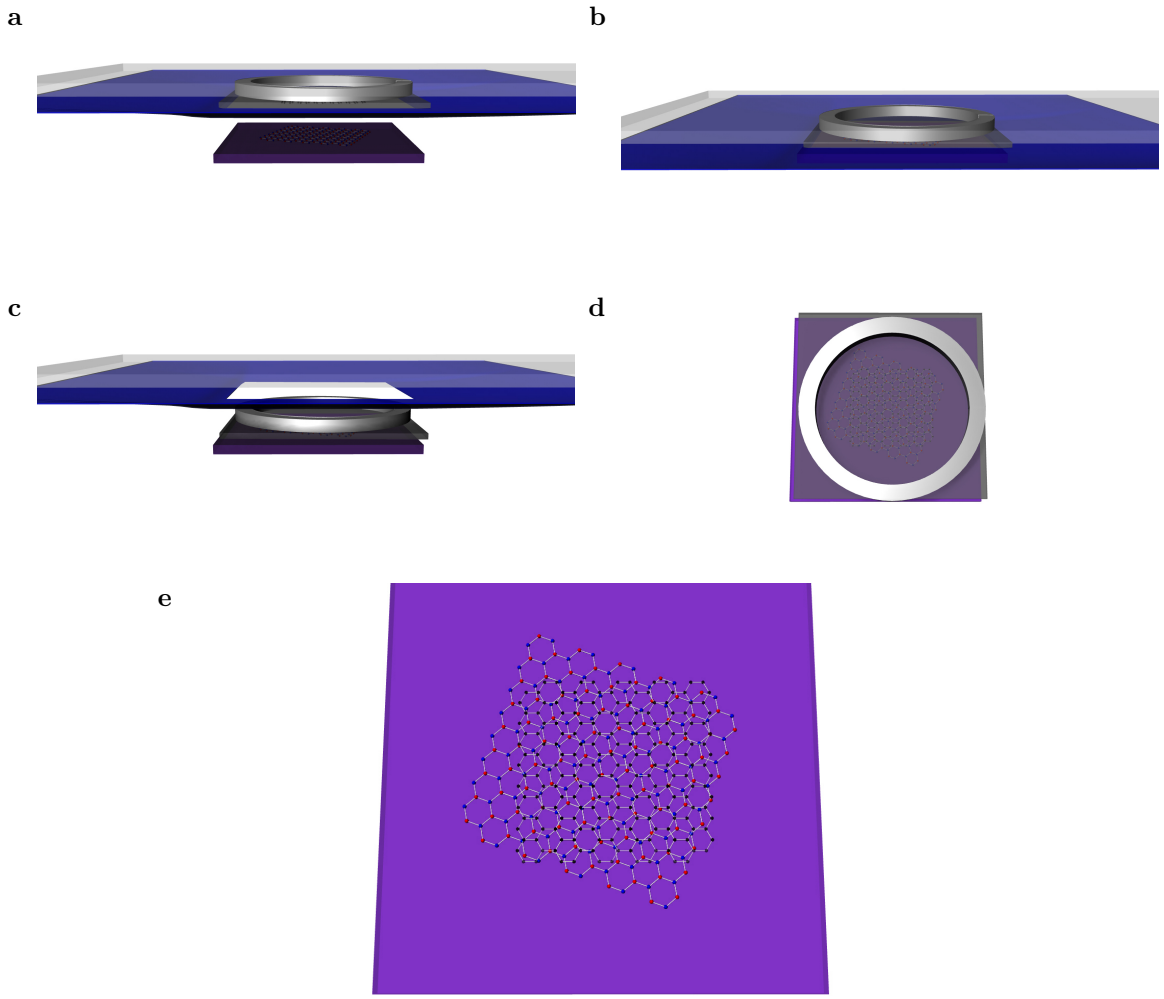

Figure 1.2: PMMA-PVA transfer procedure. **a)** The bottom and top substrates are placed under a microscope and aligned. **b)** The two are then brought into contact and the bottom stage is heated to 75°C. **c)** The top substrate is retracted which results in **(d)** the PMMA to detach from the glass slide. **e)** The washer is removed and the substrate is placed into an acetone bath to wash away the PMMA.

usually beginning from the outside of the inner radius of the washer due to the protrusion caused by the washer. This contact is noticeable by a change in color going from purple to green. Eventually the entire polymer will contact the substrate where we then turn on the heating element to 75°C causing the polymer to adhere to the bottom substrate. We can then either lower the bottom stage or raise the top stage which will cause the bottom substrate to remain fixed to the top substrate. The glass slide is then removed from the transfer setup and brought to the clean room where it will be prepared for the cleaning procedure.

Cleaning Procedure: A surgical blade is used to cut out the contour of the bottom

substrate which results in the PMMA detaching from the tape frame hence releasing the bottom substrate. As acetone is PMMA's solvent, the substrate is placed in an acetone bath for approximately 30 minutes. The acetone can be heated to 55°C which is known to provide better cleaning. An isopropanol (IPA) rinse immediately follows the acetone bath which is then dried using a N_2 gun.

Stamping Technique

Bottom Substrate Preparation: The bottom substrate is prepared in the exact same way as it would for the previous technique, that is by mechanically exfoliating a crystal on a Si/SiO_2 substrate.

Top Substrate Preparation: The procedure for preparing the top substrate begins with a freshly cleaned 1cm x 1cm Si/SiO_2 substrate. This substrate is placed into the spin coater where we coat it with a layer of polypropylene carbonate (PPC). The PPC is bought from Sigma-Aldrich in its crystal form and is mixed in anisole (3 parts PPC mixed in 20 parts anisole). The PPC is mixed overnight in a stirrer. By spinning the substrate at 3000rpm for 1 minute results in a polymer film measuring approximately 1160nm in thickness. Once the spinning is completed, the substrate is placed on a hot plate to bake in air for 5 minutes at 75°C.

Just like in the last method, a tape frame is placed around the edges of the substrate before moving on to the mechanical exfoliation step. With the tape frame in place, we can proceed to mechanically exfoliate the desired crystal on the polymer covered substrate. The substrate can then be placed under an optical microscope where we can search for the flake to transfer. The PPC thickness provides sufficient contrast such that monolayer flakes can be found (see Appendix 6.1).

Similar to the last method where we use a small washer to create a bulge between the polymer and glass, in this method we use a polydimethylsiloxane (PDMS) stamp. There are two ways of obtaining said stamp:

The first method was made from pre-made Gel-Pack. A scalpel was used to cut a 2mm x 2mm (1mm thick) square from the pre-made PDMS sheet and this square was used as the PDMS stamp.

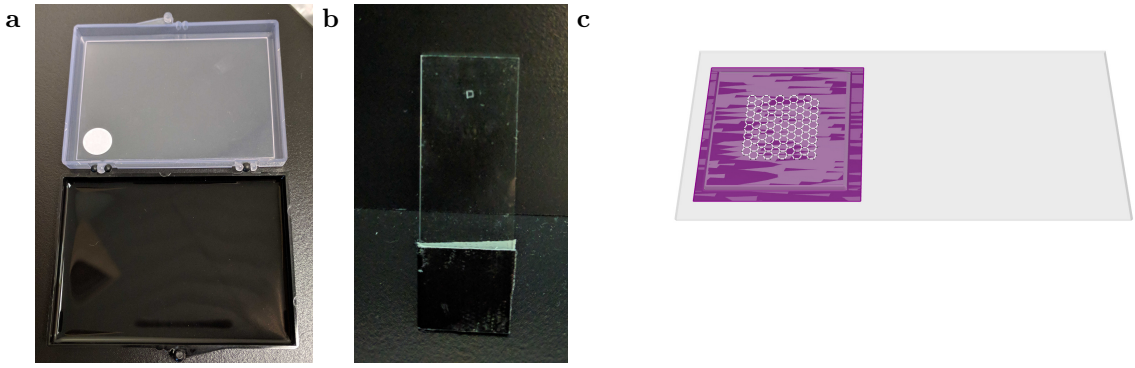

Figure 1.3: Top substrate preparation. **a)** A PDMS sheet (Gel-Pack) can be cut into a small cube and placed on a glass slide **(b)** to be used as a stamp. **c)** PPC with exfoliated crystal is picked up and placed on the stamp and glass slide.

The second method uses Sylgard 184 to make the PDMS stamps by manually mixing for 5 minutes 10 parts base and 1 part curing agent. This mixture was poured in a mold (1mm deep) and placed in a vacuum desiccator for 30 minutes. Once the mixture has degassed, the mold is placed in an oven for 2 hours. Now the cured PDMS is taken out of the mold, rinsed with IPA, then acetone, then ethanol and finally dried with a N_2 gun. This results in sheets similar to that of the Gel-Pack where we can use a scalpel to cut out similar stamps.

Now we want to bond these PDMS stamps to a glass slide otherwise they would detach during the transfer procedure. To do so, the stamps were placed on a carrier slide such that the exposed PDMS would be the side which bonds to the glass slide. The carrier slide/stamp and an additional glass slide were placed in an oxygen plasma etcher (PE-50) for 2 minutes at 50W and 0.4Torr. At the end of the cycle, the additional glass slide is pressed onto the exposed PDMS stamp causing the two to bond to each other.

The glass slide and PDMS stamp is now placed back into the oxygen plasma etcher where it undergoes the same cycle. At the end of the cycle, the PPC film is manually peeled off from the substrate and placed on the stamp such that the desired flake is located on the stamp.

The above procedures are all done in a cleanroom environment.

Transfer Procedure: The glass slide with PDMS stamp, PPC and crystal is loaded in the top substrate holder with the crystal facing the bottom stage. The bottom substrate is placed on the bottom stage where the desired flake is centered and brought into focus. The heater is turned on and raised to 100°. After having reached the desired temperature,

we lower the top manipulator whilst adjusting the position of the top flake until a corner of the stamp comes into contact with substrate which is noticeable by a change of color. As we continue to lower the top manipulator, the stamp front advances. Once this front gets close to the crystal of interest, the lowering of the stage is slowed down. After the two crystals have come into full contact, we can begin to peel back the stamp by slowly retracting the top stage. This is where the importance of the oxygen plasma etching comes into play where otherwise both the stamp and polymer would detach from the glass slide. Peeling back the stamp at this temperature results in the drop-off of the flake from the stamp to the bottom substrate.

Cleaning Procedure: Even though the polymer does not detach from the stamp, a small residue could be left behind therefore the samples are subject to the same cleaning as in the last method.

Pick-up Technique

Top Substrate Preparation: Analogous to the previous method, a PDMS stamp is bonded to a glass slide and is subject to a second oxygen plasma cycle. The next step in the preparation is to put a film of PPC on the stamp. This can be done directly by spin coating the PPC on the stamp but due to the small size of the stamp, this does not provide a uniform film. Instead, we will spin coat a film of PPC on a Si/SiO_2 substrate as we did in the last method. Again, we will put a tape frame around the substrate to pick up the polymer film and place it on the stamp once the plasma cycle is completed. If this step is completed carefully, a uniform and flat film of PPC will now be on the stamp. To obtain crystal on the stamp, certain conditions allow us to pick-up crystal from a Si/SiO_2 substrate. A substrate with exfoliated crystal is placed under the optical microscope on the bottom stage and the glass slide is inserted into the top substrate holder. The bottom stage is brought into focus and heated to 40°C. The top stage is slowly brought down until the stamp and polymer have come into complete contact with the substrate. By quickly lowering the bottom stage or raising the top stage, the crystal can be picked up.

Once the crystal is picked up, we can follow the same transfer procedure and cleaning procedure as the previous method.

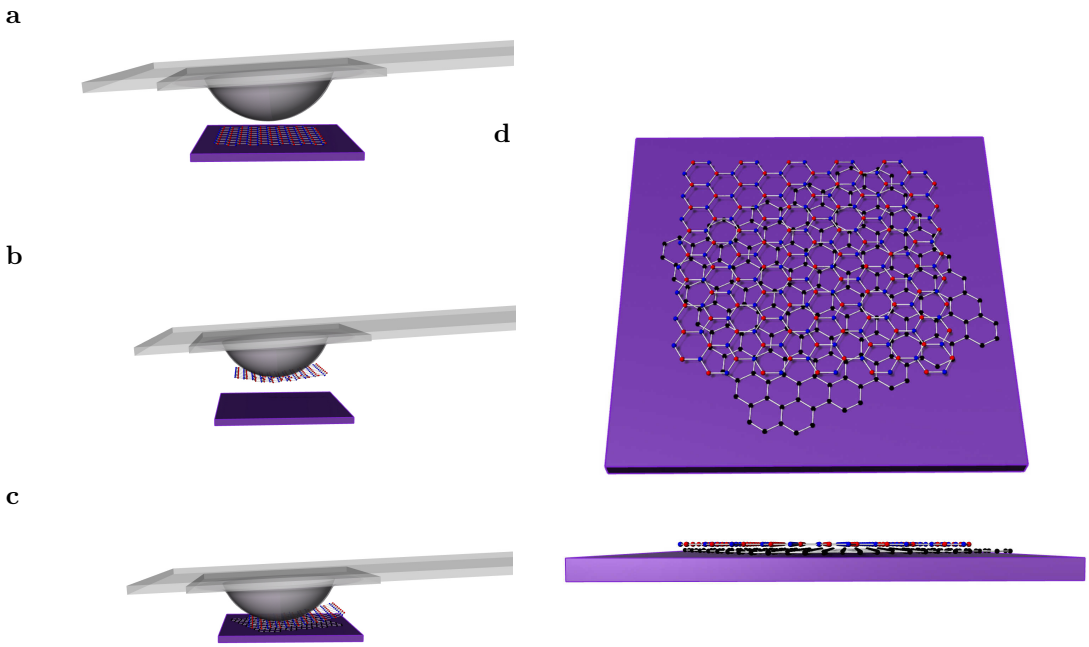

Figure 1.4: Pick-up technique. **a)** A stamp is lowered and brought into contact with an exfoliated flake. **b)**By setting the bottom substrate temperature to 40°C, the top substrate can be retracted resulting pick-up of the bottom flake. **c)** The top flake can be dropped onto another exfoliated flake by heating the bottom substrate to 100° **(d)** resulting in a stack.

Additional Remarks

In this section, I will discuss the limitations, the advantages, and the disadvantages of each method, as well as add some clarifications on the procedure.

PMMA-PVA Technique: This method involves many steps where the PMMA layer may risk tearing. Starting with the mechanical exfoliation, it was found to tear close to 75% of the time if this step was not done within a couple hours of the spin coating where it then had a near 80% success rate. In the next step, the separation of the PMMA from the PVA can sometimes fail and result in tearing of the PMMA. A last step that threatens the structural integrity of the PMMA comes when placing the washer on the polymer. The washer has a 0.5mm inner radius and we are attempting to place it around a specific flake. To do this, we must use tweezers and an optical microscope therefore, we risk perforating the PMMA and destroying the sample. This being said, the preparation of the samples can be completed but a scrupulous approach must be taken.

Another factor that affects the success rating of this method is the cleaning step. Even

though proper contact seemed to have been made when completing the transfer, washing the substrate in acetone sometimes leads to the removal of the flake along with the polymer.

However, washing PMMA off of crystals has been studied for many years as it is used as an electron beam resist, a photo-resist and a supporting layer for transferring CVD grown crystals from one substrate to another. Therefore, in addition to simple wet chemistry, many techniques are available and known for washing this polymer away.

Stamping Technique: Compared to PMMA, the PPC is a lot more durable and hardly tears during its handling. Also, the transfer process in general proves to be a lot easier to control and perform. Finally, during the cleaning procedure, as there is only a trace of polymer to wash off, this step has never resulted in a flake being washed off from the stack.

Nevertheless, this thin film of polymer has proven difficult to completely remove using simply wet chemistry. Due to the fact that the polymer is difficult to wash off, a second flake transferred onto the stack would lead to a contaminated interface.

PPC's stickiness coefficient changes depending on its temperature going from more adhesive to less adhesive as temperature increases. This is in one way an advantage because we saw that in the pick-up technique, at 40°C, PPC can pick-up the crystal whereas at temperatures above 70°C, PPC will drop off a crystal. However, heating the PPC can also bring some disadvantages. If the flake we wish to transfer is thin enough but has a fold or wrinkle along its edge, by raising the temperature, the flake will then proceed to roll in on itself (see figure 1.5). This fact greatly reduces the options for flakes as most of the time a flake will not be perfectly flat with no folds.

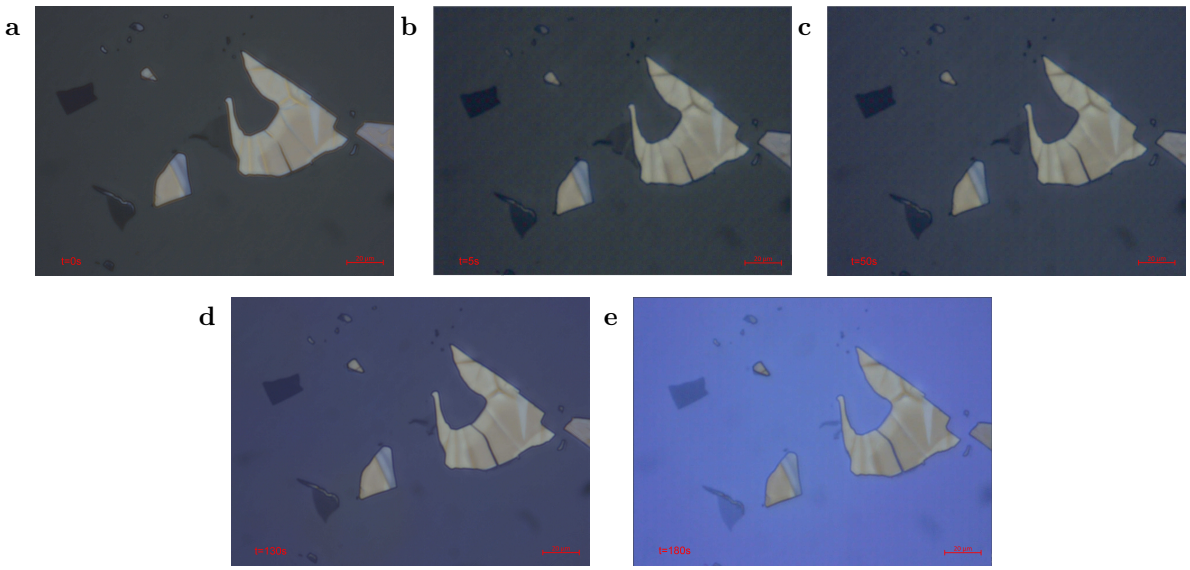

Figure 1.5: A graphene flake on a stamp that was prepared using the PPC method. The stamp is slowly brought closer to a bottom substrate that has been heated to 100°C resulting in the curling of the flake.

Pick-up Technique: As mentioned, PPC can be used to pick-up flakes under certain conditions. One of those conditions is that the temperature must be set at 40°C. A stricter condition is that thin crystals are nearly impossible to pick-up from the substrate. As monolayer crystal is usually our crystal of choice for transfers, this technique is almost rendered useless. However, any thickness of hBN can easily be picked up. This is useful because while hBN is on the stamp, it can be used to pick-up other crystals including the thinner flakes (see figure 6.8). This results in a method for picking up any thin crystal and creating a stack out of it. The limitation is that hBN must now be part of that stack.

hBN does not have be on the stamp to pick up thin flakes but we can also transfer the thin flakes onto an hBN flake using the stamping method then proceed to picking up the stack (see figure 6.9). This allows us to create stacks with hBN and a thin flake where order of the flakes does not matter.

Furthermore, with this pick-up technique, the interface between two crystals in a stack will never come in contact with a polymer which decreases the opportunity for contaminants. For example, if we wish to make a Graphene/MoS_2/hBN stack we have the following options:

Option 1: We can proceed with the stamping method or the PVA-PMMA method where

we first exfoliate graphene on a substrate. We then transfer MoS_2 onto the graphene followed by a second transfer of hBN.

Option 2: We mechanically exfoliate hBN on a susbtrate. We then pick-up the hBN flake using the pick-up technique. Then we exfoliate MoS_2 on another substrate followed by an immediate pick-up using the hBN stamp. Then we simply drop off the MoS_2/hBN stack onto a previously exfoliated graphene flake.

In the first option, the graphene/MoS_2 interface would be clean however, because the MoS_2 came in contact with polymer, the MoS_2/hBN interface may be contaminated. This would not be the case for option 2.

Examples of transfers using the various methods can be found in Appendix 6.2.

1.2.2 Device Fabrication

2D materials alone as well as van der Waals heterostructures have great potential when it comes to devices. Therefore, electrical contacts need to be placed on these 2D materials to transform them into devices. To that end, spin-coating, electron-beam lithography, and electron-beam metal evaporation are the main instruments used to pattern and realise these electrical contacts. A complete protocol can be found in Appendix 6.3.

1.3 Characterization Techniques

Many characterization techniques are used throughout this work to locate particular flakes, determine their thickness as well as to evaluate their cleanliness.

1.3.1 Optical Microscopy

Flakes resulting from mechanical exfoliation typically occupy an area of $100\mu m^2$ and the optical microscope provides a quick method for seeing these exfoliated flakes. We typically use the optical microscope in two modes, reflected brightfield and reflected darkfield, where the former can provide information on the flake's thickness,[33] and the latter has the ability to expose adhesive tape residues or inconsistencies in the crystal. To understand how brightfield microscopy operated in reflection mode can give the flake's

thickness, we can calculate the intensity of the light reflected from the crystal and see how it changes as a function of flake thickness[33] (see 6.1). As an example, figure 1.6 shows how the peak in the reflected spectrum of graphite shifts from low wavelength (purple) to a higher wavelength (blue-green) when going from a single layer to a relatively thick piece of graphite. This corresponds well with what is seen in the optical microscope where monolayer graphene is purple, few-layer graphene is blue, and thick graphite is more green or yellow (see figure Appendix 1.7).

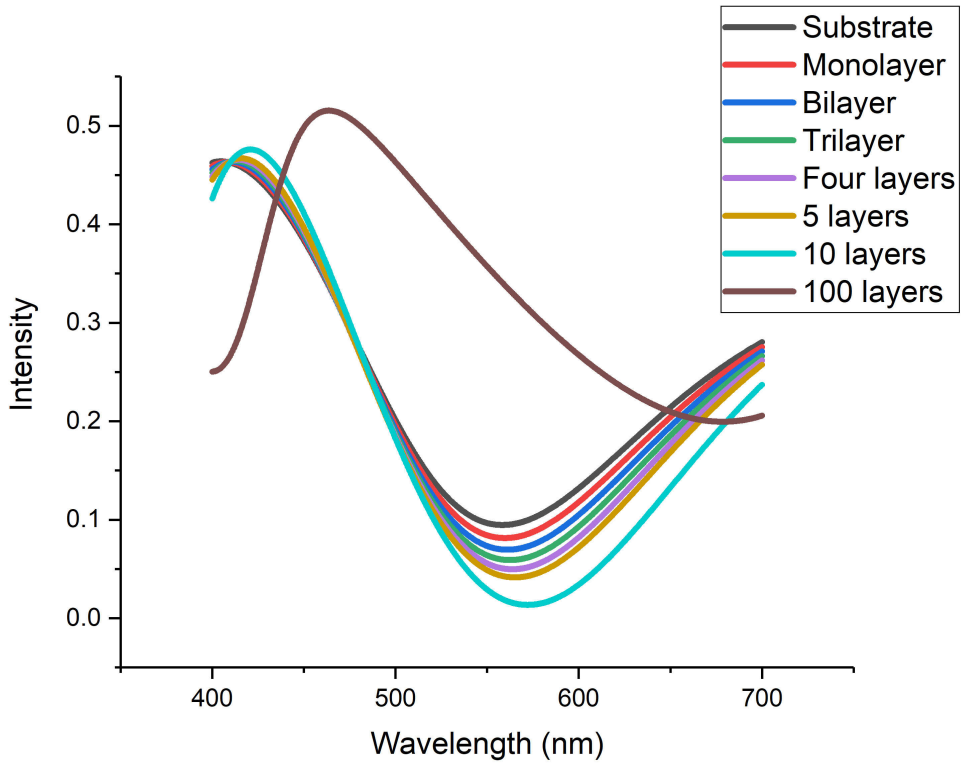

Figure 1.6: A plot of the intensity of the reflected light for a bare Si/SiO_2 (285nm) substrate and various layers of graphene.

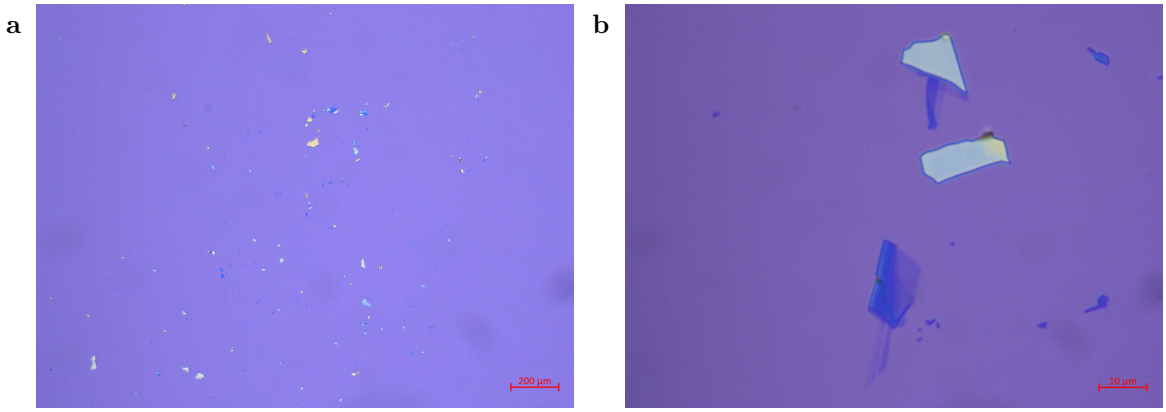

Figure 1.7: Graphene mechanically exfoliated on Si/SiO_2 substrate as seen from an optical microscope under a magnification of **a)** 5X and **b)** 100X.

1.3.2 Atomic Force Microscopy

Optical microscopy presents a way to quickly scan over an entire substrate and estimate the thickness and cleanliness of the exfoliated crystals. For a more precise measurement of both the thickness and the surface roughness, an atomic force microscope (AFM) can be used.

The AFM was invented in 1986[34] by Binnig *et al.* not long after the invention of the scanning tunneling microscope (STM). The STM which relies on the principle of quantum tunneling,[35] can only be used for analyzing conductive samples. With the goal of addressing this limitation, the AFM was invented to be enable the analysis of the surface of any solid material.

The basic principle of the AFM works by scanning a sharp tip over a surface and detecting the deflection of a cantilever; a deflection determined by the interacting forces between the sample and the AFM tip. The shape and size of the AFM tip varies depending on the application, but a typical tip is made by controlled etching of silicon into a pyramid shape which results in a tip radius of approximately 15nm. These sharp tips are mounted on a highly reflective cantilever which again can vary in shape and material. The cantilever and the tip are essentially the AFM sensor. By shinning a laser on the reflective cantilever, a position sensitive detector (PSD) consisting of an array of photodiodes picks up the reflected signal and can detect any deflection that may occur. This deflection is regulated by the interacting forces between the tip and the sample.

These tip-sample interactions can be categorized in two types of interactions: repulsive and attractive. Away from the sample, van der Waals forces dominate resulting in an overall attractive force whereas near or in-contact with the sample, repulsive forces take over. Depending on what is being studied, the user can probe the surface in either one of these regimes, but the approach is different. There exists three major modes of operation as to how one scans the surface and interacts with the sample: contact mode, tapping mode, and non-contact mode.

Contact mode: In contact mode, the tip is brought into direct contact with the surface of the sample. The tip will approach the sample until it senses a specified repulsive force. Once the tip begins to scan the surface of the sample, a feedback loop maintains the force constant by adjusting the vertical position of the tip/sample. This adjustment is registered and is interpreted as the height topography of the sample. Using the AFM in contact mode can lead to high resolution images, however, as the tip is in immediate contact with the sample, it can also result in contamination and destruction of the sample as well as a short tip life.

Non-contact mode: In non-contact mode, an actuator is used to vibrate the cantilever (in the z-direction) just above its resonant frequency near the surface of the sample with a vibration amplitude of a few nanometers. As the tip further approaches the sample, the force between the sample and tip will shift the resonant frequency of the cantilever. This shift in frequency can be detected by monitoring the amplitude of the cantilever vibration with the laser and a PSD. By scanning the tip over the sample, the AFM will adjust the tip-sample separation to keep the oscillation amplitude constant and will result in a height map of the sample.

Tapping-mode: A third method exists where the tip is once again driven near its resonant frequency but at a much higher amplitude (typically between 20 and 100nm) and actually comes into contact with the surface on each oscillation.[36] The intermittent contact with the surface causes a change in the oscillation amplitude. As the tip scans over the sample, the sample-tip distance can be adjusted to maintain the oscillation amplitude at a constant set point generating a topographic image of the sample.

In this work, the AFM was used in non-contact or tapping mode to protect the samples we studied. Furthermore, it was used to confirm the thicknesses of multiple flakes as well as their cleanliness. To evaluate the cleanliness of our samples, we calculate the

arithmetic roughness R_a and root mean squared roughness R_q.

$$R_a = \frac{1}{n}\sum_{i=1}^{n}|z_i| \qquad R_q = \sqrt{\frac{1}{n}\sum_{i=1}^{n}z_i^2} \tag{1.1}$$

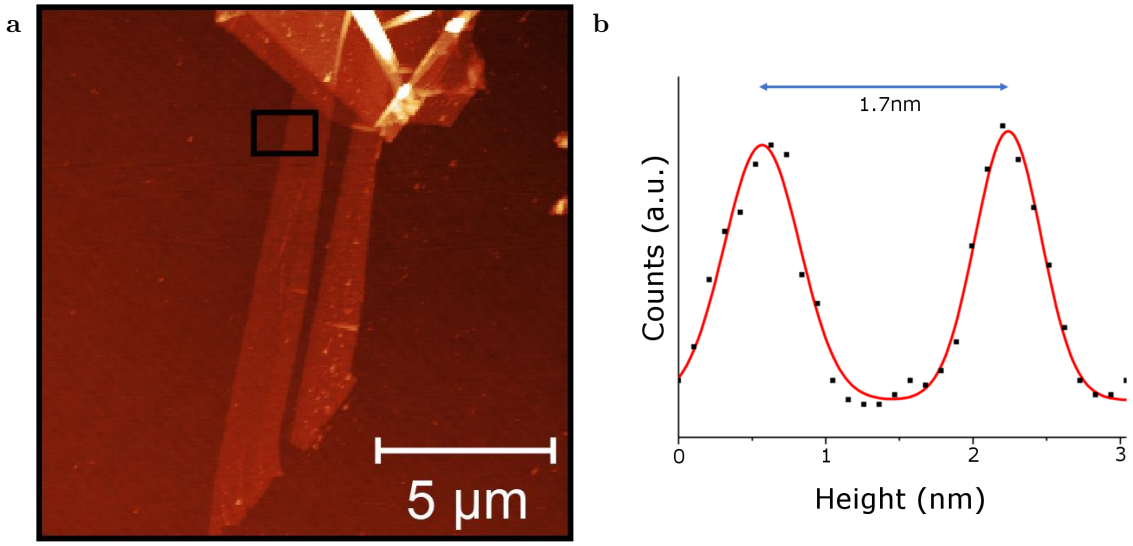

Figure 1.8: **a)** AFM image of the graphene flake from Figure 1.7b. **b)** A height histogram of the area denoted by the box in **(a)** fitted with a double Gaussian indicating a step height of 1.7nm.

The two AFMs used during this project are the Park NX10 operated in non-contact mode and the Bruker – Dimension Icon which was operated in tapping-mode.

1.3.3 Raman Spectroscopy

Raman spectroscopy is another powerful characterization tool that offers a quick, reliable, and non-destructive method for analyzing crystals. This tool can be used to distinguish various materials as each crystal provides a unique fingerprint. The spectrum does not only provide information on the constituents of the crystal, but can also give information about various other parameters such as the number of layers,[37–39] strain effects,[40–42] electron-phonon coupling,[43,44] interlayer coupling,[45–48] and doping.[49]

In Raman spectroscopy, a monochromatic light source illuminates a sample and the user observes the scattered light. When light interacts with a solid, an incident photon can create an electron-hole pair. This electron-hole pair will then interact with the

crystal lattice through a scattering process. Elastic scattering dominates the scattering processes and in this case, the electron-hole pair will recombine to emit a photon with equal energy as the incident photon. This is known as Rayleigh scattering. However, inelastic scattering processes may occur. In these cases, the interaction between the lattice and the electron-hole pair can either lead to the creation or annihilation of a phonon followed by the recombination of the electron-hole pair and emission of a photon. In the case where a phonon is created, the emitted photon will be red-shifted. If a phonon is annihilated, the emitted photon will be blue-shifted. These two inelastic scattering processes are known as Stokes and anti-Stokes scattering, respectively. The three cases can be summarized by the energy conservation law

$$\hbar\omega_i = \hbar\omega_s \pm \hbar\omega_p$$

where ω_i is the frequency corresponding to the incident photon, ω_p is the frequency corresponding to the phonon and ω_s is the frequency corresponding to the scattered photon.

1.3.4 Raman Spectroscopy of Graphene

As mentioned earlier, Raman spectroscopy can be used as a quick method for identifying the number of layers of particular crystals which proves to be very useful in this work. For the case of graphene, a noticeable change in the Raman spectrum occurs when going from monolayer graphene to a bilayer structure to bulk crystal. To explain this change, let us take a look at the origin of the peaks found in the Raman spectrum of graphene and of graphite.

The unit cell of graphene contains 2 atoms and therefore has three acoustic and three optical branches in its phonon dispersion, each containing two in-plane and one out-of-plane vibrational mode. At $q = 0$ (the center of the Brillouin zone or the Γ-point), graphene has 6 normal modes where two of them are doubly degenerate (E_{2g} and E_{1u}).[50]

$$\Gamma_{vib,2d} = A_{2u} \oplus B_{2g} \oplus E_{1u} \oplus E_{2g}$$

The three optical modes (higher frequency) come from the doubly degenerate in-plane E_{2g} mode and the out-of-plane B_{2g} however, only the E_{2g} mode is Raman active. This

high-frequency phonon, E_{2g}, corresponds to the G peak in graphene's Raman spectrum which is located at ≈1580cm^{-1}. The second peak found in graphene's Raman spectrum is known as the 2D peak and is located at ≈2700cm^{-1}. It is the overtone of a defect activated peak, the D peak. The D peak is due to the breathing mode of the graphene ring and comes from the transverse optical phonon mode around the Brillouin zone K-point.[51] As we just mentioned, the D-peak is only defect activated as the Raman fundamental selection rules do not allow zone-boundary phonons. However, the 2D peak in graphene is due to two phonons with opposite momentum near the K-point which satisfies the selection rules and is therefore present in pristine graphene. For monolayer graphene, the intensity ratio between these two main peaks ($\frac{I2D}{IG}$) is ≈2 where they can both be fitted by a single Lorentzian profile.

In graphite, the unit cell contains 4 atoms and we therefore have 3 acoustic branches and 9 optical branches. We can find the 12 normal modes at the Γ-point by combining graphene's normal modes in-phase ($\Gamma_{vib,2d} \otimes A_{1g}$) or out-of-phase ($\Gamma_{vib,2d} \otimes B_{1u}$) resulting in[50]

$$\Gamma_{vib,3d} = 2(A_{2u} \oplus B_{2g} \oplus E_{1u} \oplus E_{2g})$$

Again, the only Raman active modes at the Γ point for graphite are the two E_{2g} optical modes. Among these two, there is a high-frequency mode and a low-frequency mode. The high-frequency mode generates the G-peak, which is also present in single layer graphene. The low-frequency mode is caused by the shearing of layers and generates the C-peak.[52] For this reason, it is not present in monolayer graphene and could be used to distinguish monolayer from bilayer. Furthermore, this peak is sensitive to interlayer coupling and consequently scales with the number of layers,[52] where it was measured to be ≈31cm^{-1} for bilayer graphene and ≈42cm^{-1} for bulk graphite.[52] This peak could be used to determine the number of layers however, low-frequency peaks are hard to observe as these values are typically below the edge filter cut-off frequency of typical Raman setups.

Like in graphene, the 2D peak exists in graphite's Raman spectrum, yet its shape and relative intensity drastically changes and therefore can also be used to determine the number of layers. In the monolayer case, this peak originates from two phonons with opposite momentum near the K-point and produces one sharp peak. In the case of bilayer graphene, the 2D peak divides into 4 separate components generating a much broader peak. In Bernal stacked bilayer graphene (AB stacking), the electronic bands split into

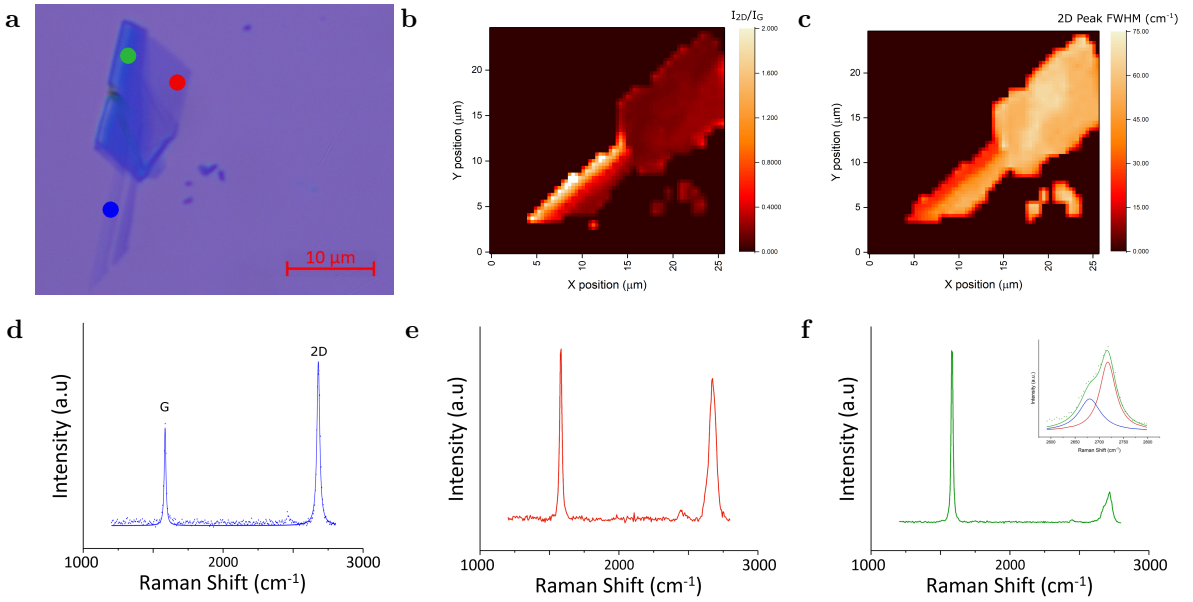

Figure 1.9: **a)** Optical image of a mechanically exfoliated graphene flake. **b)** Raman map of the flake in **(a)**. The map represents the ratio of the intensity of the 2D peak vs. the G peak. A ratio of of more than 1.5 indicates the presence of monolayer graphene. **c)** Raman map of the flake in **(a)** representing the FWHM of the 2D peak. A small FWHM indicates the presence of monolayer graphene ($\approx 20\text{cm}^{-1}$) **d)** Raman spectrum of monolayer graphene as indicated by the blue dot in **(a)**. The G and 2D peaks are located at $1585.8 \pm 0.2\text{cm}^{-1}$ and $2674.1 \pm 0.2\text{cm}^{-1}$ respectively with a relative intensity $\frac{I2D}{IG}$ of 1.7. The FWHM of the G peak is $14.3 \pm 0.6\text{cm}^{-1}$ and the 2D peak has a FWHM of $23.7 \pm 0.5\text{cm}^{-1}$. **e)** Raman spectrum of bilayer graphene as indicated by the red dot in **(a)**. One can notice that the relative intensity ($\frac{I2D}{IG}$) dropped to ≈ 1 and the FWHM of the 2D peak broadened to $48 \pm 1\text{cm}^{-1}$. **f)** Raman spectrum of bulk graphite as indicated by the green dot in **(a)**. **Inset:** Two Lorentzians are used to fit the 2D peak of bulk graphite.

4 bands where the incident light couples more strongly two pairs of bands. However, the two nearly degenerate phonons couple all four bands resulting in four possible processes with four different phonon momenta. These different phonon momenta give rise to four peaks all around 2700cm^{-1} generating the 2D peak.[37] In the case of bulk graphite, three of the phonon momenta found in bilayer graphene become much weaker compared to the fourth momentum resulting in one sharp peak and a low-frequency shoulder.[37,38,53] Not only does the shape of this 2D peak change, but its relative intensity with the G peak also decreases going from ≈ 2 for monolayer, to ≈ 1 for bilayer and much smaller for bulk. Figure 1.9 demonstrates these changes.

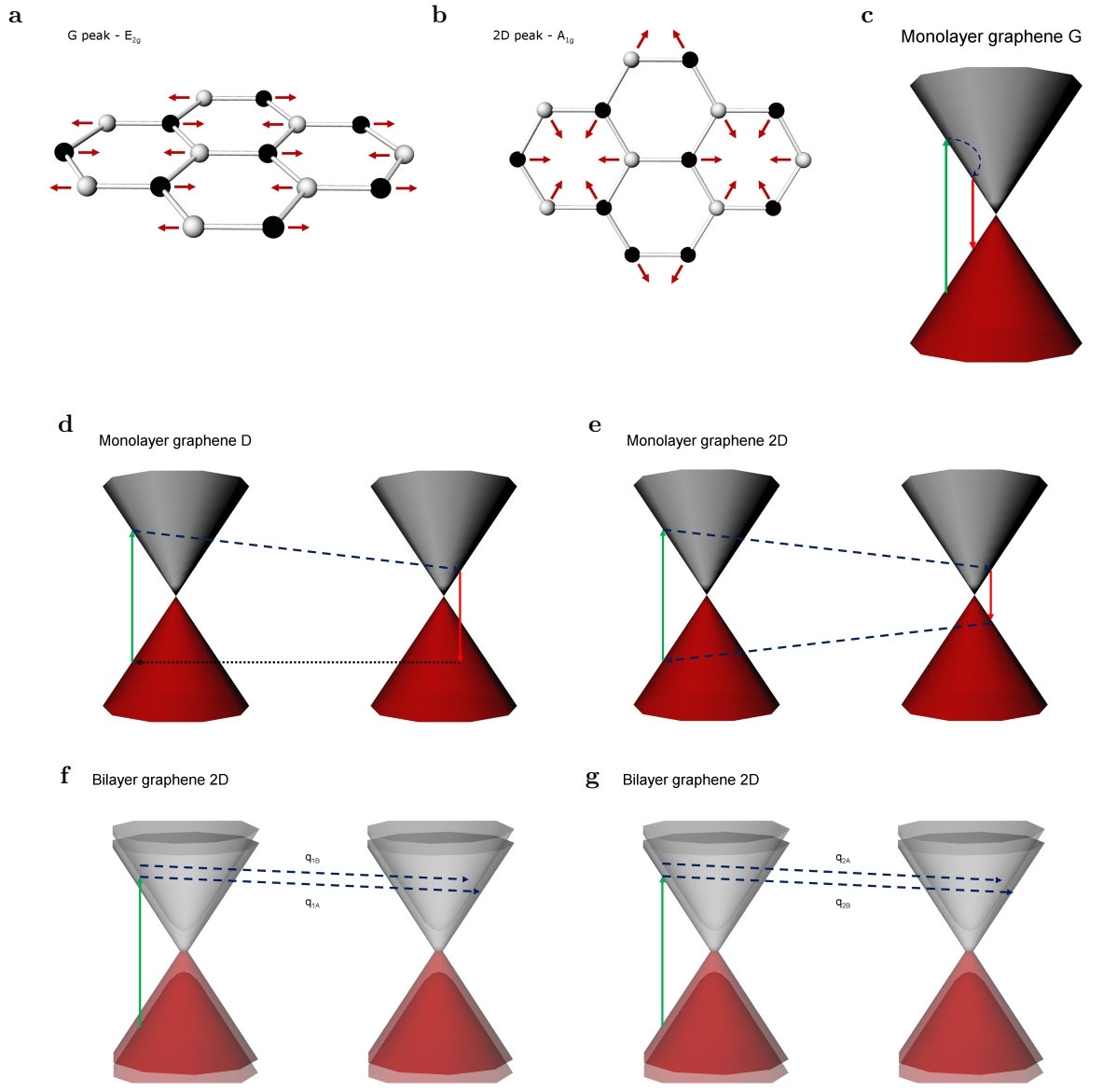

Figure 1.10: **(a-b)** Phonon modes in graphene responsible for the two peaks found in the Raman spectrum. Black and white atoms represent the inequivalent carbon atoms and the red arrows represent the atom displacement. **(c-g)** The cones represent the electron dispersion, green and red arrows represent a photon absorption and a photon emission, respectively, phonon wave vectors are represented by blue dashed arrows, and black dotted arrows represent an electron scattering on a defect. **c)** A one-phonon process responsible for the G peak in monolayer graphene. **d)** The phonon process responsible for the D peak in monolayer graphene demonstrating the need for a defect. **e)** A second phonon with equal but opposite momentum can be scattered to create the 2D peak. **(f-g)** The splitting of the valence and conduction band in bilayer graphene leads to 4 possible phonon processes with slightly different momenta where two are shown per diagram. The second phonons needed to complete the process are not shown in the diagrams.

Chapter 2

van der Waals Heterostructures Fabrication Setup

Specialized instrumentation is needed to create van der Waals heterostructures, consequently, a customized system was developed to enable the production of such stacks.

Optical microscope: The first piece of equipment found in our stacking setup is an optical microscope which is used for locating flakes prior to the transfer and for aligning flakes during the transfer. The microscope that we purchased is the Nikon Eclipse LV150NL, an upright microscope with LED illumination. The microscope is operated as a bright-field microscope illuminated under epi illumination but can be easily adjusted to be used as a differential interference contrast microscope (DIC) or polarization microscope.

Microscope objectives: As the flakes we study tend to be approximately $100\mu m^2$ in area and are exfoliated on a substrate that is approximately $1cm^2$, objectives with various magnifications are needed. For the case when we are searching for transferable flakes, a low-magnification objective is needed to quickly scan across the substrate and locate potential flakes whereas higher-magnification objectives are useful for obtaining a quality estimate on the thickness, cleanliness, and size of the flake. When it comes to stacking two crystals together or aligning a top crystal onto a bottom substrate, we typically employ a low-magnification objective in the early stages of the alignment process and then use higher-magnifications to complete the alignment. Low-magnification objectives are naturally associated with larger depth of fields; therefore, a low-magnification objective can be used to align the top and bottom flakes when they are relatively far apart. As the two flakes get closer together, we may change to a higher-magnification to ensure proper alignment before contact is made. Large working distances are also

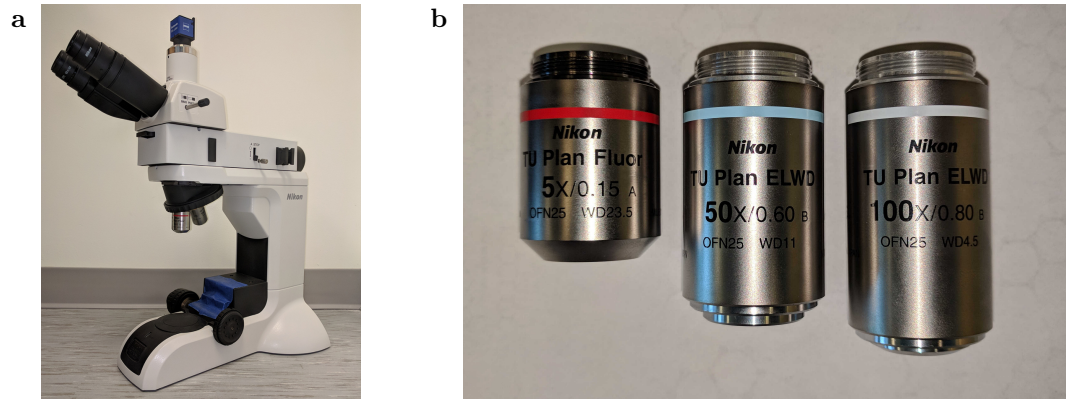

Figure 2.1: **a)** The optical microscope and **(b)** the three lenses used for the transfer setup.

essential for this type of work. The substrate for which the top flake resides does not necessarily have a negligible thickness, consequently, the employed objectives need to have a working distance larger than that thickness.

To satisfy all of these needs, attached to the microscope are three different lenses: 5X, 50X and 100X. The 5X objective is the Nikon TU Plan Fluor EPI, a semi-apochromat lens with a working distance of 23.5mm and a numerical aperture of 0.15. The 50X objective is the Nikon TU Plan EPI ELWD, a semi-apochromat objective with a working distance of 11mm and a numerical aperture of 0.6. Finally, the 100X objective is the Nikon TU Plan EPI ELWD, a semi-apochromat objective with a working distance of 4.5mm and a numerical aperture of 0.8.

Bottom and top manipulators: Precision is key when attempting to perfectly align two surfaces measuring no more than $100\mu m^2$ and therefore, we must limit any source of vibration. Manual microscope stages naturally introduce vibrations when the user utilizes the stages. For this reason, a hands-free approach was taken where we employ computer automated stages. The traditional microscope stage was removed, and we replaced it with a set of manipulators which acted as the bottom microscope stage. A second independent set of manipulators was also added to provide movement for the top stage. All manipulators are programed into the same user-interface where the user can move the manipulators individually or simultaneously, read out the position of each manipulator, save positions, adjust the speed of the manipulators, and automatically focus. There are also built-in safety features that depend on the employed lens, which avoids possible collisions between the sample and lens. Appendix 6.4 provides a complete list of the possible functions as well as the core LabVIEW code used in the development

of the UI.

The bottom stage consists of a set of four independent manipulators which are able to move in all directions which include the X, Y, Z, and θ. To provide a smooth motion, the manipulators are displaced by the means of a stepper motor. The X and Y manipulators can move over a range of 25mm with a step size of 47.625nm. The Z manipulator can travel a total distance of 40mm with a step size of 95.25nm. The rotational stage provides a full 360° rotation at 4.091μrad increments. As for the top stage, three separate manipulators move the sample in the X, Y, and Z direction. These manipulators are run by piezoelectric motors which provide a step size of 11nm in all directions. In the X and Y direction, the manipulators can travel up to 18mm and can travel 30mm in the Z direction.

For both the bottom stage and the top stage to be complete, custom sample holders had to be machined and attached to these stages. As precise control over the temperature of the sample is required during the transfer, the bottom stage is made of a flat heating element. A temperature controller and J-type thermocouple is wired to the heating element to provide the temperature control. To avoid heating the manipulators passed the recommended temperature, the heating element is fixed to a thermal insulating piece of Macor™. To fix the Macor™ block to the manipulators, screw holes were machined at specific locations. A slit was also made to fit the heating element. For the top stage, an angle bracket was machined such that it can be attached to the top manipulators and a glass slide can be fixed inside of it. This transparent glass slide acts as the top sample holder.

Not all 2D materials are inert in air[21,22] and therefore, for them to survive the transfer procedure, the transfer would have to take place in an inert environment such as a glovebox. For this reason, the entire transfer setup was designed such that it is hands-free and could be moved and operated inside a glovebox. The computer-controlled manipulators and temperature controller were chosen to allow this move to a glovebox. Furthermore, a camera was added to the trinocular of the microscope and is connected to the same computer which controls the manipulators. This allows the user to control the manipulators while following the live-feed of the transfer all on the same computer. The camera is the Zeiss Axiocam 105c; a 5-megapixel camera with a 47 frames per second live frame rate and exposure time that can vary from 100μs to 2s.

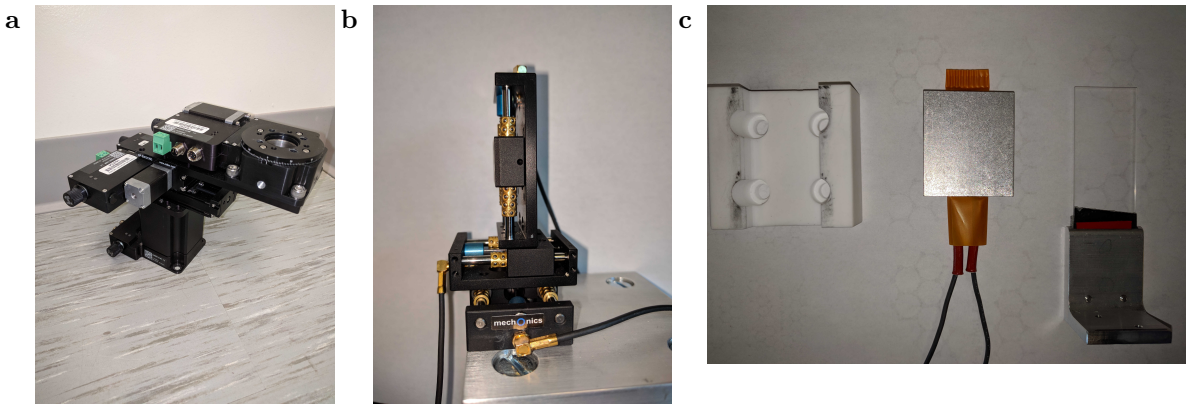

Figure 2.2: **a)** Set of bottom manipulators and **b)** top manipulators. **c)** (Left) Machined piece of Macor made to thermally isolate the heating element from the bottom manipulators. (Center) Heating element that sits in the machined Macor and is used as the bottom sample holder. (Right) Machined angle bracket that can be screwed into place into the top manipulator and can hold a glass slide which is used as the top sample holder

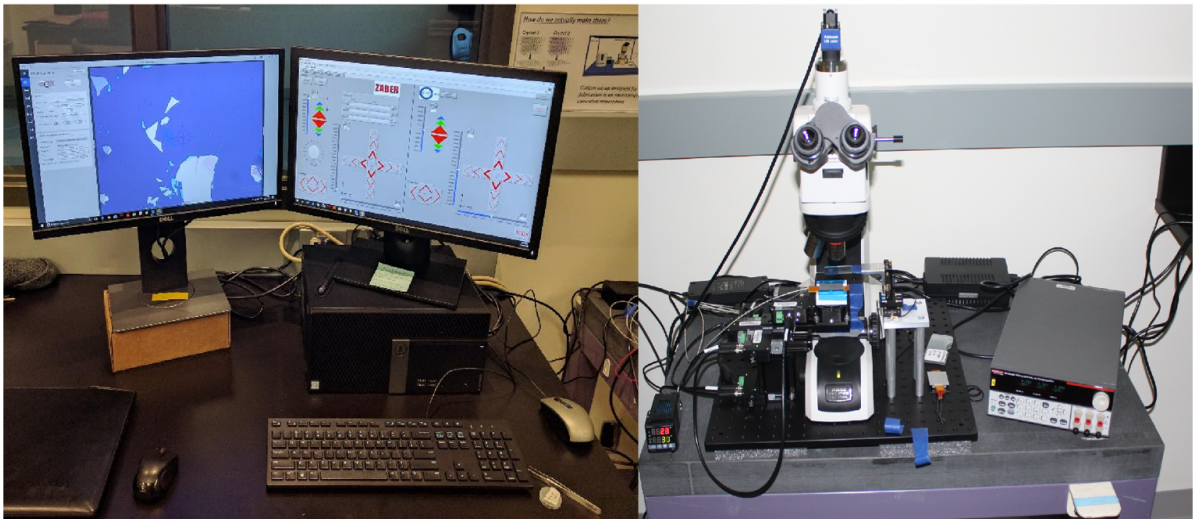

Figure 2.3: Image of the computer and monitors used for the transfer setup. The left monitor provides the live feed as seen from the camera placed in the trinocular of the microscope. The right monitor displays the program used to control the two sets of manipulators.

Components	Description
Optical microscope	Nikon upright microscope LV150N LED Reflected Illuminator
Objectives	5X Objective Lens, N.A. 0.15, W.D. 23.5mm 50X Objective Lens, N.A. 0.4, W.D. 19mm 100X Objective Lens, N.A. 0.8, W.D. 4.5mm
Top manipulator	Z manipulator – 30mm travel with step size of 11nm X manipulator – 18mm travel with step size of 11nm Y manipulator – 18 mm travel with step size of 11nm
Bottom manipulator	Heated Stage Z manipulator – 40mm travel with step size of 95.25nm X manipulator – 25mm travel with step size of 47.625nm Y manipulator – 25mm travel with step size of 47.625nm θ manipulator – 360° travel with step size of 4.091μrad
Temperature controller	Controls the temperature of the bottom stage via a J type thermocouple
Camera	Zeiss Axiocam 105c – 5 megapixels, 47fps live frame rate, exposure time of 100μs-2s

Table 2.1: Full list of the transfer setup components.

For a detailed list of the components involved in this stacking setup, see table 2.1.

Chapter 3

Characterization and Optimization of the Quality and Cleanliness of Heterostructures and Devices

3.1 The Importance of a Clean Interface

With these presented stacking techniques, we have the means to create new artificial van der Waals materials by stacking two crystals together. However, during the transfer procedure, a variety of contaminants such as hydrocarbons[54,55] may get trapped between the different layers. These trapped contaminants may question the legitimacy of the van der Waals bonding between two adjacent layers and hence the nature of the artificial van der Waals material.[54] Moreover, contaminations between layers are known to limit device performance[20,56,57] and worsen transport properties.[58] These contaminations can also induce non-uniform strain and doping which leads to inhomogeneous properties throughout the material.[59,60]

In this chapter, we characterize the stacks that were made using the transfer techniques discussed in the previous chapter using optical microscopy, atomic force microscopy and Raman spectroscopy. This characterization allows us to evaluate the level of cleanliness of the stack interface and stack surface, and to compare the level of cleanliness of the two stacking methods.

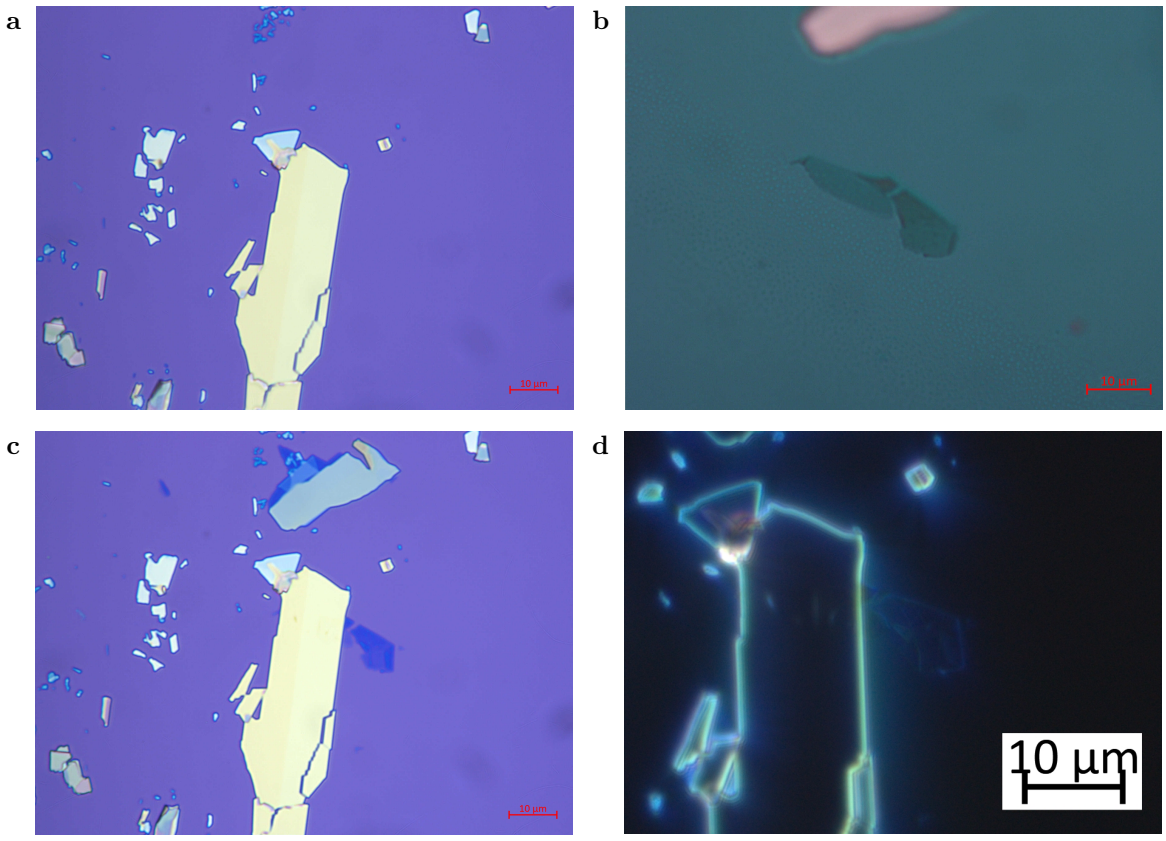

Figure 3.1: Brightfield optical images of **(a)** the ReS_2 flake on a Si/SiO_2 substrate, **(b)** the graphene flake on the PMMA film, and **(c)** the final transfer. **d)** The darkfield optical image of the transfer.

3.2 PMMA-PVA Technique

We have seen that stacking crystals with the PMMA-PVA technique is more difficult to execute in comparison to the stamping techniques. Furthermore, we will show that this stacking technique usually leads to samples that have more bubbles and folds at its interface.

Figure 3.1 is an example of a successful transfer using the PMMA-PVA technique. It consists of monolayer graphene transferred onto thick rhenium disulfide. In the bright-field optical image (figure 3.1c), it is impossible to determine whether the transfer was successful in being wrinkle free yet alone see the outline of the transferred flake. The darkfield image (figure 3.1d) really highlights the edges of the graphene flake and the resulting wrinkles caused by the stacking. To quantify the cleanliness of the sample, we employ the AFM to evaluate the surface roughness.

AFM images were taken once when the stack was placed in an acetone bath for 5 minutes (figures 3.2a-3.2b) and again after the sample has been in the bath for an additional hour at 55°C (figure 3.2c-3.2d). In figures 3.2a-3.2b, we notice an inhomogeneous pattern across both the graphene and rhenium flakes. This is caused by the residual PMMA which remained after the first cleaning. However, this pattern disappears in figures 3.2c-3.2d where we are left with mostly uniform surfaces. By comparing these two images, we can see how a simple warm acetone bath is able to clean off all the PMMA from the stack.

Although the PMMA is easily washed away, the transferred flake is full of wrinkles. The wrinkles generated from this method should not come as a big surprise when you think about the transfer method itself. The thin flake that is meant to be transferred is fixed to a thin layer of PMMA that is freely suspended. It would be like comparing this transfer method to an attempt of applying Saran™ wrap to a flat surface; wrinkles and trapped air bubbles are inevitable. Nonetheless, between the wrinkles, clean areas of approximately $1 - 10\mu\text{m}^2$ can be found and their roughness can be measured. In figure 3.2f, we compare a histogram of the roughness of one of these clean areas to the roughness of the ReS_2. The graphene results in roughness values of $R_a = 0.23\text{nm}$ and $R_q = 0.29\text{nm}$ whereas the rhenium disulfide gives $R_a = 0.21\text{nm}$ and $R_q = 0.28\text{nm}$. As these numbers are very similar, we can conclude that the graphene conforms to the rhenium disulfide in the clean areas of the stack.

3.3 Stamping Technique

Although the PMMA-PVA method results in an apparent clean top surface, the interface between the stacked crystals tend to be wrinkly and full of bubbles. The stamping technique proposes to use a PDMS stamp to push out the bubbles and wrinkles[61] just like a squeegee would when applying a screen protector to a phone. Instead of being freely suspended, the polymer (PPC in this case) is adhered to a PDMS stamp and therefore has less of a chance to fold over itself during the transfer process.

Figure 3.3 is an example of a completed transfer using the stamping technique. In this sample, we transferred monolayer graphene onto thick hBN. As we can see from figures 3.3a - 3.3b, the manual peeling of the PPC off of the Si/SiO_2 substrate and placement on the stamp caused it to wrinkle and thus resulted in an area of folded graphene. However,

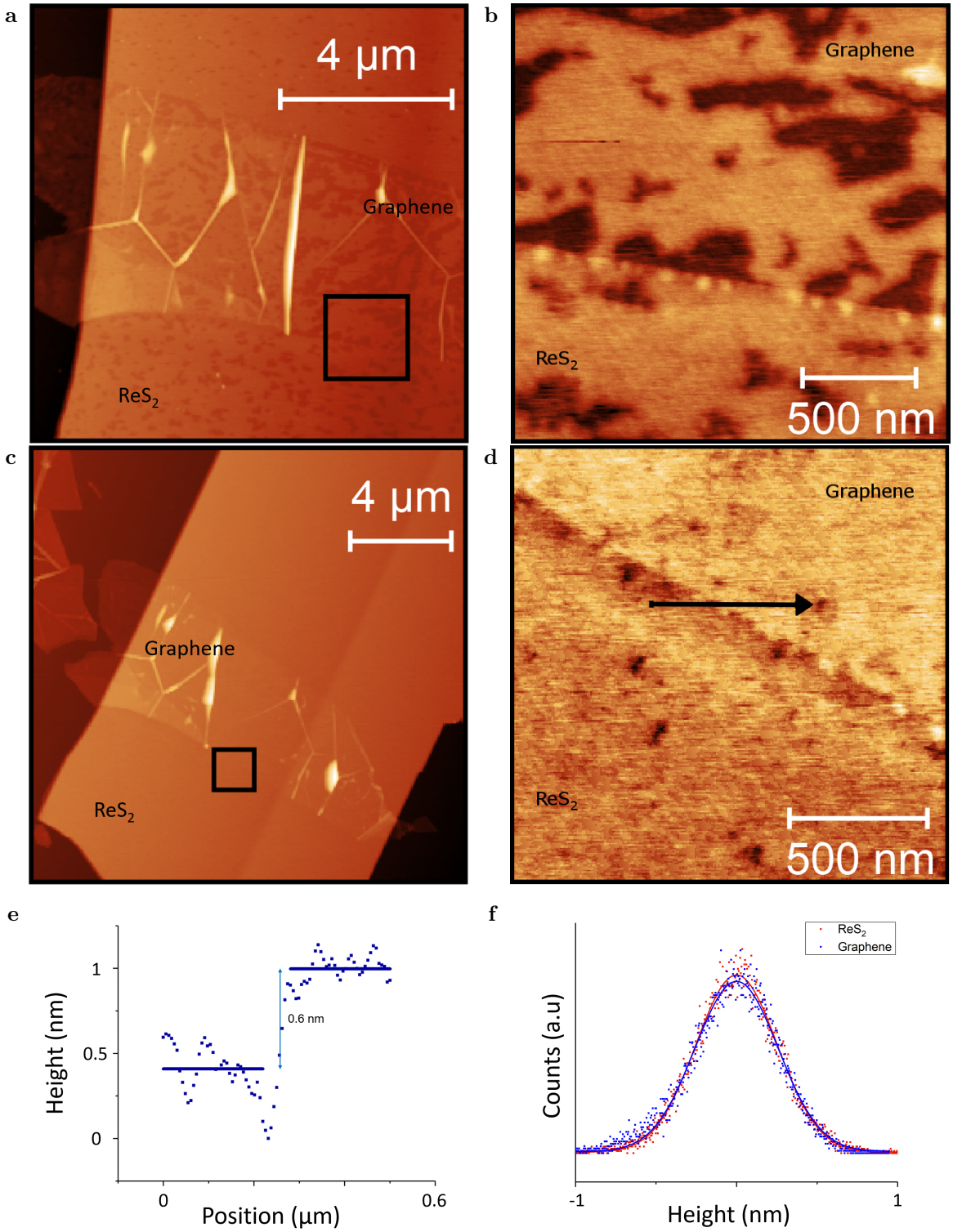

Figure 3.2: **a)** An AFM image of the transfer from figure 3.1 before proepr cleaning. **b)** A high resolution image of the boxed area in **(a)** displaying the step-edge and the residual PMMA. **c)** AFM image of the same stack but after a proper cleaning. **d)** A high resolution image of the boxed area in **(c)**. **e)** AFM line profile across the black line described in **(d)** indicating a step height of 0.6nm which corresponds to the height of monolayer graphene. **f)** Histogram of the height distribution taken from **(d)** fitted by a Gaussian distribution.

a large surface of the flake remained flat on the stamp. In the optical image of the final transfer, we can see a region that appears to have been folded and a region that appears to be bubble and wrinkle free.

Figures 3.3d - 3.3e are AFM images taken of the sample directly after the transfer, i.e., without any cleaning step. As one can immediately see, the entire graphene flake appears to be smooth, absent of wrinkles, and without any bubbles. The height measurement done at the step-edge (0.64nm) suggests that no thin film of PPC was left behind during the transfer, although there is still some polymer residue (bright circles in figures 3.3d - 3.3e). In this case, we find again that the roughness of the graphene is similar to that of the hBN. Graphene's roughness values are given as $R_a = 0.18$nm and $R_q = 0.23$nm. Similarly, the roughness values for hBN are $R_a = 0.25$nm and $R_q = 0.28$nm.

3.4 Additional Cleaning Procedures

The stamping technique produces heterostructures with reduced bubbles and wrinkles compared to the PMMA-PVA technique. However, this transfer technique often tends to leave behind a film of PPC on the sample. Even when there is little residual PPC as demonstrated in the previous stack, a simple wash in acetone is never enough for removing all the polymer. Figure 3.4 demonstrates such a case where graphene was transferred on hBN. AFM images were taken at two instances: after a first cleaning in warm acetone for 1 hour, and after a second cleaning in warm acetone for an additional hour. In the first instance, it is clear that there is an important amount of residual polymer left behind on the stack. After the second cleaning, the surface appears to be more uniform which may mean that the polymer has been successfully cleaned. With a higher resolution image near the step-edge of the graphene, we can extract a step-height of 2.5nm which corresponds to approximately 5 layers of graphene. However, when we perform Raman spectroscopy on this same stack, we are left to conclude that the flake is in fact monolayer graphene as we obtain a sharp 2D peak and a ratio $(\frac{I2D}{IG})$ bigger than 1.5 across the transferred flake, traits belonging to single layer graphene. This indicates that the graphene surface is still tarnished with a layer of polymer which represents the additional ≈ 1.9nm measured during AFM. Therefore, additional cleaning steps need to be investigated.

Thermal annealing: A common approach for cleaning away polymers is to introduce

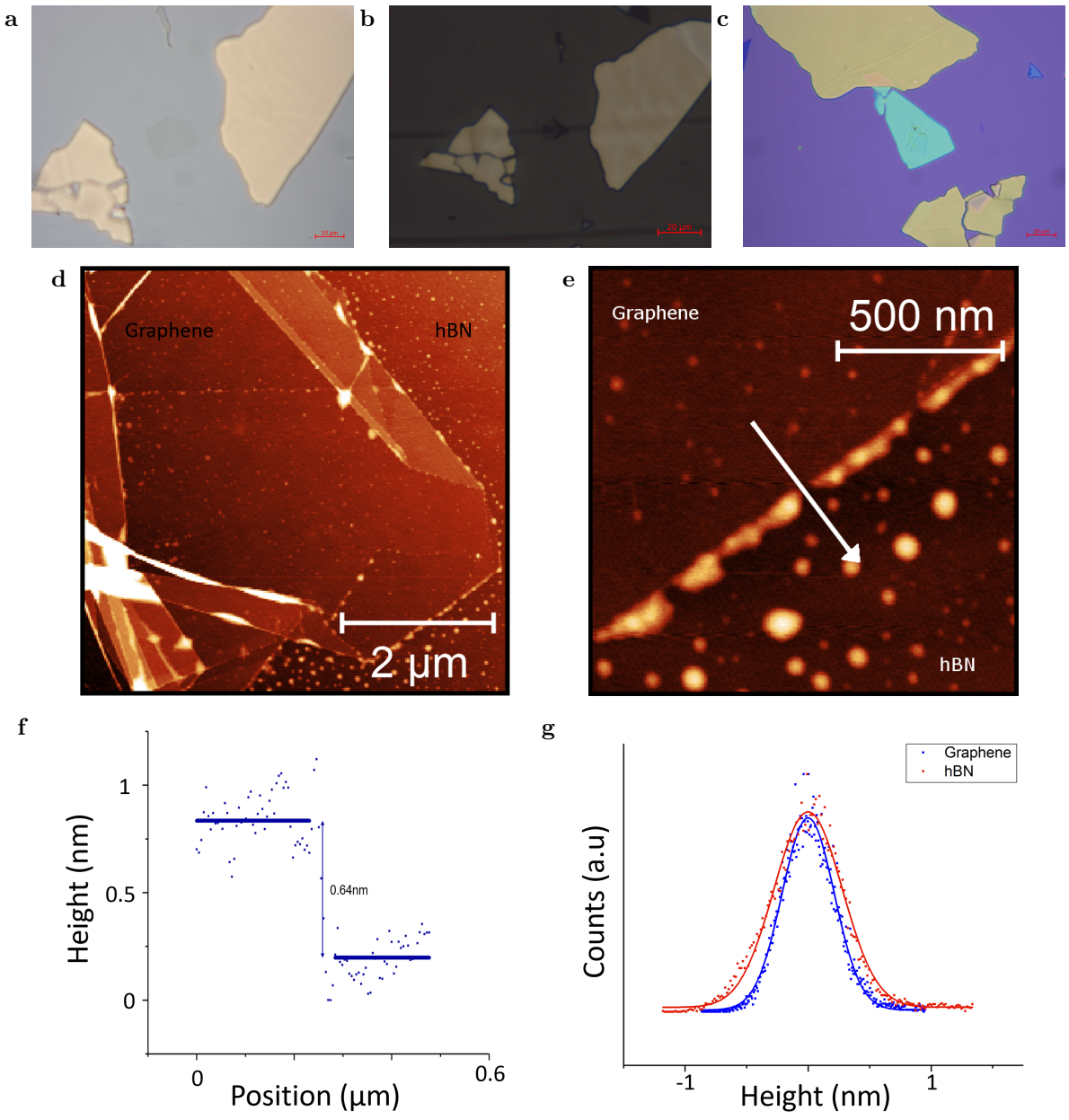

Figure 3.3: Brightfield optical images of **(a)** the graphene flake on a PPC covered Si/SiO_2 substrate, **(b)** the graphene flake and PPC film on the PDMS stamp, and **(c)** the final transfer. **d)** An AFM image of the graphene/hBN stack. **e)** A high resolution image of the lower right corner of the stack displaying the step-edge. **f)** AFM line profile across the white line described in **(e)** indicating a step height of 0.64nm which corresponds to the height of monolayer graphene. **g)** Histogram of the height distribution taken from **(e)** fitted by a Gaussian distribution.

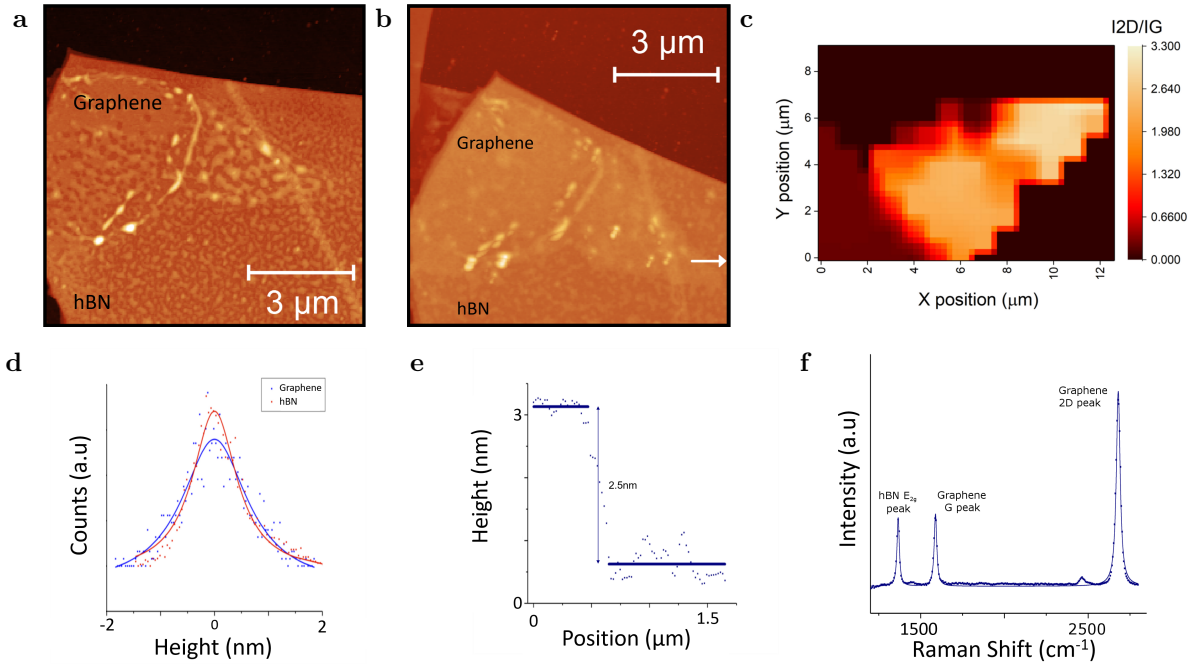

Figure 3.4: **a)** An AFM image of a transfer of graphene on hBN after cleaning in warm acetone for 1 hour. **b)** An AFM image of the same transfer after cleaning in warm acetone for an additional hour. **c)** Raman map representing the ratio of the 2D and G peak of graphene. An orange-white color indicates a ratio bigger than ≈1.5 which is consistent with monolayer graphene. **d)** Histogram of the height distribution taken from **(b)** fitted by a Gaussian distribution. We find that the graphene has roughness values of $R_a = 479$pm and $R_q = 603$pm and that the hBN has values $R_a = 449$pm and $R_q = 584$pm. **e)** AFM line profile across the white line described in **(b)** indicating a step height of 2.5nm. **f)** Raman spectrum taken at the top right tip of the graphene flake in **(c)** which agrees with the spectrum associated to monolayer graphene. The first peak corresponds to the E_{2g} vibration mode of hBN and is located at $1365.6 \pm 0.4\text{cm}^{-1}$. Graphene's G and 2D peaks in this spectrum are located at $1588.6 \pm 0.4\text{cm}^{-1}$ and $2679.8 \pm 0.2\text{cm}^{-1}$ respectively.

an annealing step in the cleaning procedure. Typically, this step is done under vacuum or under some inert gas atmosphere to avoid oxidation or contamination of the sample, however, to simply demonstrate the importance of this step, our annealing was done on a hot plate in air. The samples were placed on a hot plate, set to 300°C and remained there for the duration of an hour. An example of such sample is shown in figure 3.5 where graphene was transferred on ReS_2. In figure 3.5a, it is clear that a film of polymer coats the entire sample as not only is the graphene rugged, so is the ReS_2. The ReS_2 presents roughness parameters of more than 1nm which confirms the presence of PPC. However, once the sample is subject to an annealing process, the PPC disappears and we are left with two pristine surfaces as we can see in figure 3.5b. Again, to demonstrate the cleanliness of our sample, we note the roughness values of both crystals. The graphene has roughness values of $R_a = 168$pm and $R_q = 212$pm and the ReS_2 has values $R_a = 178$pm and $R_q = 223$pm.

This transfer also demonstrated that bubbles may also form at the interface of the crystals just as in the PMMA-PVA technique. From figure 3.5a we notice multiple small bubbles scattered across the interface of the stack. The annealing step causes the bubbles to merge into fewer but bigger bubbles. Therefore, the annealing process also reduces the number of bubbles and increases the percentage of the stack interface that appears to be contaminant-free, hence, creates a cleaner interface.

One must ensure to do the annealing step under vacuum or in an inert environment to avoid oxidation of the sample. As our annealing step was done in air, we can directly see the consequences associated to this by comparing figures 3.5a and 3.5b. We can see that the left tip of the rhenium disulfide crystal is beginning to disappear due to oxidation and burning of the sample.

Raman Spectroscopy: To that end, Raman spectroscopy may offer an alternative where this annealing step can be achieved in air while simultaneously characterizing the stack. The laser in the Raman setup can be used to locally heat areas of the stack that need to be cleaned. This local and controllable heating can prove to be useful in the cases where only specific areas of the sample are heated while the others that are more fragile remain untouched.

In figure 3.6, we performed AFM on a sample of graphene transferred on ReS_2 before and after Raman spectroscopy. As we can see, the density of bubbles is greatly reduced

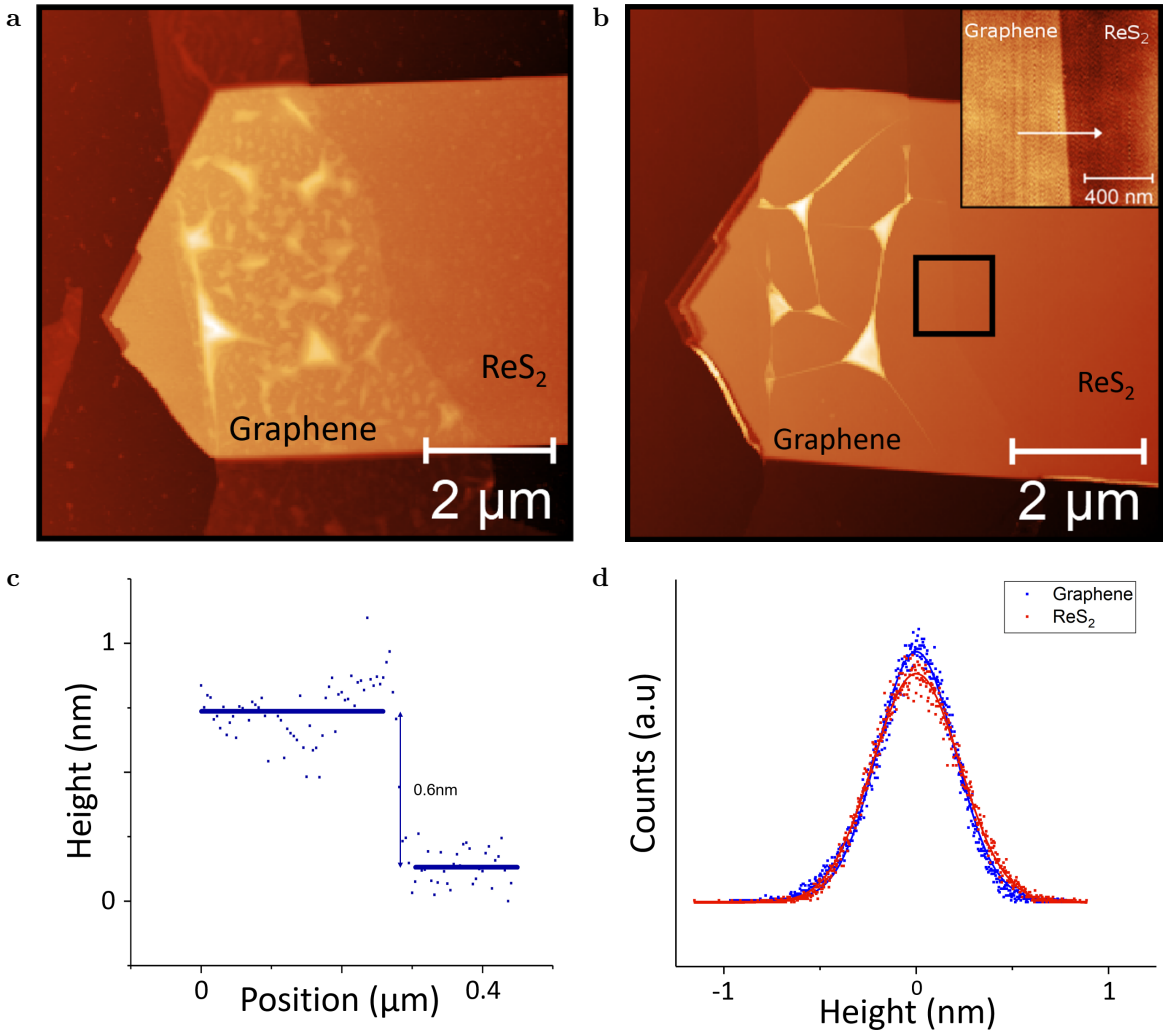

Figure 3.5: **a)** An AFM image of a transfer of graphene on ReS_2 after cleaning in warm acetone for 1 hour. **b)** An AFM image of the same stack after having placed it on a hot plate at 300°C for 1 hour. **Inset**: A high resolution image corresponding to the boxed area. **c)** AFM line profile across the white line described in the inset from **(b)** indicating a step height of 0.6nm which corresponds monolayer graphene. **d)** Histogram of the height distribution taken from the inset in **(b)** fitted by a Gaussian distribution.

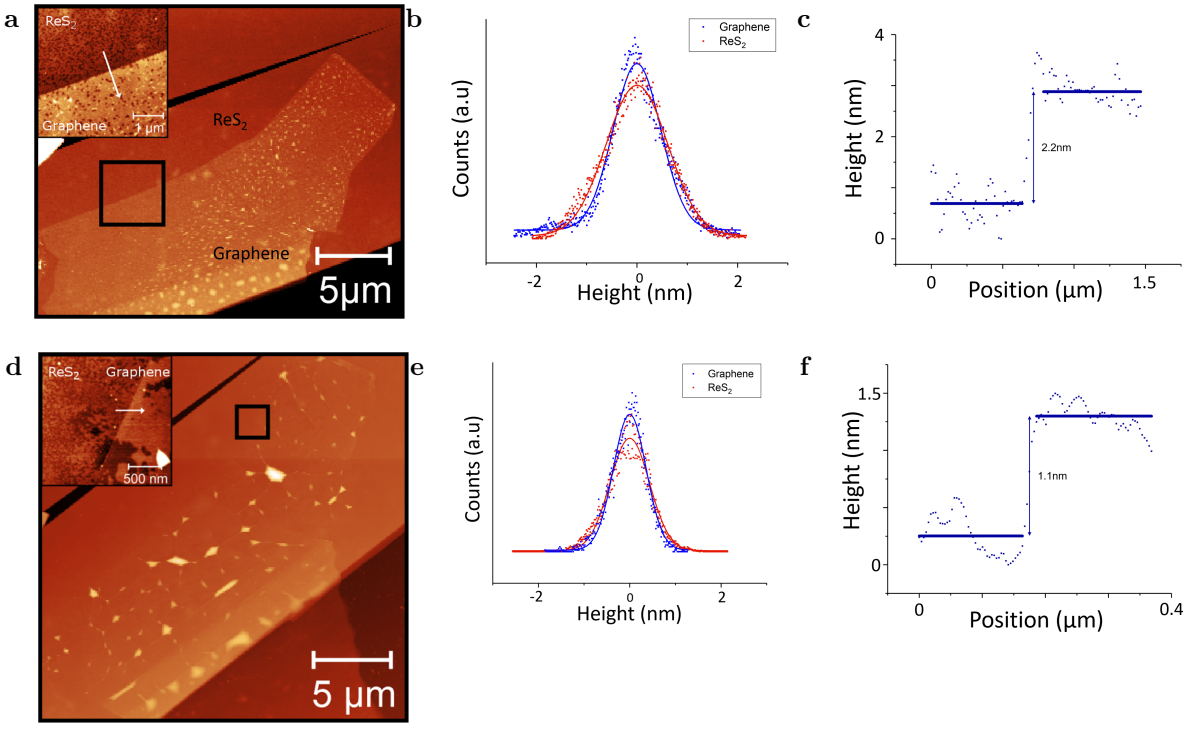

Figure 3.6: **a)** An AFM image of a transfer of graphene on ReS_2 after cleaning in warm acetone for 1 hour. **Inset**: A high resolution image corresponding to the boxed area. **b)** Histogram of the height distribution taken from the inset in **(a)** fitted by a Gaussian distribution. We find that the graphene has roughness values of $R_a = 309$pm and $R_q = 434$pm and that the rhenium disulfide has values $R_a = 515$pm and $R_q = 634$pm. **c)** AFM line profile across the white line described in the inset from **(a)** indicating a step height of 2.2nm. **d)** An AFM image of the same stack after having performed Raman spectroscopy with a laser power of 8.7mW. **Inset**: A high resolution image corresponding to the boxed area. **e)** Histogram of the height distribution taken from the inset in **(d)** fitted by a Gaussian distribution. We find that the graphene has roughness values of $R_a = 301$pm and $R_q = 352$pm and that the rhenium disulfide has values $R_a = 365$pm and $R_q = 413$pm. **f)** AFM line profile across the white line described in the inset from **(d)** indicating a step height of 1.1nm.

which then also reduces the roughness parameters of the stack. The decrease in bubbles also results in a true height measurement of the thickness of our graphene flake where we now read the height of bilayer graphene ($\approx$ 1nm). The laser may be able to clean the interface of our stack by decreasing the bubble density, however, the inset from figure 3.6d clearly shows that the surface topography is quite inhomogeneous and residual PPC still remains on the surface. Higher laser powers and dwell times remain to be further studied where they may be able to completely remove the polymer.

In addition to cleaning the sample, we have seen that Raman spectroscopy is used as a characterization tool. So far it has been used to determine the height of a sample and deduce, in parallel with the AFM, whether the surface is clean. Furthermore, it can also give information about the interface cleanliness. Particularly, strain in graphene can easily be identified in Raman spectroscopy where there is a distinctive red shift in both

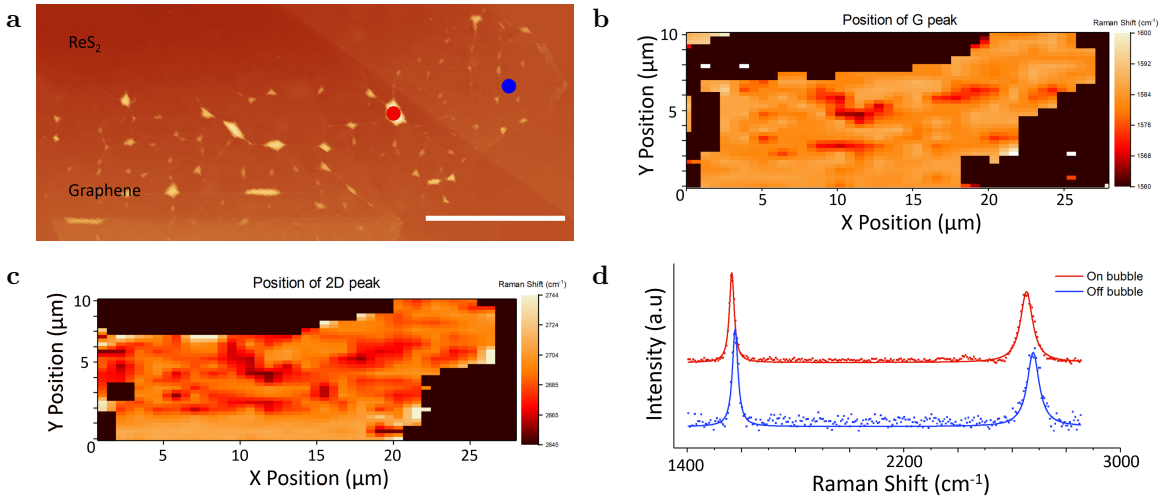

Figure 3.7: **a)** An AFM image of the same transfer of graphene on ReS_2 from 3.6 (Scale bar of 5μm). **b)** Raman map of the G peak position. **c)** Raman map of the 2D peak position. **d)** Raman spectra measured on the bubble (red) and off the bubble (blue) as indicated in 3.7a. We find that the G and 2D peak red-shift by values of 13cm^{-1} and 25cm^{-1} respectively.

the G and 2D peak.[40,41] As one would imagine, bubbles created at the interface of the stack during the transfer would inevitably induce some strain on the top layer. When performing Raman spectroscopy on these samples, this strain is immediately noticeable by simply mapping the position of the graphene peaks (G and 2D) as can be seen in figure 3.7. When comparing these Raman maps to the AFM images, we can directly correlate the red shifted peaks to areas of high strain, i.e., bubbles. In these maps, we notice a red shift of the G peak as large as 20cm^{-1} and a red shift of the 2D peak as big as 40cm^{-1} which corresponds to a peak shift ratio of 2, a value that is in agreement with previous measurements found for biaxial strain in bilayer graphene.[62]

Examples of devices: Now that we are able to achieve a certain level of cleanliness, we can take the next step and begin building devices from heterostructures. A particular device that we have been working on is creating quantum dots in MoS_2 based van der Waals heterostructures.[63–67] 2D materials are a promising candidate in the world of quantum electronics, where precise confinement and manipulation of multiple charges and spins is required.[68,69] van der Waals heterostructures can be manipulated and made into devices in such a way that they demonstrate efficient control of quantum dot systems.[63–67]

The steps to making our device is to first pattern fine local bottom gates on a Si/SiO_2 using electron-beam lithography. These bottom gates serve as the quantum confine-

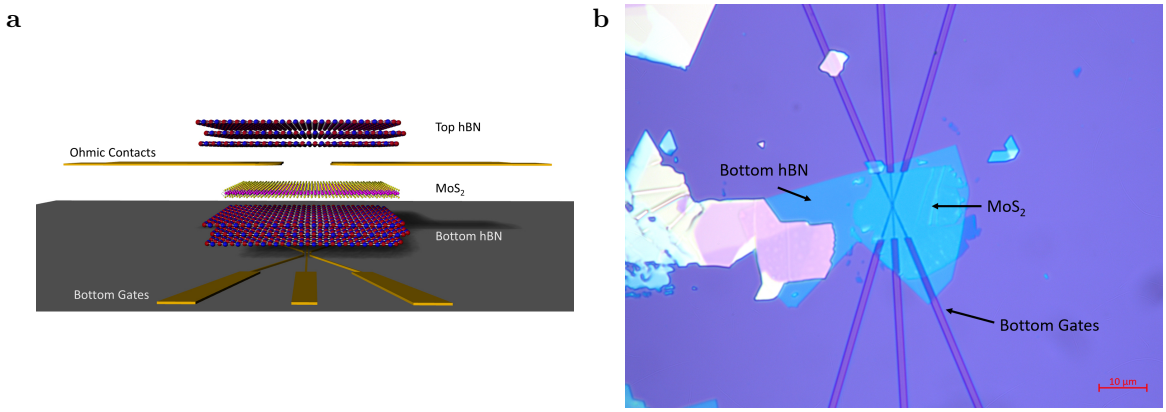

Figure 3.8: **a)** Schematic of the MoS_2 based van der Waals heterostructure. Both sets of contacts are Ti/Au and are electron-beam evaporated onto the sample. **b)** Optical image of the completed first transfers before the patterning of the ohmic contacts.

ment potential.[63,65] Next, an hBN flake measuring approximately 30nm in thickness is transferred onto the bottom gates followed by a few-layer MoS_2 flake. Electron-beam lithography is once again employed to create ohmic contacts to the MoS_2. A last hBN flake is transferred on top of the device using the stamping technique which serves to encapsulate the device (figure 3.8).

Chapter 4

Optical Properties of Semiconducting Heterostructures with Relative Twist Angles

Just like in the case of graphene, Raman spectroscopy can give information about the number of layers in a MoS_2 crystal. First, let us consider the case of bulk MoS_2. In its unit cell, MoS_2 has 6 atoms and therefore has 3 acoustic branches and 15 optical branches resulting in a total of 18 normal modes. At the Γ-point, these normal modes are the following:[70]

$$\Gamma = A_{1g} \oplus 2A_{2u} \oplus B_{1u} \oplus 2B_{2g} \oplus E_{1g} \oplus 2E_{1u} \oplus E_{2u} \oplus 2E_{2g}$$

Out of the 15 optical modes, only 4 of them are Raman active: the E_{1g} mode, the two E_{2g} modes, and the A_{1g}. In a typical back-scattering Raman setup, the E_{1g} mode is forbidden and we do not detect it.[71] One of the E_{2g} modes, the E^2_{2g} mode, is difficult to detect as it corresponds to the low frequency mode which is located at $\approx 25\text{cm}^{-1}$ and arises due to lateral vibrations of adjacent layers (shear-mode). The second E_{2g} mode, E^1_{2g}, originates from the molybdenum atom moving laterally in one direction whereas the two sulfur atoms move laterally in the opposite direction and generates a detectable peak around 380cm^{-1}. The A_{1g} mode results in a second detectable peak around 409cm^{-1} and appears due to the sulfur atoms vibrating out-of-plane. Refer to figure 4.1 for a visual description of these modes.

If we consider single layer MoS_2, we would expect to lose the low-frequency mode because there would be no more interlayer processes. The E^1_{2g} and the A_{1g} do remain, however,

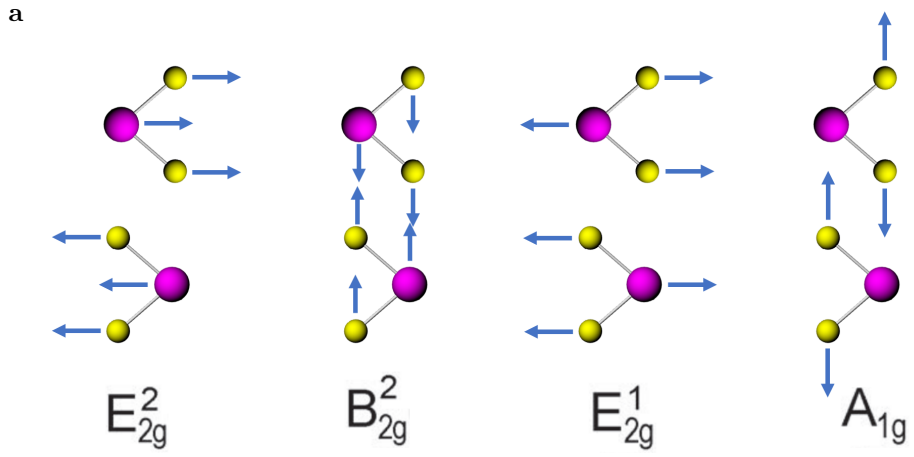

Figure 4.1: Visual representation of the MoS_2 vibration modes responsible for its Raman spectrum. The B^2_{2g} vibration mode is only Raman active for even number of layers in few layer MoS_2.[72–74]

they suffer a shift in frequency that is found to be layer dependent.[39,71] In 1980,[75] a study showed that these two phonon modes blue-shift as a function of applied hydrostatic pressure. Compared to this study, the A_{1g} phonon mode is also found to blue-shift when the number of layers is increased.[39,71] This should not come as a surprise as the A_{1g} phonon mode corresponds to an out-of-plane breathing mode and the addition of layers would result in a larger out-of-plane force constant which suppresses atom vibration just as an increase in pressure would. However, the E^1_{2g} mode experiences a red-shift in frequency when going from monolayer to bulk MoS_2;[39,71] a characteristic opposing the result obtained with hydrostatic pressure. This trait was attributed to long-range Coulomb interactions between the MoS_2 layers.[76]

4.1 Raman Spectroscopy of Twisted MoS_2 Flakes

Introducing a relative twist angle between adjacent layers of a two-dimensional crystal can affect the interlayer coupling between those layers. When we speak of interlayer coupling, we are talking about the degree at which two adjacent layers in a material are coupled to each other. For example, when considering a tight binding model, the interlayer coupling is related to the interlayer hopping parameters. Bilayer graphene provides an example of such an effect where twisting the adjacent layers of graphene can modify the interlayer coupling. Furthermore, a large twist angle (above 20°) effectively decouples the two layers of graphene. These two decoupled graphene layers go on to exhibit properties that are indistinguishable from those of single-layer graphene.[77]

Monolayer MoS_2 has a direct band gap[17] which leads to the ability to absorb up to 10% of incident sunlight.[78] As monolayer MoS_2 corresponds to a thickness less than 1nm, an absorption of 10% corresponds to an order of magnitude higher than GaAs and Si, the most commonly used solar absorbers.[78] However, as soon as a second layer of MoS_2 is added, the direct band gap transitions to an indirect band gap and the material loses these phenomenal properties. With graphene in mind, the main motivation is to attempt to decouple adjacent layers of MoS_2 by introducing a relative angle between the layers in the hopes to regain a direct band gap in bilayer MoS_2 and therefore a higher absorption.

The interlayer coupling in MoS_2 is sensitive to the number of layers as can be seen by the shifting of the E^1_{2g} and A_{1g} peaks. Raman spectroscopy can also be used to demonstrate that it is sensitive to the stacking orientation of the layers by observing a similar shifting of the E^1_{2g} and A_{1g} peaks as well as a shift in the low-frequency modes.[48,79–83] In the low-frequency regime, there are two peaks known as the shear mode and the layer breathing mode that appear on the Raman spectrum.[48] As previously mentioned, the shear mode corresponds to the E^2_{2g} mode. The layer breathing mode is caused by one of the B_{2g} modes (B^2_{2g})[84] and corresponds to a rigid out-of-plane layer displacement. These produce two peaks at 22.9cm^{-1} and 38.1cm^{-1}[48] for naturally stacked bilayer MoS_2. They have found that at a twist angle near 0° or 60°, both modes suffer a shift of up to 8cm^{-1}. Between 20° and 40°, the shear mode is no longer observed as it is supposed to shift to extremely low-frequencies (10cm^{-1}) where it is no longer detectable. These low-frequency modes are hard to detect and are in fact undetectable in the Raman system we used. We will therefore only consider the E^1_{2g} and A_{1g} peaks to study twisting and its effect on interlayer coupling in bilayer MoS_2.

We have created artificial bilayer MoS_2 using the PMMA-PVA method, which consists of two monolayer MoS_2 flakes (see figure 4.2). During the stacking of the flakes, the top flake was intentionally placed such that half of its surface would be on the bottom flake while the other half would be on the substrate (Si/SiO_2). However, during the transfer, part of the top flake folded on itself which resulted in another artificial bilayer area. Additionally, the bottom flake has a small region where there are two-layers of MoS_2. This sample then offers 2 areas with artificial bilayer and one area with natural bilayer. We will refer to these areas as the folded bilayer, the stacked bilayer, and the natural bilayer.

On this stack, we performed Raman spectroscopy to study the evolution of the Raman

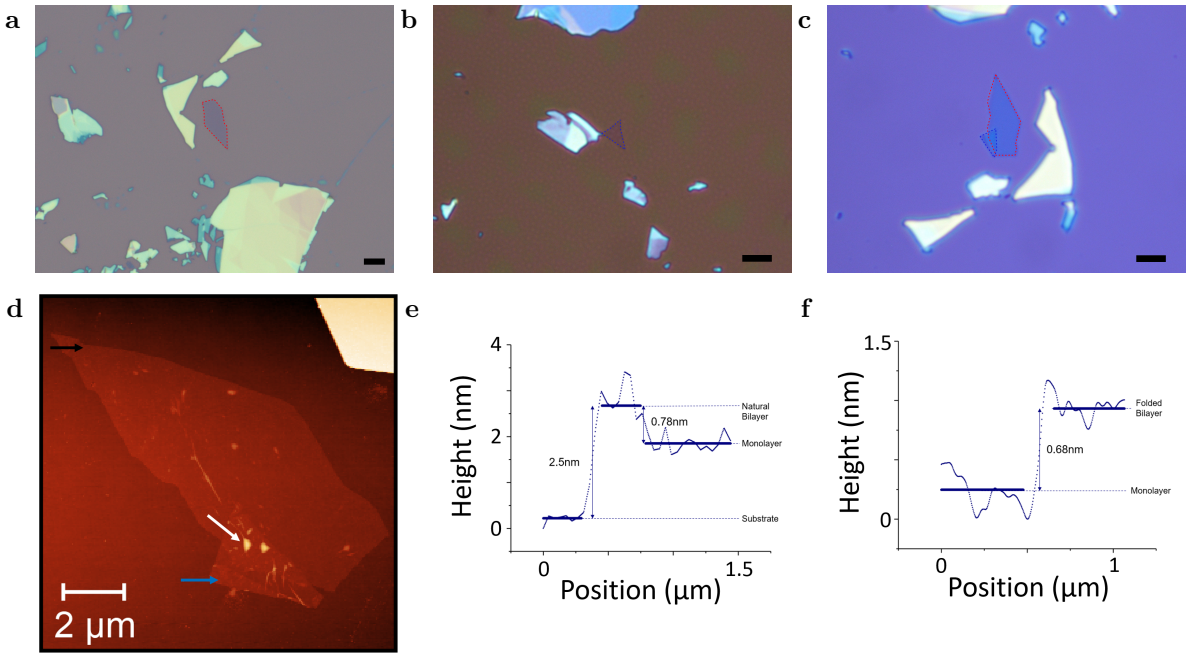

Figure 4.2: **(a-c)** Optical microscope images of the bottom MoS_2 flake **(a)**, the top MoS_2 flake **(b)**, and the twisted MoS_2 stack **(c)**. All scale bars in the optical images measure 5μm. **d)** An AFM image of the twisted MoS_2 stack revealing the three different bilayer areas. The black arrow passes over the natural bilayer, the white arrow points at the stacked bilayer, and the blue arrow points at the folded bilayer. **e)** The line profile associated to the black arrow in **(d)** revealing a thickness of 0.78nm when going from the bottom flake monolayer region to its bilayer region, consistent with a single layer step height. From the substrate to bilayer, 2.5nm is measured which indicates that the bottom flake has a height measurement of 1.7nm, again consistent with the height of monolayer when going from substrate to MoS_2. **f)** The line profile related to the white line in **(d)** indicating a step height of 0.68nm demonstrating the fact that the top flake is also monolayer MoS_2.

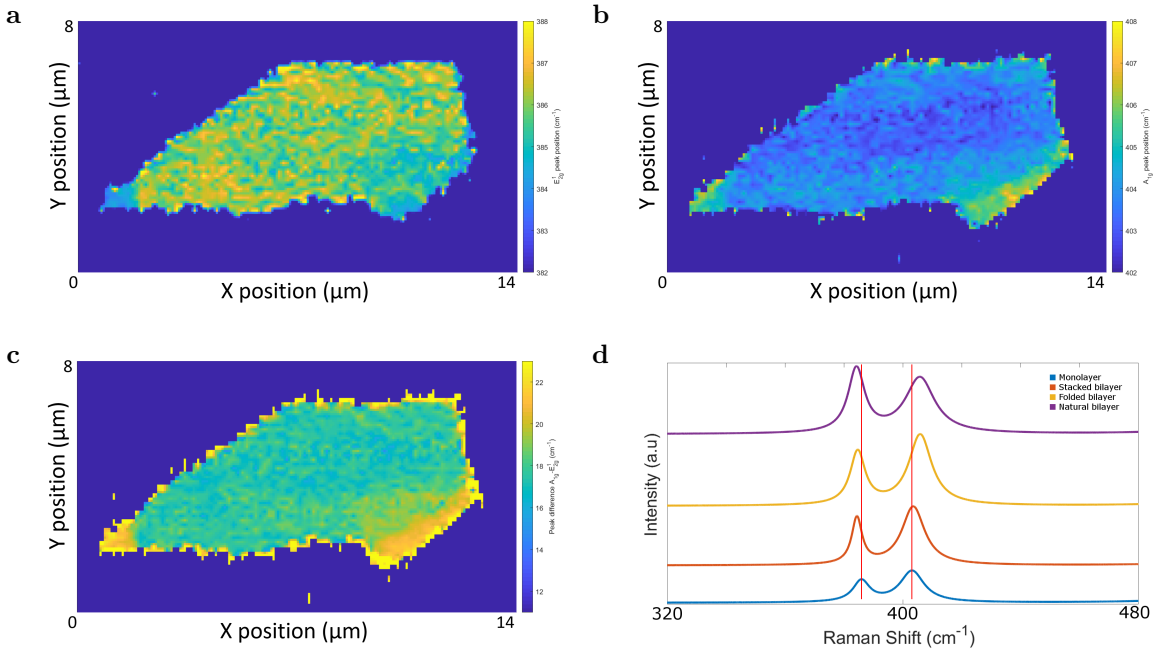

Figure 4.3: **a)** Mapping of the E^1_{2g} and **b)** the A_{1g} Raman peaks. **c)** Map of the frequency difference A_{1g}-E^1_{2g}. **d)** Raman spectra taken on the bottom flake monolayer (blue), the stacked bilayer (orange), the folded bilayer (yellow), and the natural bilayer (purple).

peaks when going from monolayer MoS_2, to natural bilayer MoS_2, and to the two artificial bilayer MoS_2. To visualise this shifting, the position of both the E^1_{2g} and the A_{1g} where plotted as a function of position in figure 4.3. In this figure, we also plotted the frequency difference between these two peaks as it should grow from monolayer to bulk.

When comparing the bilayer areas to the monolayer area, we notice a clear change in peak position for both the E^1_{2g} peak and the A_{1g} peak, which is to be expected. Furthermore, a small but visible change can also be seen when comparing the peaks in the various bilayer areas. This is caused by the different stacking orientation. To further investigate, let us determine the stacking orientation of each area.

The MoS_2 natural bilayer was a result of mechanical exfoliation and therefore should respect a 2H stacking order. For this stacking order, the molybdenum atoms of one layer align over the sulfur atoms of an adjacent layer and similarly, the sulfur atoms align over the molybdenum atoms(see figure 4.4c).

Now let us consider the folded bilayer area. From the AFM image, we can measure the top left corner of the top flake to have an angle of 60°. This indicates that the MoS_2 is either in an *armchair* or *zigzag* configuration at that area (see figure 4.4a). We also

measure a 90° angle at the lower left corner which corresponds to the angle between the armchair and zigzag configuration. This indicates that if the top left corner of the flake is in an armchair (zigzag) configuration, then the fold is along the zigzag (armchair) direction. Assuming the fold is along the armchair direction, then the resulting stacking order of the folded bilayer would be an AA stacking: molybdenum is aligned over molybdenum and sulfur is aligned over sulfur (see figure 4.4b). Otherwise the fold is along the zigzag direction where we have two outcomes: the fold is along the molybdenum atoms or the sulfur atoms. If it falls on the molybdenum atoms, we end up with an AB′ stacking: Mo is over Mo and S is located at the center of the hexagons (see figure 4.4d). If it falls on the sulfur atoms, we have an A′B stacking: S is over S and Mo is located at the center of the hexagons (see figure 4.4e).

In previous studies, finding the twist angle between the top flake and the bottom flake has been straightforward as they use CVD grown MoS_2[48,79,80,82,83] which produces triangular flakes making the orientation of the flakes easy to determine. Determining whether the edges are Mo or S terminated are also straightforward in CVD flakes because a sulfur terminated flake will result in a small kink near the center of the edges of the triangle whereas a molybdenum terminated edge results in a straight line.[85] Furthermore, zigzag edges are the most common morphology in CVD grown MoS_2 triangles therefore they need not worry about whether an edge is in a zigzag or armchair configuration. In our case, we do not use CVD crystals and therefore the determination of the twist angle is a more difficult task. To find the twist angle for our exfoliated flakes, we must consider three parameters: the edge direction, the edge configuration (zigzag or armchair) and whether the edge is sulfur or molybdenum terminated. The only parameter that we can determine with high certainty is the edge direction. From the AFM images, we can find edges all along the flake that are parallel or differ by a factor of 30°. These edges will determine the crystal direction. Because we cannot determine the edge configuration or termination, we will consider all cases. First we note that bilayer MoS_2 has a twist angle periodicity of 120° (think of a triangle). Second, the angular difference between a zigzag orientation and an armchair orientation is ±30°. Finally, the angular difference between a molybdenum or a sulfur terminated edge is 60°. Therefore, the difference between the measured crystal direction of the bottom flake and the top flake is not our only possible twist angle but we will have to consider that angle difference $\pm 30 (mod\ 120)$ and $+60 (mod\ 120)$. For example, if the edges of the bottom flake were perfectly aligned, then we would consider a twist angle of 0°, 30°, 60°, and 90°. In our case, for the bottom

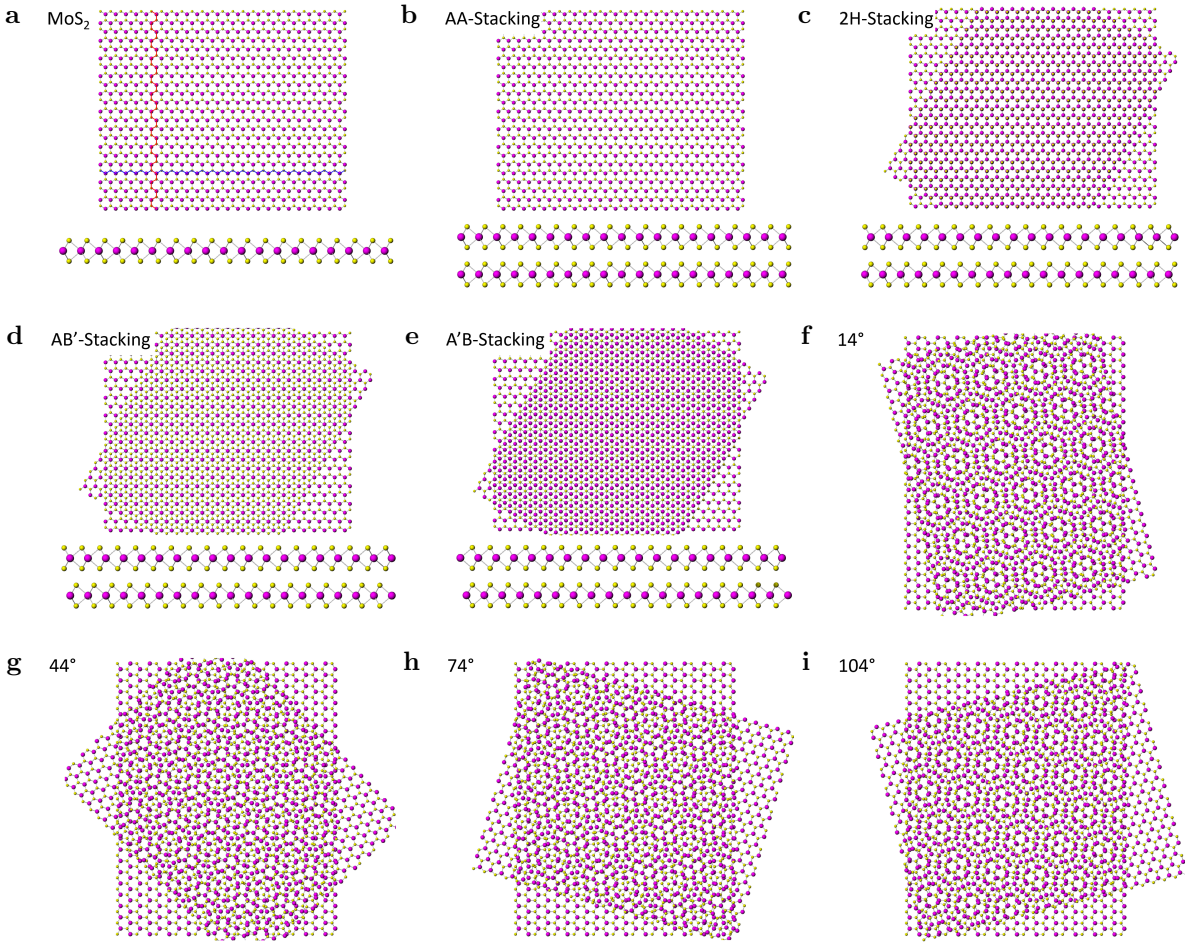

Figure 4.4: Ball and stick representation of monolayer MoS_2 and of the different stacking configurations for twisted bilayer MoS_2. Purple spheres represent molybdenum atoms whereas yellow spheres represent sulfur atoms. **a)** The blue and red lines represent the zigzag and armchair directions respectively. **b)** Bilayer MoS_2 corresponding to one possible configurations related to a twist angle of 0°, the AA-stacking. **(c-e)** The three possible configurations for bilayer MoS_2 corresponding to a twist angle of 60°. **(f-i)** Ball and stick representation of twisted bilayer MoS_2 for the four possible twist angles found in our sample.

flake, we measure a crystal direction of either $-0.4°$, $59.1°$, and $119.3°$. As for the top flake, we measure $-46.6°$, $-15°$, and $73.7°$. These reduce to four possible twist angles: $14° \pm 1°$, $44° \pm 1°$, $74° \pm 1°$ or $104° \pm 1°$.

As mentioned earlier, other groups have used CVD grown crystals to study the effect of twisting MoS_2.[48,79,80,82,83] In some cases, they simply grow the MoS_2 on two separate substrates and transfer them on top of each other without worrying about alignment. This results in a abundance of twisted MoS_2 bilayers with various twist angles. We can then compare our results to theirs (see figure 4.5). To do this, we compared the difference between the two peak positions, A_{1g} - E^1_{2g}. For the natural bilayer, we have established

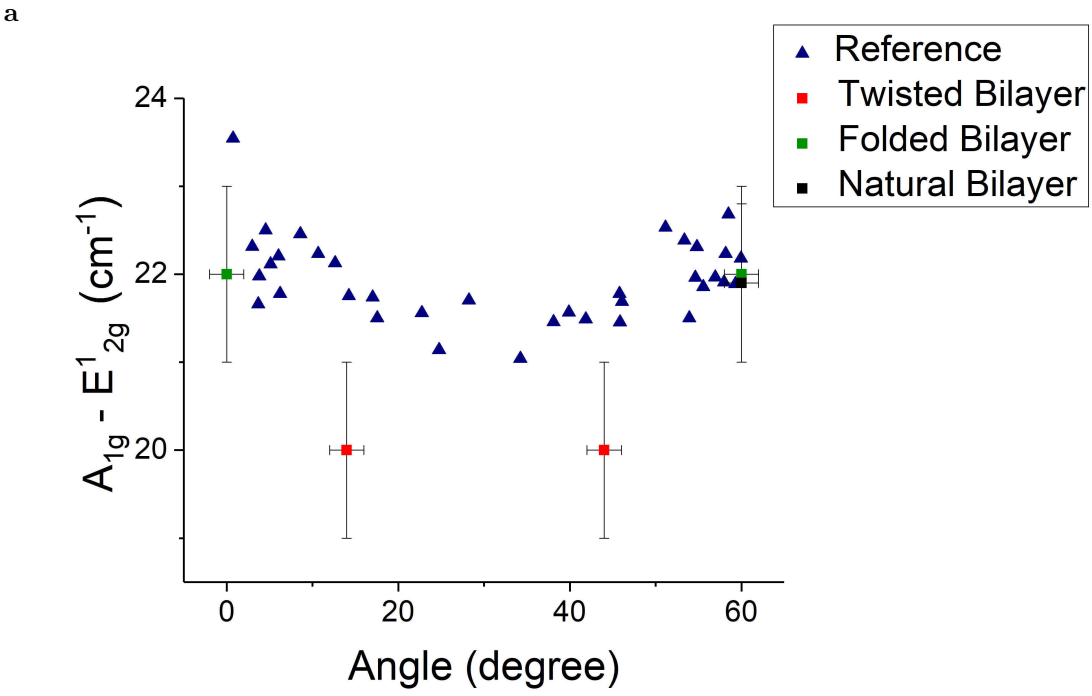

Figure 4.5: **a)** Peak position difference A_{1g} - E^1_{2g} with respect to the twist angle between monolayers of MoS_2. Reference values taken from.[48]

that the twist angle is 60° (2H) and we measure a peak difference of (21.9 ± 0.9)cm^{-1}. The folded bilayer corresponds to a twist angle of either 0° or 60° (AA or AB′/A′B) where we obtain a peak difference of (22 ± 1)cm^{-1}. These two values agree with the lower end of the reference values. A small discrepancy arises when we look at the twisted bilayer area. As the reference values only considered twist angles between 0° and 60°, we will only consider a twist angle of 14° or 44° for this area. The twisted MoS_2 bilayer resulted in a peak difference of (20 ± 1)cm^{-1} which is about 1cm^{-1} less than the smallest value found in the reference. This small difference could be due to the low spectral resolution of the instrument used during these measurements (one data point per 4.5cm^{-1}) which limited the precision of the determination of the exact peak position. The fabrication and characterization of additional samples would help reduce this uncertainty. Although we see a bigger shift compared to the referred data, we observe the same trend; as you approach a twist angle of 30°, the Raman peaks experience a smaller shift. As this shift is related to the interlayer coupling, we may conclude that a relative twist between adjacent layers modifies the interlayer coupling.

Chapter 5

Conclusion and Outlook

Heterostructure cleanliness: Within the framework of this thesis, we explored various methods for stacking 2D materials and creating van der Waals heterostructures. These van der Waals heterostructures offer new ways of studying fundamental physics and show promising properties which are appealing to researchers in many fields.

The level of cleanliness at the interface at each layer in stacks is crucial for device performance, obtaining maximum transport properties and obtaining homogeneity across a sample. The surface cleanliness is also critical for making devices where we want to ensure there is proper contact between the electrical contact and the sample. Furthermore, the surface cleanliness is key for stacking multiple crystals on top of each other; a contaminated surface would lead to a contaminated interface. Consequently, in addition to studying the various assembly methods, we looked to optimize the cleanliness of the stacks.

In this regard, we found that the stamping technique created heterostructures with less interface contaminants compared to the PMMA-PVA technique, however, the polymer associated with this technique could not be cleaned off with simple wet chemistry. Simple annealing on a hot plate successfully cleaned away residual polymer and limited any interface contaminants that may have occurred during the process, yet damage to the sample was nearly inevitable when doing so in air. Using Raman spectroscopy allowed us to characterize the stacks while simultaneously and locally cleaning the surface and interface of the stacks. The heat transferred from the laser was able to reduce the number of bubbles at the heterostructure interface, but residual polymer remained at the surface. Therefore, future work would involve the study of the laser at higher powers and longer dwell times.

For the stamping technique, it has been shown that the PPC polymer is not a necessity and one can simply exfoliate the desired top crystal on a PDMS stamp.[57,59] When using this technique, similar results occur where a difficult to clean PDMS layer is left covering the sample. Vacuum annealing was used to clean the sample, however this resulted in a level of cleanliness inferior to freshly exfoliated crystal. To obtain maximum cleanliness, Jain *et al.* developed a UV-O_3 treatment recipe which modified the PDMS stamp. Following this treatment, they would exfoliate the crystal on the stamp and proceed with the transfer which resulted in a reduction of residues.[59] This technique could possibly be applied to the PPC before exfoliation which may result in cleaner stacks.

Twisted MoS_2: Heterostructures made from staking two layers of the same material but with a relative twist angle lead to different properties compared to its natural stacking orientation. This is due to the change of the interlayer coupling between the adjacent layers. This interlayer coupling with respect to twist angle was studied for the case of twisted MoS_2 by the means of Raman spectroscopy. The Raman spectra measured on these twisted stacks are in agreement with literature; the interlayer coupling decreases as the twist angle is increased between 0° and 30° and then returns towards its initial value as the angle is increased back to 60°.

For this experiment, we used mechanical exfoliated flakes which made the determination of the relative twist angle difficult and led to different angle possibilities. To facilitate its determination, the MoS_2 stacks could be placed in an STM where atomic resolution would confirm the orientation of the flakes.

Another option would be to attempt to study the effects of interlayer coupling on the electronic structure of twisted bilayer MoS_2 in a dynamical fashion. In recent work by Ribeiro-Palau *et al.*,[86] they created a device that allowed an AFM tip to dynamically modify the rotational angle of a graphene-hBN heterostructure *in situ*. Along the same vein, the MoS_2 stacks could be modified in such a way that the STM tip could modify the twist angle *in situ*, followed by a study of the electronic structure. This would ensure uniformity across the measured samples as the sample has always been subject to the same conditions. Although this would be a difficult task, an STM is readily accessible in Dr. Luican-Mayer's lab where it can also be operated in AFM mode, as in the work done by Ribeiro-Palau *et al.*

Chapter 6

Appendices

6.1 Appendix 1 - Graphene as seen on various substrates

Graphene and other monolayer two-dimensional materials measure less than 1nm in thickness and it would not be surprising that they appear optically invisible on some substrates. Luckily, when exfoliated on a silicon substrate with a 285nm native oxide layer, which is the typical choice of substrate in our lab, the flakes are visible. This is not true for all substrates. In fact, for silicon oxide substrates, flakes of graphene achieve a maximum contrast when the oxide layer measures 90nm and 280nm[33] but there is a quick drop off around these points which make the search for graphene extremely difficult on any other thickness. By considering Fresnel's equations, it is straight forward to calculate the expected contrast of graphene on a Si/SiO_2 for any oxide thickness. We define contrast as

$$Contrast = \frac{R_g - R_b}{R_b}$$

where R_g is the reflected intensity from the graphene flake and R_b is the reflected intensity from the Si/SiO_2 (the background).

First, let us calculate the reflected light from a bare substrate (figure 6.1a). That is, the incident light from the microscope is passing from air and reflecting off an oxide layer with thickness d_2, followed by a reflection off of the silicon where we consider it to have an infinite thickness. These three zones have respective index of refractions $n_{air} = 1$,

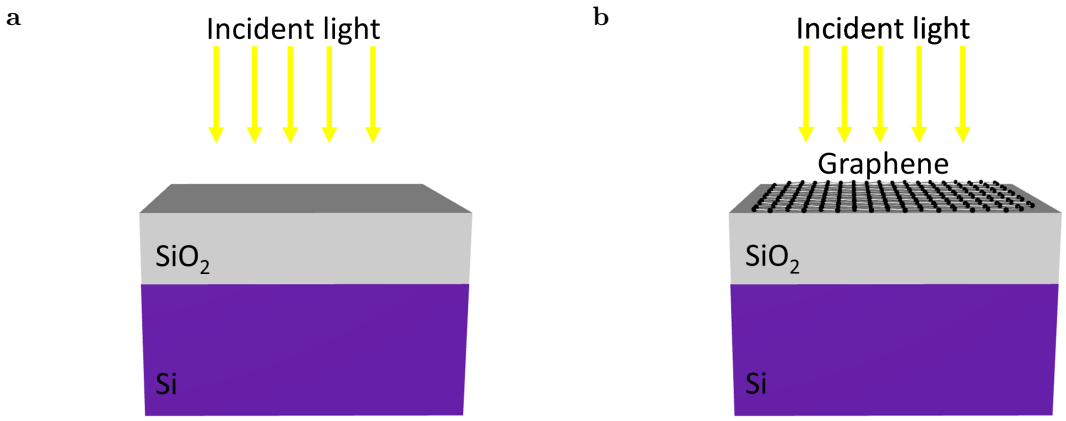

Figure 6.1: The optical system used in the contrast calculations where incident light encounters **(a)** a bare Si/SiO_2 substrate or **(b)** a graphene flake on a Si/SiO_2 substrate.

n_{SiO_2}, and n_{Si}, where both the Si and SiO_2 are wavelength dependent.[87–89]

In the first zone (air), we have an incident and reflected electromagnetic wave. In the second zone (SiO_2), we have a transmitted and reflected electromagnetic wave. Finally in the last zone (Si), we simply have a transmitted electromagnetic wave resulting in the following electric and magnetic fields:

$$E(z) = \begin{cases} E^I_{air} + E^R_{air} = E^+_{air} e^{-k_{air} z} + E^-_{air} e^{k_{air} z} & z < 0 \\ E^I_{SiO_2} + E^R_{SiO_2} = E^+_{SiO_2} e^{-k_{SiO_2} z} + E^-_{SiO_2} e^{k_{SiO_2} z} & 0 < z < d_2 \\ E^T_{Si} = E^+_{Si} e^{-k_{Si}(z-d_2)} & z > d_2 \end{cases}$$

$$B(z) = \begin{cases} B^I_{air} + B^R_{air} = \dfrac{n_{air} E^+_{air}}{c} e^{-k_{air} z} - \dfrac{n_{air} E^-_{air}}{c} e^{k_{air} z} & z < 0 \\ B^I_{SiO_2} + B^R_{SiO_2} = \dfrac{n_{SiO_2} E^+_{SiO_2}}{c} e^{-k_{SiO_2} z} - \dfrac{n_{SiO_2} E^-_{SiO_2}}{c} e^{k_{SiO_2} z} & 0 < z < d_2 \\ B^T_{Si} = \dfrac{n_{Si} E^+_{Si}}{c} e^{-k_{Si}(z-d_2)} & z > d_2 \end{cases}$$

The boundary conditions for the electric field and magnetic field at each interface ensures continuity therefore we have

$$\text{At } z = 0 \qquad \begin{cases} E^+_{air} + E^-_{air} = E^+_{SiO_2} + E^-_{SiO_2} \\ n_{air}(E^+_{air} + E^-_{air}) = n_{SiO_2}(E^+_{SiO_2} - E^-_{SiO_2}) \end{cases}$$

$$\text{At } z = d_2 \qquad \begin{cases} E^+_{SiO_2} e^{-k_{SiO_2} d_2} + E^-_{SiO_2} e^{k_{SiO_2} d_2} = E^+_{Si} + E^-_{Si} \\ n_{SiO_2}(E^+_{SiO_2} e^{-k_{SiO_2} d_2} + E^-_{SiO_2} e^{k_{SiO_2} d_2}) = n_{Si}(E^+_{Si} - E^-_{Si}) \end{cases}$$

We can rewrite these equations in matrix notation:

$$\begin{bmatrix} E^+_{air} \\ E^-_{air} \end{bmatrix} = \frac{1}{t_0} \begin{bmatrix} 1 & r_0 \\ r_0 & 1 \end{bmatrix} \begin{bmatrix} E^+_{SiO_2} \\ E^-_{SiO_2} \end{bmatrix} = \frac{1}{t_0 t_{d_2}} \begin{bmatrix} 1 & r_0 \\ r_0 & 1 \end{bmatrix} \begin{bmatrix} e^{i\phi_{d_2}} & r_{d_2} e^{i\phi_{d_2}} \\ r_{d_2} e^{-i\phi_{d_2}} & e^{-i\phi_{d_2}} \end{bmatrix} \begin{bmatrix} E^+_{Si} \\ E^-_{Si} \end{bmatrix}$$

where

$$r_0 = \frac{n_{air} - n_{SiO_2}}{n_{air} + n_{SiO_2}}, \qquad r_{d_2} = \frac{n_{SiO_2} - n_{Si}}{n_{SiO_2} + n_{Si}}, \qquad t_0 = \frac{2n_{air}}{n_{air} + n_{SiO_2}}$$
$$t_{d_2} = \frac{2n_{SiO_2}}{n_{SiO_2} + n_{Si}}, \qquad \phi_{d_2} = \frac{2\pi n_{SiO_2} d_2}{\lambda}, \qquad E^-_{Si} = 0$$

We are interested in the reflected intensity and therefore want to find the value of $|E^-_{air}|^2$. By considering the 2x2 matrix found above, E^-_{air} is given as the ratio of the (2,1) element and the (1,1) element multiplied by the E^+_{air} which we can take as 1. We then obtain

$$R_b = |E^-_{air}|^2 = \left| \frac{r_0 e^{i\phi_{d_2}} + r_{d_2} e^{-i\phi_{d_2}}}{e^{i\phi_{d_2}} + r_0 r_{d_2} e^{-i\phi_{d_2}}} \right|^2$$

Now let's redo this calculation for the case where we have a graphene flake on the substrate (figure 6.1b). That is, we have 4 zones: air, graphene, SiO_2, and Si, where graphene has a thickness d_1 and again, SiO_2 has a thickness d_2 . Similarly, we obtain the following equation

$$\begin{bmatrix} E^+_{air} \\ E^-_{air} \end{bmatrix} = \frac{1}{t_0 t_{d1} t_{d2}} \begin{bmatrix} e^{i(\phi_{d_1} + \phi_{d_2})} + r_0 r_{d_1} e^{-i(\phi_{d_1} - \phi_{d_2})} + r_0 r_{d_2} e^{-i(\phi_{d_1} + \phi_{d_2})} + r_{d_1} r_{d_2} e^{i(\phi_{d_1} - \phi_{d_2})} & \dots \\ r_0 e^{i(\phi_{d_1} + \phi_{d_2})} + r_{d_1} e^{-i(\phi_{d_1} - \phi_{d_2})} + r_{d_2} e^{-i(\phi_{d_1} + \phi_{d_2})} + r_0 r_{d_1} r_{d_2} e^{i(\phi_{d_1} - \phi_{d_2})} & \dots \end{bmatrix}$$

$$\begin{bmatrix} \dots & e^{i(\phi_{d_1}+\phi_{d_2})} + r_0 r_{d_1} e^{-i(\phi_{d_1}-\phi_{d_2})} + r_0 r_{d_2} e^{-i(\phi_{d_1}+\phi_{d_2})} + r_{d_1} r_{d_2} e^{i(\phi_{d_1}-\phi_{d_2})} \\ \dots & r_0 e^{i(\phi_{d_1}+\phi_{d_2})} + r_{d_1} e^{-i(\phi_{d_1}-\phi_{d_2})} + r_{d_2} e^{-i(\phi_{d_1}+\phi_{d_2})} + r_0 r_{d_1} r_{d_2} e^{i(\phi_{d_1}-\phi_{d_2})} \end{bmatrix} \begin{bmatrix} E^+_{Si} \\ E^-_{Si} \end{bmatrix}$$

where

$$r_0 = \frac{n_{air} - n_g}{n_{air} + n_g}, \qquad r_{d_1} = \frac{n_g - n_{SiO_2}}{n_g + n_{SiO_2}}, \qquad r_{d_2} = \frac{n_{SiO_2} - n_{Si}}{n_{SiO_2} + n_{Si}}, \qquad t_0 = \frac{2n_{air}}{n_{air} + n_g}$$

$$t_{d_1} = \frac{2n_g}{n_g + n_{SiO_2}}, \qquad t_{d_2} = \frac{2n_{SiO_2}}{n_{SiO_2} + n_{Si}}, \qquad \phi_{d_1} = \frac{2\pi n_g d_1}{\lambda}, \qquad \phi_{d_2} = \frac{2\pi n_{SiO_2} d_2}{\lambda}$$

The value of d_1 is the thickness of the graphene flake but can be multiplied by any integer to represent multi-layered graphene. We take this value to be the distance between layers of graphene: $d_1 = 0.335$nm.[90] Graphene's index of refraction is also wavelength dependent and is simply taken as graphite's index of refraction.[91] Once again, we are looking for the reflected intensity therefore we only need the (1,1) and (2,1) elements of the previous matrix equation. This gives us the following intensity

$$R_g = |E^-_{air}|^2 = \left| \frac{r_0 e^{i(\phi_{d_1}+\phi_{d_2})} + r_{d_1} e^{-i(\phi_{d_1}-\phi_{d_2})} + r_{d_2} e^{-i(\phi_{d_1}+\phi_{d_2})} + r_0 r_{d_1} r_{d_2} e^{i(\phi_{d_1}-\phi_{d_2})}}{e^{i(\phi_{d_1}+\phi_{d_2})} + r_0 r_{d_1} e^{-i(\phi_{d_1}-\phi_{d_2})} + r_0 r_{d_2} e^{-i(\phi_{d_1}+\phi_{d_2})} + r_{d_1} r_{d_2} e^{i(\phi_{d_1}-\phi_{d_2})}} \right|^2$$

To really show that an oxide layer of either 90nm or 280nm provides the best contrast for graphene, figure 6.2a provides a color map where the contrast is plotted as a function of both wavelength and oxide thickness. The eye is most sensitive to green light and therefore we look for the oxide layer that corresponds to a maximum contrast along this wavelength (555nm) which corresponds to oxide layers of 88.28nm and 278.53nm (figure 6.2b).

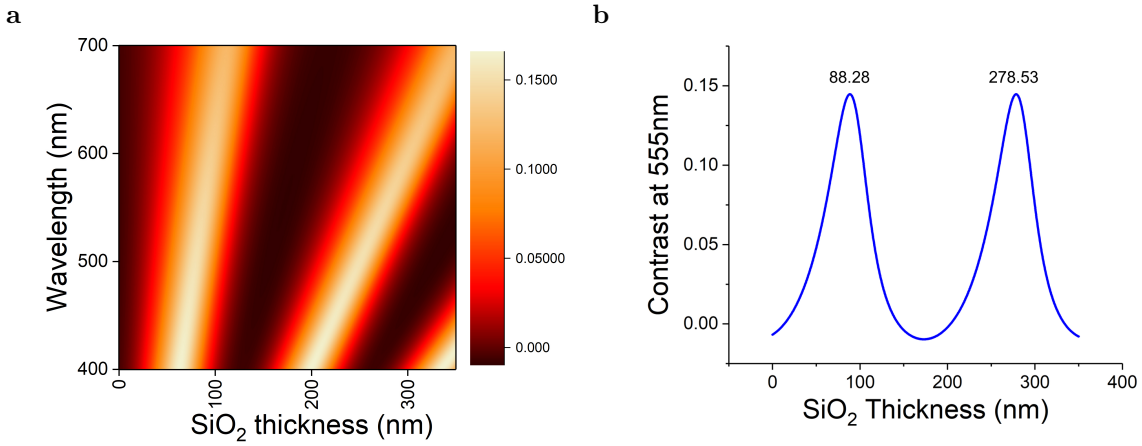

Figure 6.2: **a)** A color plot of the contrast of graphene on a Si/SiO_2 substrate as a function of incident wavelength and SiO_2 thickness. **b)** A slice of the color plot at $\lambda = 555nm$ displaying maximum contrast for SiO_2 thicknesses of 90nm and 280nm.

When the task came to making van der Waals heterostructures using the stamping technique, graphene or other 2D materials were being exfoliated on a Si/SiO_2 substrate that has been previously coated with a layer of PPC. First attempts were made by spin coating the substrate at 1500rpm which resulted in a thickness of 1830nm. At this thickness it seemed nearly impossible to find monolayer graphene. The next attempt resulted in a thickness of 1160nm where the substrate was spun at 3000rpm. At this thickness, we were able to locate monolayer flakes.

To find the PPC thickness that relates to the best possible contrast, we consider a similar scenario to the one above where we again have two cases. First case is when incident light reflects off of a PPC film ($n_{PPC} = 1.463$[92]), followed by a reflection off of SiO_2, and finally off of Si. In the second case, we simply add monolayer graphene before the PPC. This results in the following two equations for the reflected intensities:

$$R_b = \left| \frac{r_0 e^{i(\phi_{d_2}+\phi_{d_3})} + r_{d_2} e^{-i(\phi_{d_2}-\phi_{d_3})} + r_{d_3} e^{-i(\phi_{d_2}+\phi_{d_3})} + r_0 r_{d_2} r_{d_3} e^{i(\phi_{d_2}-\phi_{d_3})}}{e^{i(\phi_{d_2}+\phi_{d_3})} + r_0 r_{d_2} e^{-i(\phi_{d_2}-\phi_{d_3})} + r_0 r_{d_3} e^{-i(\phi_{d_2}+\phi_{d_3})} + r_{d_2} r_{d_3} e^{i(\phi_{d_2}-\phi_{d_3})}} \right|^2$$

$$R_g = \left| \frac{c}{a} \right|^2$$

where

$$c = r_{d_0}e^{i(\phi_{d_1}+\phi_{d_2}+\phi_{d_3})} + r_{d_1}e^{-i(\phi_{d_1}-\phi_{d_2}-\phi_{d_3})} + r_{d_2}e^{-i(\phi_{d_1}+\phi_{d_2}-\phi_{d_3})} + r_{d_3}e^{-i(\phi_{d_1}+\phi_{d_2}+\phi_{d_3})}$$
$$+r_{d_0}r_{d_1}r_{d_2}e^{i(\phi_{d_1}-\phi_{d_2}+\phi_{d_3})} + r_{d_0}r_{d_2}r_{d_3}e^{i(\phi_{d_1}+\phi_{d_2}-\phi_{d_3})} + r_{d_0}r_{d_1}r_{d_3}e^{i(\phi_{d_1}-\phi_{d_2}-\phi_{d_3})} + r_{d_1}r_{d_2}r_{d_3}e^{i(\phi_{d_1}-\phi_{d_2}+\phi_{d_3})}$$

$$a = e^{i(\phi_{d_1}+\phi_{d_2}+\phi_{d_3})} + r_{d_0}r_{d_1}e^{-i(\phi_{d_1}-\phi_{d_2}-\phi_{d_3})} + r_{d_0}r_{d_2}e^{-i(\phi_{d_1}+\phi_{d_2}-\phi_{d_3})} + r_{d_0}r_{d_3}e^{-i(\phi_{d_1}+\phi_{d_2}+\phi_{d_3})}$$
$$+r_{d_1}r_{d_2}e^{i(\phi_{d_1}-\phi_{d_2}+\phi_{d_3})} + r_{d_1}r_{d_3}e^{i(\phi_{d_1}-\phi_{d_2}-\phi_{d_3})} + r_{d_2}r_{d_3}e^{i(\phi_{d_1}+\phi_{d_2}-\phi_{d_3})} + r_{d_0}r_{d_1}r_{d_2}r_{d_3}e^{-i(\phi_{d_1}-\phi_{d_2}+\phi_{d_3})}$$

$$r_0 = \frac{n_{air}-n_g}{n_{air}+n_g}, \qquad r_{d_1} = \frac{n_g-n_{PPC}}{n_g+n_{PPC}}, \qquad r_{d_2} = \frac{n_{PPC}-n_{SiO_2}}{n_{PPC}+n_{SiO_2}}, \qquad r_{d_3} = \frac{n_{SiO_2}-n_{Si}}{n_{SiO_2}+n_{Si}},$$

$$\phi_{d_1} = \frac{2\pi n_g d_1}{\lambda}, \qquad \phi_{d_2} = \frac{2\pi n_{PPC} d_2}{\lambda}, \qquad \phi_{d_3} = \frac{2\pi n_{SiO_2} d_3}{\lambda},$$

From these equations, we can once again plot a color map as well as contrast plot at 555nm (figure 6.3). From the color map, we see that for all thicknesses, there are wavelengths for which the contrast is high and therefore, applying particular filters could facilitate the location of the flakes. The contrast plot for 555nm suggests that tuning the PPC thickness to 1133nm, 1323nm, 1513nm, 1703nm, or 1893nm would generate the best contrast. Coming back to the thicknesses obtained previously, a PPC thickness of 1830nm corresponds to a 1% contrast whereas a thickness of 1160nm corresponds to a 6% contrast. These values explain why we could see the graphene on a layer of PPC spun at 3000rpm and could not when it was spun at 1500rpm. Of course, by tuning in to a thickness that corresponds to a maximum in figure 6.3b, the contrast would be improved and graphene would be easier to find. A similar calculation can be done for various 2D materials and polymers.

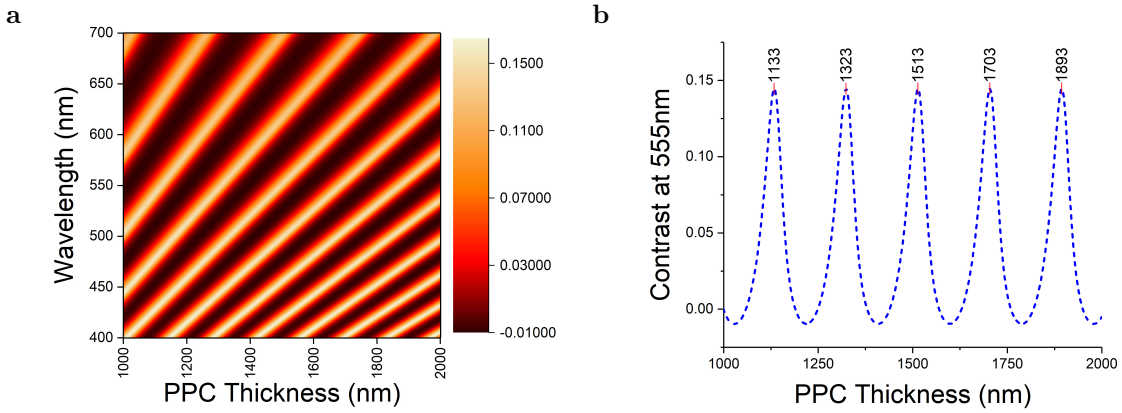

Figure 6.3: **a)** A color plot of the contrast of single layer graphene on a PPC covered Si/SiO_2 substrate (285nm SiO_2) as a function of incident wavelength and PPC thickness. **b)** A slice of the color plot at $\lambda = 555nm$ displaying maximum contrast for PPC thicknesses of 1133nm, 1323nm, 1513nm, 1703nm, and 1893nm.

6.2 Transfer Examples

The goal of this section is to show examples of each transfer method being used.

PMMA-PVA Technique

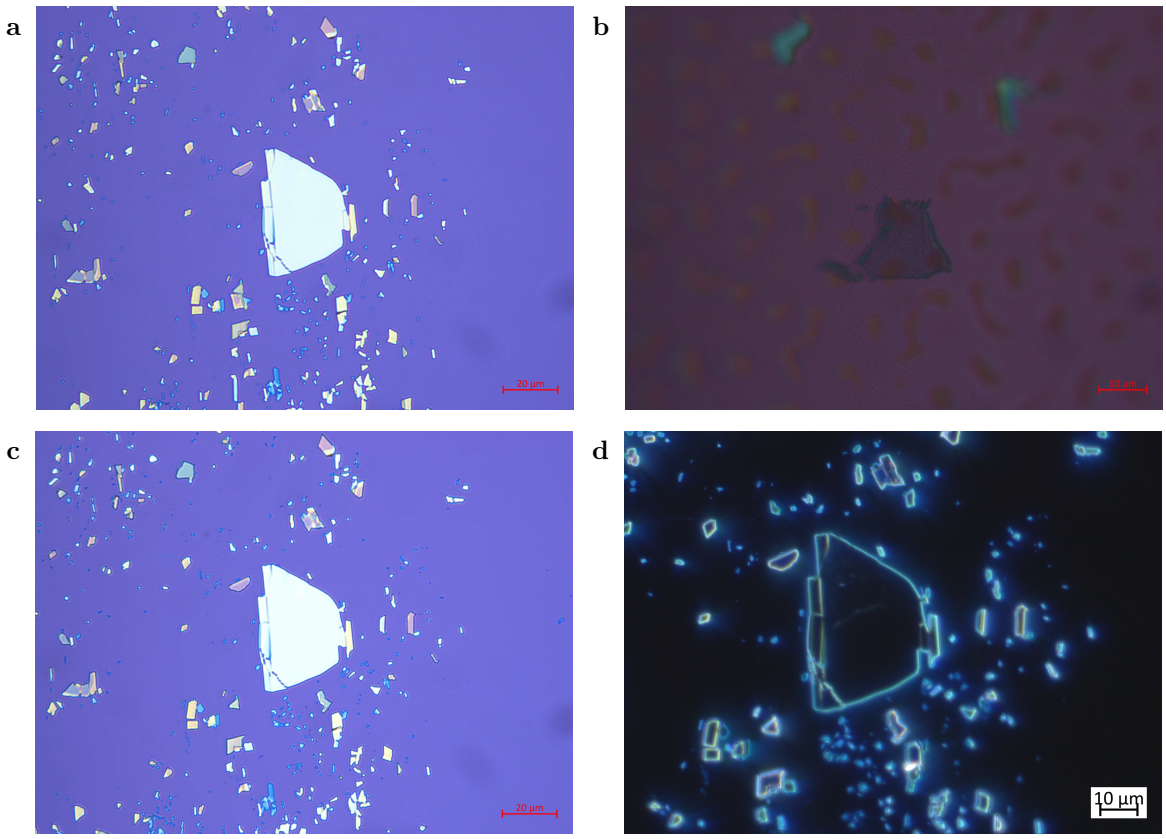

Figure 6.4: Optical images of a transfer using the PMMA-PVA technique. **a)** 50X image of a ReS_2 flake exfoliated on a Si/SiO_2 substrate. **b)** 100X image of a graphene flake on a PMMA film. **c)** 50X brightfield image of the flake from **(b)** transfered on the flake in **(a)**. The top flake is invisible in this image. **d)** A darkfield image of **(c)** where the top flake is now visible.

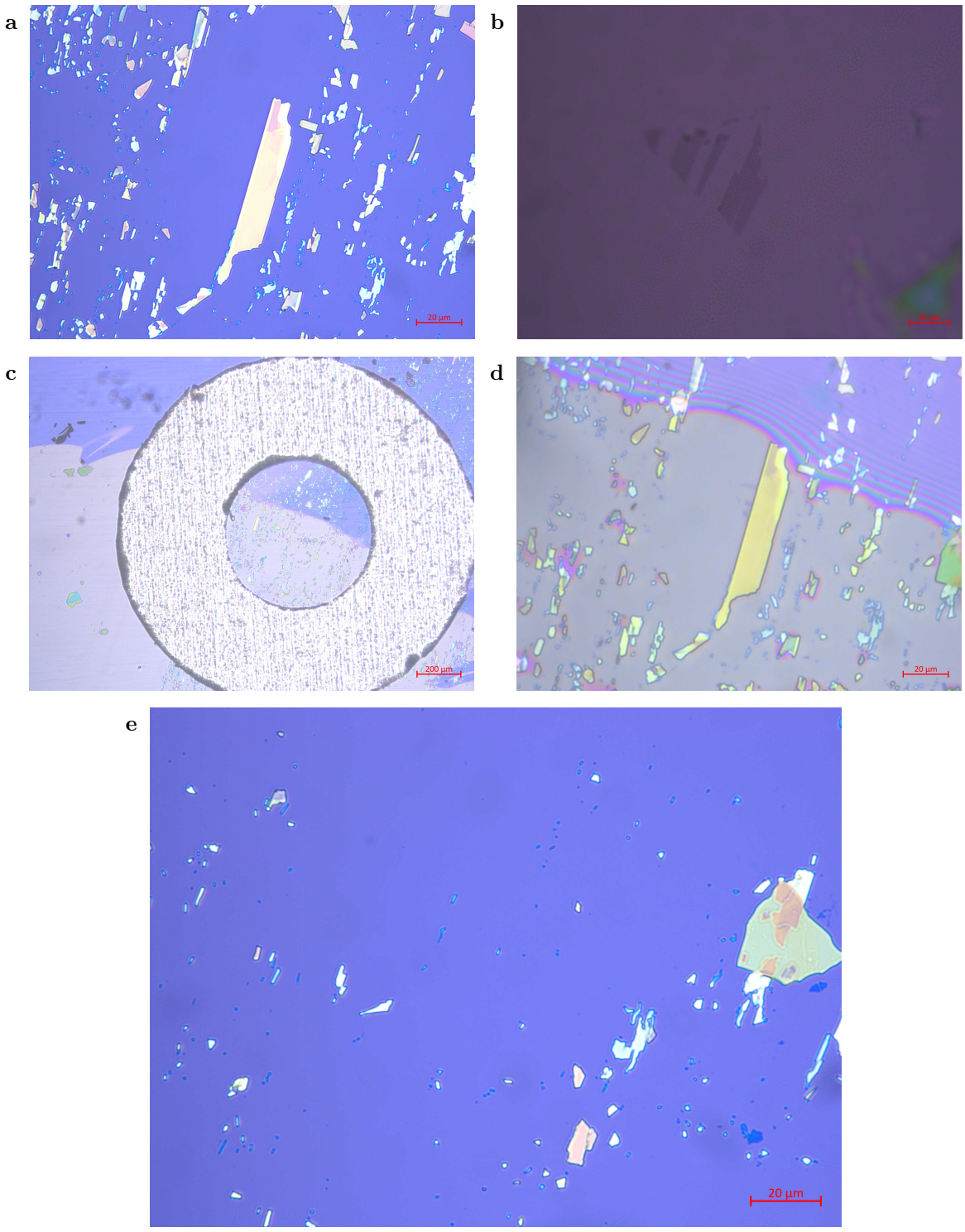

Figure 6.5: Optical images of a transfer using the PMMA-PVA technique. **a)** 50X image of a ReS_2 flake exfoliated on a Si/SiO_2 substrate. **b)** 100X image of a graphene flake on a PMMA film. **c)** 5X optical image mid transfer showing the washer and the change of color as the PMMA comes into contact with the substrate. **d)** 50X image of **(c)**. **e)** 50X image after cleaning away the PMMA. This step also washed away the stack.

Stamping Technique

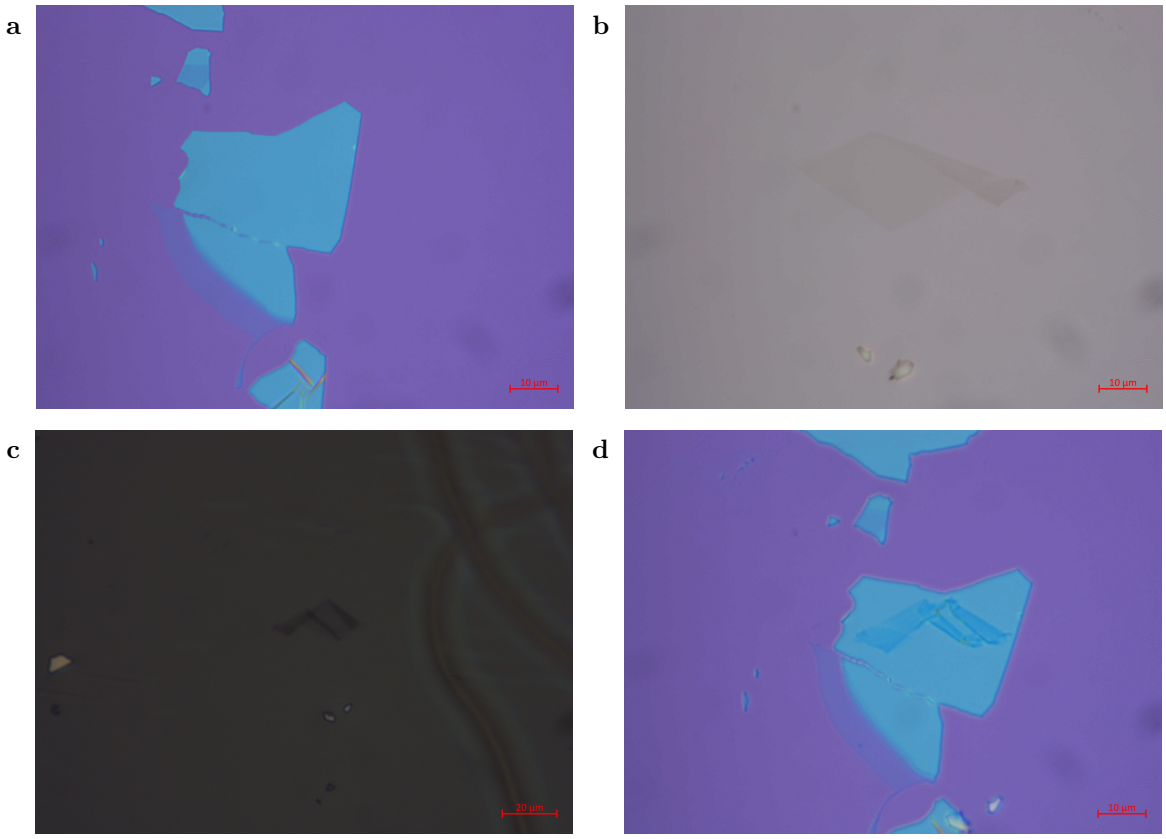

Figure 6.6: Optical images of a transfer using the stamping technique. **a)** 100X image of an hBN flake exfoliated on a Si/SiO_2 substrate. **b)** 100X image of a graphene flake exfoliated on a PPC covered Si/SiO_2 substrate. **c)** 50X image of the flake from **(b)** transfered on a PDMS stamp. The transfer resulted in a curled graphene flake. **d)** 100X image of the resulting transfer.

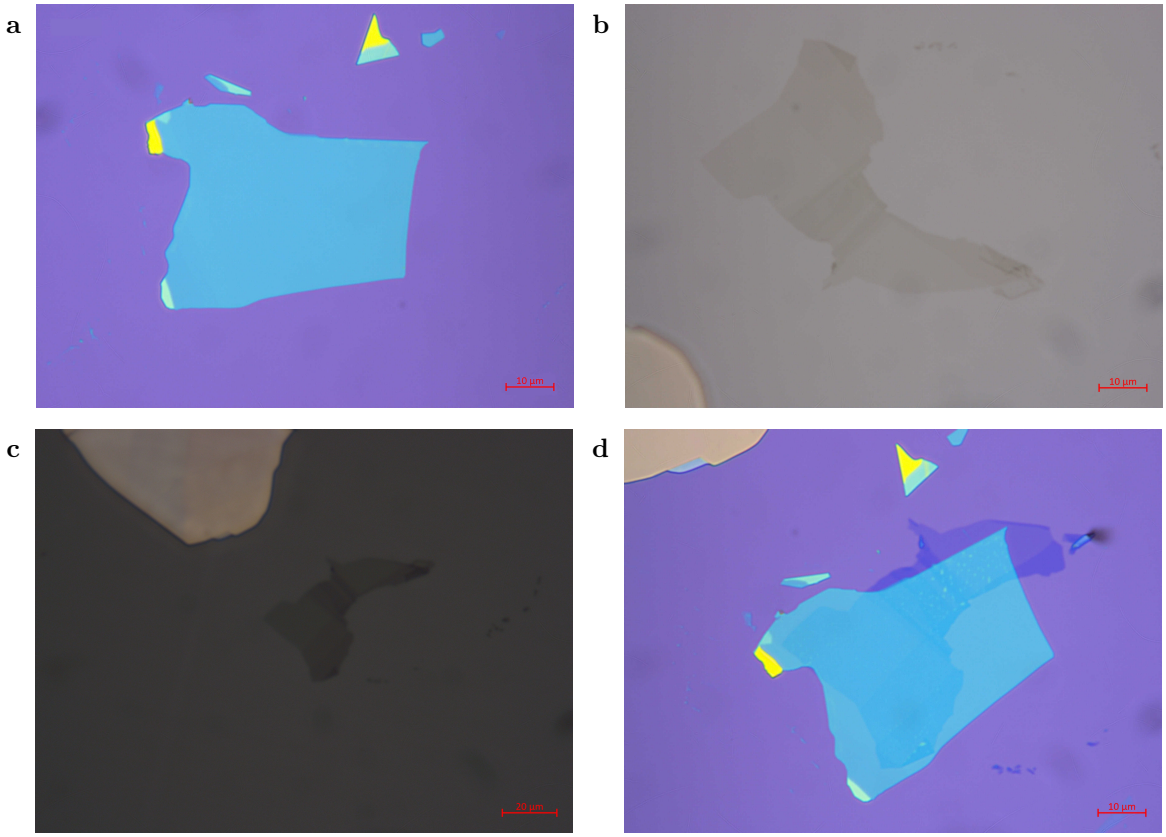

Figure 6.7: Optical images of a transfer using the stamping technique. **a)** 100X image of an hBN flake exfoliated on a Si/SiO_2 substrate. **b)** 100X image of a graphene flake exfoliated on a PPC covered Si/SiO_2 substrate. **c)** 50X image of the flake from **(b)** transfered on a PDMS stamp. **d)** 100X image of the resulting transfer showing a clean area and an area with multiple little bubbles.

Pick-up Technique

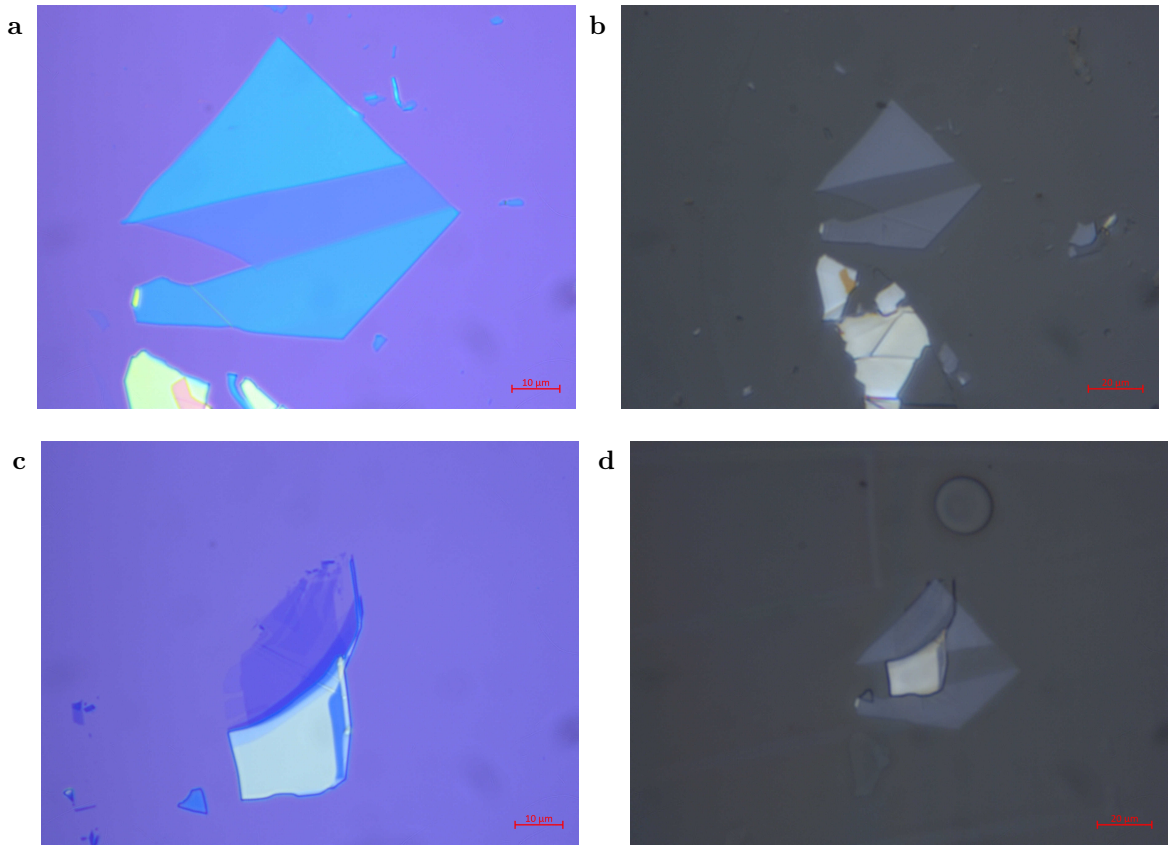

Figure 6.8: Optical images of a transfer using the pick-up technique. **a)** 100X image of an hBN flake exfoliated on a Si/SiO_2 substrate. **b)** 50X image of this same hBN flake picked up on a PDMS stamp. **c)** 100X image of a graphene flake exfoliated on a Si/SiO_2 substrate. **d)** 50X image of this same graphene flake picked up using the hBN flake from **(a-b)**.

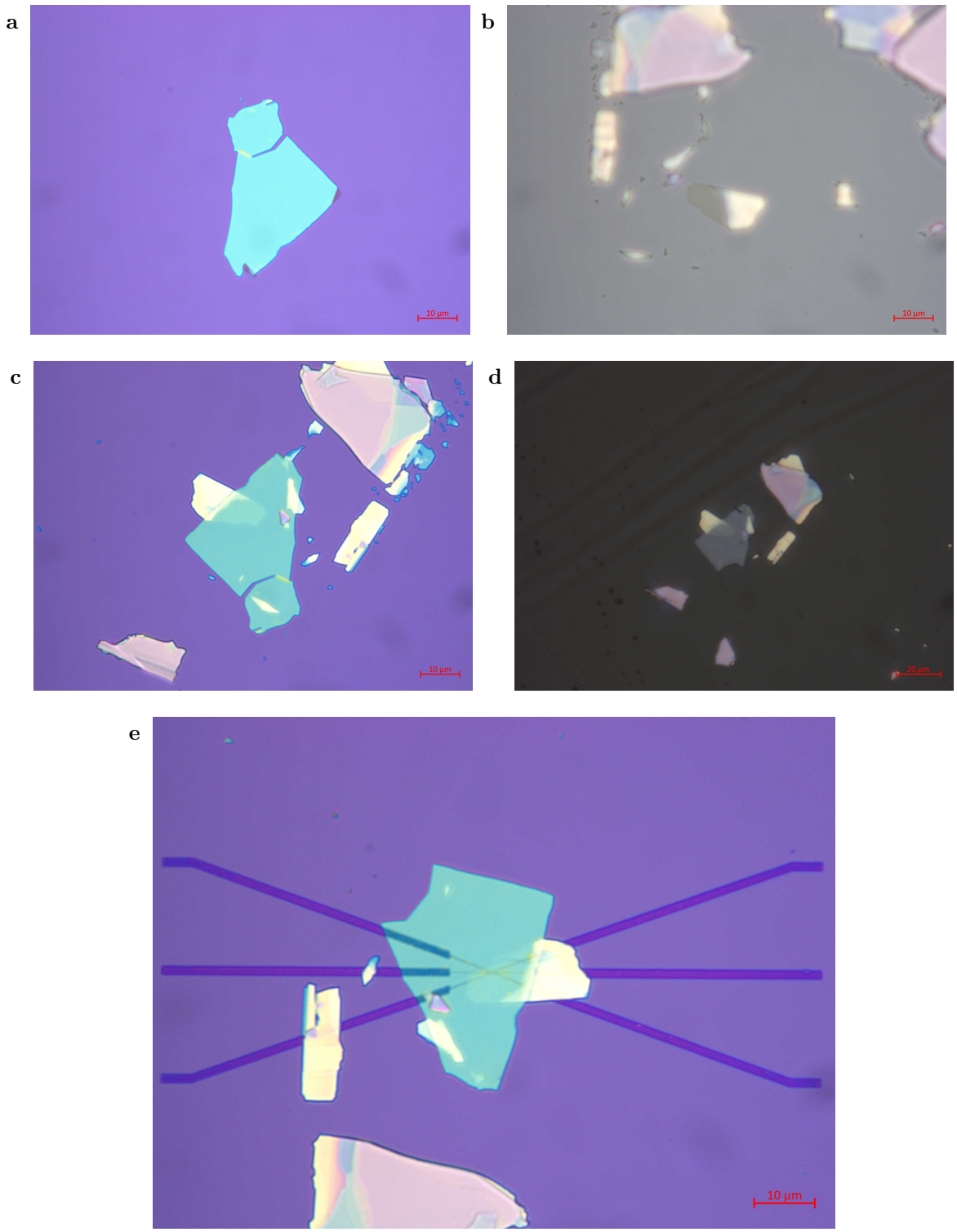

Figure 6.9: Optical images of a transfer using the pick-up technique. **a)** 100X image of an hBN flake exfoliated on a Si/SiO_2 substrate. **b)** 100X image of an MoS_2 flake exfoliated on a PPC covered susbtrate. **c)** 100X image of the flake from **(b)** transfered on the hBN flake in **(a)** using the stamping technique. **d)** 50X image of the MoS_2/hBN stack picked-up and on a stamp. **e)** 100X image of the stack transfered on gold contacts.

6.3 Electron-Beam Procedure for Device Fabrication

Three major steps are involved in the fabrication of any device: spin-coating, electron-beam (e-beam) lithography, and e-beam metal evaporation. However, the road to a complete device involves repeating these steps several times.

Before providing the protocol for each major step, let us walk through the various stages.

1. E-beam resist Spin: Alignment Grid
2. E-beam: Alignment Grid
3. Metal Evaporation: Alignment Grid
4. Lift-off Procedure
5. Introduction of Crystal on Alignment Grid
6. E-beam resist Spin: Contacts
7. E-Beam: Contacts
8. Metal Evaporation: Contacts
9. Lift-off Procedure

The reason for the alignment grid is to allow us to localize the crystal on the substrate when patterning the electrical contacts as we do not want to pre-expose the area of interest.

Spin-coating

For our devices, we opt for a bi-layer spin (two-layers of e-beam resist) which plays an important role during the metal evaporation and lift-off step (see figure 6.10).

First resist layer: The first layer of e-beam resist is a layer of 495K PMMA A6 where this process results in a thickness of 260nm.

- The bare substrate is placed in the spin-coater.
- 495K PMMA A6 is deposited on the substrate.
- The substrate is accelerated to an angular velocity of 1000rpm over a period of 15 seconds.
- The substrate is again accelerated to an angular velocity of 3000rpm over a period of 10 seconds where it will remain at this velocity for an additional 90 seconds.
- The substrate decelerates at a constant rate for 20 seconds until it comes to a complete stop.
- The substrate is placed on a hot plate at 200°C to bake in air for 1 hour.

Second resist layer: The second layer of e-beam resist is a layer of 950K PMMA A2 where this process results in a thickness of 80nm.

- The substrate is placed in the spin-coater.
- 950K PMMA A2 is deposited on the substrate.
- The substrate is accelerated to an angular velocity of 1000rpm over a period of 10 seconds.
- The substrate is again accelerated to an angular velocity of 6000rpm over a period of 15 seconds where it will remain at this velocity for an additional 30 seconds.
- The substrate decelerates at a constant rate for 20 seconds until it comes to a complete stop.
- The substrate is placed on a hot plate at 200°C to bake in air for 1 hour.

E-beam lithography

The Raith Pioneer e-beam system was used where standard e-beam protocol was followed. Here we will present the exposure parameters associated to our e-beam resist.

- Steps: 0.02μm
- Dwell time: 0.0027ms
- Dose: 151.617$\frac{\mu C}{cm^2}$
- Speed: 7.407$\frac{mm}{s}$

Following the exposure, the substrate is placed in a Petri dish where it will undergo its development stage. The Petri dish is filled with 1 part MIBK and 3 parts IPA and is set at a temperature of 20°C. The substrate remains in the dish for exactly 2 minutes, then is rinsed with IPA and blow dried using an N_2 gun.

Metal Evaporation

We use the e-beam metal evaporator which is part of the Angstrom Nexdep Series metal evaporator to deposit metal on our patterned substrate. Gold is typically used to make the metal contacts however a small amount of titanium is evaporated before the gold to help it adhere more firmly to the substrate. For example, when making the alignment grids, we evaporate 3nm of titanium followed by 50nm of gold.

Lift-off Procedure

The substrate is placed and held vertically in an acetone filled vial where it remains for a couple of hours. If all the PMMA has not fallen off by that time, the vial is placed in an ultrasonic bath where it will receive a short pulse usually resulting in the falling of the remaining PMMA.

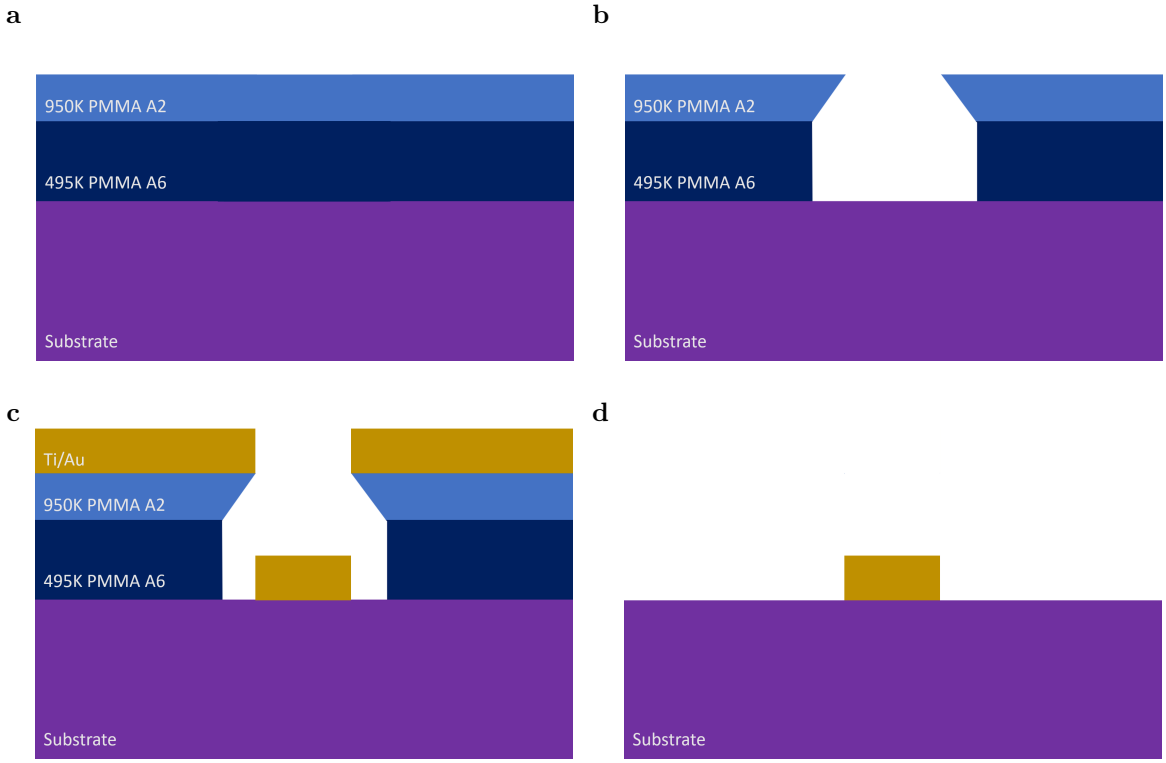

Figure 6.10: **a)** A substrate is coated with two layers of e-beam resist. **b)** The pattern is written into the resist using the e-beam. **c)** Metal is evaporated onto the surface of the substrate and polymer. **d)** The acetone from the lift-off procedure disolves the PMMA causing the gold to only stay on the substrate. Due to the bi-polymer spin, there is a broken connection between the metal on the substrate and the metal on the polymer which reduces the odds of a failed lift-off.

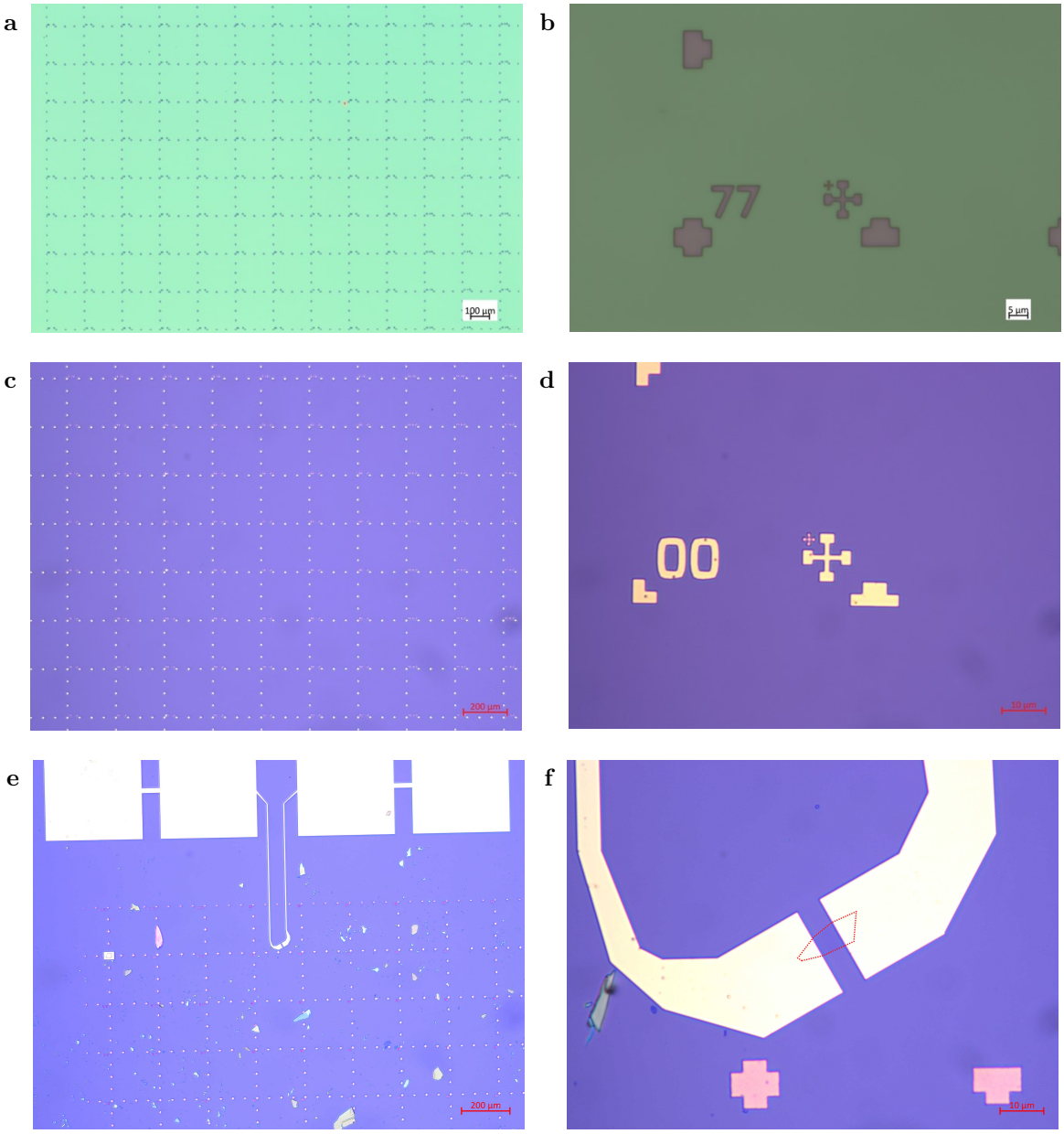

Figure 6.11: **(a-b)** Optical images taken after e-beam and development of the alignment grid. **(c-d)** Optical images taken after metal deposition of the alignment grid. **(e-f)** Optical images of a graphene device made on the aligment grid.

6.4 LabVIEW Program for Microscope User-Interface

In this section, we will present the functions that are used to control the manipulators and which can be found on the user interface. Figure 6.12 shows the user interface where figure 6.12a is the main tab used for everyday operation. The main tab is separated into two parts: the Zaber side and the Mechonics side (as indicated by their logo). Each side is responsible for controlling either the bottom manipulators (Zaber) or the top manipulators (Mechonics). The basic functions are found at this tab. Here, you can move the manipulators in any direction, which includes rotational movement for the bottom stage, you can save desired substrate positions, focus the bottom stage, bring back the manipulators to their initial positions, and bring the manipulators to a stop. The manipulators are coded in such a way that their movement is based on a step motion and not a continuous motion. This was chosen so that the user does not lose control of the manipulators. That being said, there are various step sizes to be chosen from, where a smaller arrow represents a smaller step and a larger arrow represents larger steps. The step sizes also vary depending on the employed lens, *i.e.*, a lower magnification results in larger steps whereas a higher magnification corresponds to smaller steps. If the user wants to employ a continuous motion, the slide bars are available where they can simply input a value and press the "move" button.

When pressing on the "DEV." tab, the user is brought to figure 6.12b. In this tab, the user can see which devices are initialised, send specific commands to chosen devices, and get or change certain settings associated to the manipulators.

Among the long list of possible commands, the most frequently used are: move to either a relative or absolute position, specify the speed at which the manipulator moves to that position, stop all manipulators or a particular manipulator, park the manipulator, get a setting, and change a setting. A full list of commands can be found at https://www.zaber.com/wiki/Manuals/ASCII_Protocol_Manual#Command_Reference.

The get/change setting command that can control many settings and therefore a separate box was created for it. Settings that can be changed or that can be read out include: the acceleration of a manipulator, the currents associated to holding the manipulator in position or to move the manipulator, the temperature of the manipulator's driver,

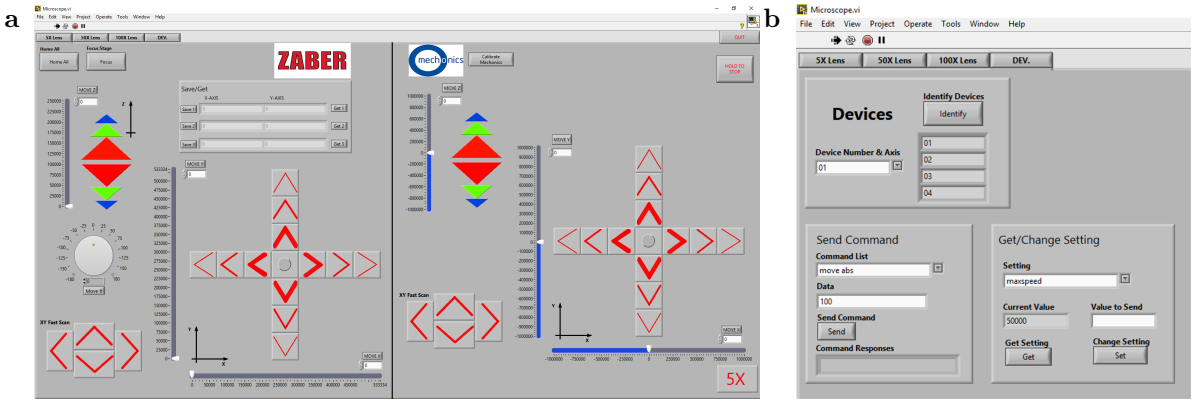

Figure 6.12: LabVIEW user interface used for the transfer setup

the temperature of the unit, the maximum position of a manipulator, the maximum speed of the manipulator, the set speed of the manipulator, the maximum speed of the manipulator when approaching the maximum position, the current position of the manipulator, and the microstep resolution. For a full list of settings, visit https://www.zaber.com/wiki/Manuals/ASCII_Protocol_Manual#Device_Settings.

Each button found on the user-interface references to a case structure in the main code. Figure 6.13 shows the case structure responsible for choosing the correct case structure. The other case structures contain the code responsible for executing the chosen command.

a

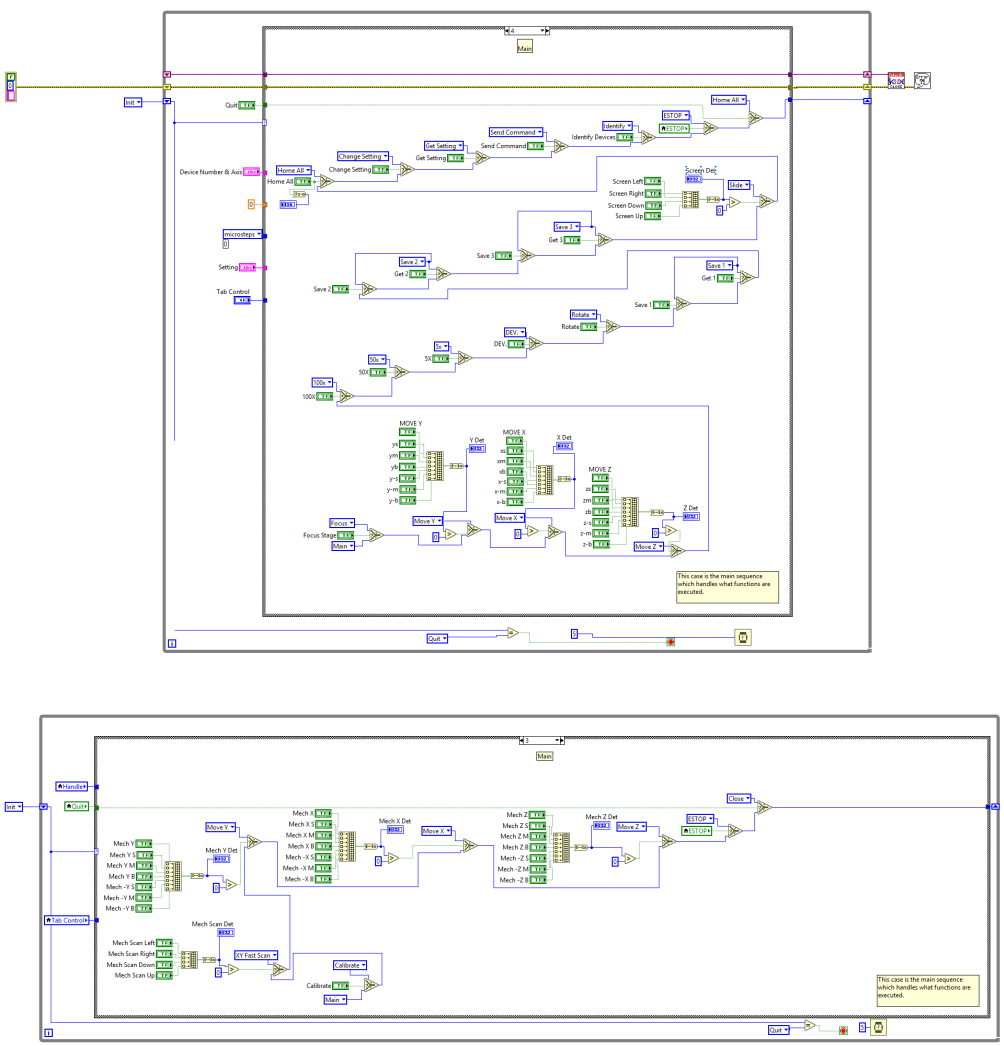

Figure 6.13: LabVIEW code responsible for assigning the appropriate case structure

Bibliography

[1] K. S. Novoselov, D. Jiang, F. Schedin, T. J. Booth, V. V. Khotkevich, S. V. Morozov, and A. K. Geim. Two-dimensional atomic crystals. *Proceedings of the National Academy of Sciences*, 102(30):10451–10453, 2005.

[2] K. S. Novoselov, A. K. Geim, S. V. Morozov, D. Jiang, Y. Zhang, S. V. Dubonos, I. V. Grigorieva, and A. A. Firsov. Electric field effect in atomically thin carbon films. *Science*, 306(5696):666–669, 2004.

[3] Changgu Lee, Xiaoding Wei, Jeffrey W. Kysar, and James Hone. Measurement of the elastic properties and intrinsic strength of monolayer graphene. *Science*, 321(5887):385–388, 2008.

[4] F. Schedin, A. K. Geim, S. V. Morozov, E. W. Hill, P. Blake, M. I. Katsnelson, and K. S. Novoselov. Detection of individual gas molecules adsorbed on graphene. *Nature Materials*, 6:652, 2007.

[5] Girish S. Kulkarni, Karthik Reddy, Wenzhe Zang, Kyunghoon Lee, Xudong Fan, and Zhaohui Zhong. Electrical probing and tuning of molecular physisorption on graphene. *Nano Letters*, 16(1):695–700, 2016.

[6] Tapas R. Nayak, Henrik Andersen, Venkata S. Makam, Clement Khaw, Sukang Bae, Xiangfan Xu, Pui-Lai R. Ee, Jong-Hyun Ahn, Byung Hee Hong, Giorgia Pastorin, and Barbaros Özyilmaz. Graphene for controlled and accelerated osteogenic differentiation of human mesenchymal stem cells. *ACS Nano*, 5(6):4670–4678, 2011.

[7] Gaurav Lalwani, Allan M. Henslee, Behzad Farshid, Liangjun Lin, F. Kurtis Kasper, Yi-Xian Qin, Antonios G. Mikos, and Balaji Sitharaman. Two-dimensional nanostructure-reinforced biodegradable polymeric nanocomposites for bone tissue engineering. *Biomacromolecules*, 14(3):900–909, 2013.

[8] Gaurav Lalwani, Michael D'Agati, Amit Mahmud Khan, and Balaji Sitharaman. Toxicology of graphene-based nanomaterials. *Advanced Drug Delivery Reviews*, 105:109 – 144, 2016. Graphene-based materials in nanomedicine.

[9] Diana Berman, Sanket A. Deshmukh, Subramanian K. R. S. Sankaranarayanan, Ali Erdemir, and Anirudha V. Sumant. Extraordinary macroscale wear resistance of one atom thick graphene layer. *Advanced Functional Materials*, 24(42):6640–6646.

[10] Gaurav Lalwani, Allan M. Henslee, Behzad Farshid, Liangjun Lin, F. Kurtis Kasper, Yi-Xian Qin, Antonios G. Mikos, and Balaji Sitharaman. Two-dimensional nanostructure-reinforced biodegradable polymeric nanocomposites for bone tissue engineering. *Biomacromolecules*, 14(3):900–909, 2013.

[11] J Zupan and D Kolar. Optical properties of graphite and boron nitride. *Journal of Physics C: Solid State Physics*, 5(21):3097, 1972.

[12] John Robertson. Electronic structure and core exciton of hexagonal boron nitride. *Phys. Rev. B*, 29:2131–2137, Feb 1984.

[13] J.A. Wilson and A.D. Yoffe. The transition metal dichalcogenides discussion and interpretation of the observed optical, electrical and structural properties. *Advances in Physics*, 18(73):193–335, 1969.

[14] I. Guillamón, H. Suderow, S. Vieira, L. Cario, P. Diener, and P. Rodière. Superconducting density of states and vortex cores of 2H-NbS_2. *Phys. Rev. Lett.*, 101:166407, Oct 2008.

[15] Pulickel Ajayan, Philip Kim, and Kaustav Banerjee. Two-dimensional van der Waals materials. *Physics Today*, 69:38, 2016.

[16] K. S. Novoselov, A. Mishchenko, A. Carvalho, and A. H. Castro Neto. 2D materials and van der Waals heterostructures. *Science*, 353(6298), 2016.

[17] Kin Fai Mak, Changgu Lee, James Hone, Jie Shan, and Tony F. Heinz. Atomically thin MoS_2: A new direct-gap semiconductor. *Phys. Rev. Lett.*, 105:136805, Sep 2010.

[18] A. Avsar, J. Y. Tan, T. Taychatanapat, J. Balakrishnan, G.K.W. Koon, Y. Yeo, J. Lahiri, A. Carvalho, A. S. Rodin, E.C.T. O'Farrell, G. Eda, A. H. Castro Neto, and B. Özyilmaz. Spin–orbit proximity effect in graphene. *Nature Communications*, 5:4875, 2014.

[19] C. R. Dean, A. F. Young, I. Meric, C. Lee, L. Wang, S. Sorgenfrei, K. Watanabe, T. Taniguchi, P. Kim, K. L. Shepard, and J. Hone. Boron nitride substrates for high-quality graphene electronics. *Nature Nanotechnology*, 5:722–726, Aug 2010.

[20] L. Wang, I. Meric, P. Y. Huang, Q. Gao, Y. Gao, H. Tran, T. Taniguchi, K. Watanabe, L. M. Campos, D. A. Muller, J. Guo, P. Kim, J. Hone, K. L. Shepard, and C. R. Dean. One-dimensional electrical contact to a two-dimensional material. *Science*, 342(6158):614–617, 2013.

[21] Rostislav A. Doganov, Eoin C. T. O'Farrell, Steven P. Koenig, Yuting Yeo, Angelo Ziletti, Alexandra Carvalho, David K. Campbell, David F. Coker, Kenji Watanabe, Takashi Taniguchi, Antonio H. Castro Neto, and Barbaros Özyilmaz. Transport properties of pristine few-layer black phosphorus by van der Waals passivation in an inert atmosphere. *Nature Communications*, 6:6647, 2015.

[22] Y. Cao, A. Mishchenko, G. L. Yu, E. Khestanova, A. P. Rooney, E. Prestat, A. V. Kretinin, P. Blake, M. B. Shalom, C. Woods, J. Chapman, G. Balakrishnan, I. V. Grigorieva, K. S. Novoselov, B. A. Piot, M. Potemski, K. Watanabe, T. Taniguchi, S. J. Haigh, A. K. Geim, and R. V. Gorbachev. Quality heterostructures from two-dimensional crystals unstable in air by their assembly in inert atmosphere. *Nano Letters*, 15(8):4914–4921, 2015.

[23] Woo Jong Yu, Yuan Liu, Hailong Zhou, Anxiang Yin, Zheng Li, Yu Huang, and Xiangfeng Duan. Highly efficient gate-tunable photocurrent generation in vertical heterostructures of layered materials. *Nature Nanotechnology*, 8:952, 2013.

[24] Rui Cheng, Dehui Li, Hailong Zhou, Chen Wang, Anxiang Yin, Shan Jiang, Yuan Liu, Yu Chen, Yu Huang, and Xiangfeng Duan. Electroluminescence and photocurrent generation from atomically sharp WSe_2/MoS_2 heterojunction p–n diodes. *Nano Letters*, 14(10):5590–5597, 2014.

[25] F. S. Ohuchi, B. A. Parkinson, K. Ueno, and A. Koma. van der Waals epitaxial growth and characterization of $MoSe_2$ thin films on SnS_2, journal = Journal of Applied Physics, volume = 68, number = 5, pages = 2168-2175, year = 1990, doi = 10.1063/1.346574,.

[26] W. Gannett, W. Regan, K. Watanabe, T. Taniguchi, M. F. Crommie, and A. Zettl. Boron nitride substrates for high mobility chemical vapor deposited graphene. *Applied Physics Letters*, 98(24):242105, 2011.

[27] Yumeng Shi, Wu Zhou, Ang-Yu Lu, Wenjing Fang, Yi-Hsien Lee, Allen Long Hsu, Soo Min Kim, Ki Kang Kim, Hui Ying Yang, Lain-Jong Li, Juan-Carlos Idrobo, and

Jing Kong. van der Waals epitaxy of MoS_2 layers using graphene as growth templates. *Nano Letters*, 12(6):2784–2791, 2012.

[28] Mark P. Levendorf, , Cheol-Joo Kim, Lola Brown, Pinshane Y. Huang, Robin W. Havener, David A. Muller, and Jiwoong Park. Graphene and boron nitride lateral heterostructures for atomically thin circuitry. *Nature*, 488:627, 2012.

[29] Chunming Huang, , Sanfeng Wu, Ana M. Sanchez, Jonathan J. P. Peters, Richard Beanland, Jason S. Ross, Pasqual Rivera, Wang Yao, David H. Cobden, and Xiaodong Xu. Lateral heterojunctions within monolayer $MoSe_2$–WSe_2 semiconductors. *Nature Materials*, 13:1096, 2014.

[30] Dacheng Wei and Yunqi Liu. Controllable synthesis of graphene and its applications. *Advanced Materials*, 22(30):3225–3241, 2010.

[31] Grégory F. Schneider, Victor E. Calado, Henny Zandbergen, Lieven M. K. Vandersypen, and Cees Dekker. Wedging transfer of nanostructures. *Nano Letters*, 10(5):1912–1916, 2010. PMID: 20402493.

[32] C. R. Dean, A. F. Young, P. Cadden-Zimansky, L. Wang, H. Ren, K. Watanabe, T. Taniguchi, P. Kim, J. Hone, and K. L. Shepard. Multicomponent fractional quantum hall effect in graphene. *Nature Physics*, 7:693–696, May 2011.

[33] P. Blake, E. W. Hill, A. H. Castro Neto, K. S. Novoselov, D. Jiang, R. Yang, T. J. Booth, and A. K. Geim. Making graphene visible. *Applied Physics Letters*, 91(6):063124, 2007.

[34] G. Binnig, C. F. Quate, and Ch. Gerber. Atomic force microscope. *Phys. Rev. Lett.*, 56:930–933, Mar 1986.

[35] G. Binnig, H. Rohrer, Ch. Gerber, and E. Weibel. Surface studies by scanning tunneling microscopy. *Phys. Rev. Lett.*, 49:57–61, Jul 1982.

[36] Q. Zhong, D. Inniss, K. Kjoller, and V.B. Elings. Fractured polymer/silica fiber surface studied by tapping mode atomic force microscopy. *Surface Science*, 290(1):L688 – L692, 1993.

[37] A. C. Ferrari, J. C. Meyer, V. Scardaci, C. Casiraghi, M. Lazzeri, F. Mauri, S. Piscanec, D. Jiang, K. S. Novoselov, S. Roth, and A. K. Geim. Raman spectrum of graphene and graphene layers. *Phys. Rev. Lett.*, 97:187401, Oct 2006.

[38] Andrea C. Ferrari. Raman spectroscopy of graphene and graphite: Disorder, electron–phonon coupling, doping and nonadiabatic effects. *Solid State Communications*, 143(1):47 – 57, 2007. Exploring graphene.

[39] Changgu Lee, Hugen Yan, Louis E. Brus, Tony F. Heinz, James Hone, and Sunmin Ryu. Anomalous lattice vibrations of single and few-layer MoS_2. *ACS Nano*, 4(5):2695–2700, 2010. PMID: 20392077.

[40] Zhen Hua Ni, Ting Yu, Yun Hao Lu, Ying Ying Wang, Yuan Ping Feng, and Ze Xiang Shen. Uniaxial strain on graphene: Raman spectroscopy study and band-gap opening. *ACS Nano*, 2(11):2301–2305, 2008. PMID: 19206396.

[41] Mingyuan Huang, Hugen Yan, Tony F. Heinz, and James Hone. Probing strain-induced electronic structure change in graphene by Raman spectroscopy. *Nano Letters*, 10(10):4074–4079, 2010. PMID: 20735024.

[42] Andres Castellanos-Gomez, Rafael Roldán, Emmanuele Cappelluti, Michele Buscema, Francisco Guinea, Herre S. J. van der Zant, and Gary A. Steele. Local strain engineering in atomically thin MoS_2. *Nano Letters*, 13(11):5361–5366, 2013. PMID: 24083520.

[43] Jun Yan, Yuanbo Zhang, Philip Kim, and Aron Pinczuk. Electric field effect tuning of electron-phonon coupling in graphene. *Phys. Rev. Lett.*, 98:166802, Apr 2007.

[44] Nicola Bonini, Michele Lazzeri, Nicola Marzari, and Francesco Mauri. Phonon anharmonicities in graphite and graphene. *Phys. Rev. Lett.*, 99:176802, Oct 2007.

[45] P. H. Tan, W. P. Han, W. J. Zhao, Z. H. Wu, K. Chang, H. Wang, Y. F. Wang, N. Bonini, N. Marzari, N. Pugno, G. Savini, A. Lombardo, and A. C. Ferrari. The shear mode of multilayer graphene. *Nature Materials*, 11:294–300, Feb 2012.

[46] Chun Hung Lui, Leandro M. Malard, SukHyun Kim, Gabriel Lantz, François E. Laverge, Riichiro Saito, and Tony F. Heinz. Observation of layer-breathing mode vibrations in few-layer graphene through combination raman scattering. *Nano Letters*, 12(11):5539–5544, 2012. PMID: 22963681.

[47] Kaihui Liu, Liming Zhang, Ting Cao, Chenhao Jin, Diana Qiu, Qin Zhou, Alex Zettl, Peidong Yang, Steve G. Louie, and Feng Wang. Evolution of interlayer coupling in twisted molybdenum disulfide bilayers. *Nature Communications*, 5(4966), Sep 2014.

[48] Shengxi Huang, Liangbo Liang, Xi Ling, Alexander A. Puretzky, David B. Geohegan, Bobby G. Sumpter, Jing Kong, Vincent Meunier, and Mildred S. Dresselhaus. Low-frequency interlayer Raman modes to probe interface of twisted bilayer MoS_2. *Nano Letters*, 16(2):1435–1444, 2016. PMID: 26797083.

[49] C. Casiraghi, S. Pisana, K. S. Novoselov, A. K. Geim, and A. C. Ferrari. Raman fingerprint of charged impurities in graphene. *Applied Physics Letters*, 91(23):233108, 2007.

[50] Stephanie Reich and Christian Thomsen. Raman spectroscopy of graphite. *Philosophical Transactions of the Royal Society of London A: Mathematical, Physical and Engineering Sciences*, 362(1824):2271–2288, 2004.

[51] Andrea C. Ferrari and Denis M. Basko. Raman spectroscopy as a versatile tool for studying the properties of graphene. *Nature Nanotechnology*, 8:235, 2013.

[52] P. H. Tan, W. P. Han, W. J. Zhao, Z. H. Wu, K. Chang, H. Wang, Y. F. Wang, N. Bonini, N. Marzari, N. Pugno, G. Savini, A. Lombardo, and A. C. Ferrari. The shear mode of multilayer graphene. *Nature Materials*, 11:294, 2012.

[53] L. G. Cançado, A. Reina, J. Kong, and M. S. Dresselhaus. Geometrical approach for the study of G' band in the Raman spectrum of monolayer graphene, bilayer graphene, and bulk graphite. *Phys. Rev. B*, 77:245408, June 2008.

[54] S. J. Haigh, A. Gholinia, R. Jalil, S. Romani, L. Britnell, D. C. Elias, K. S. Novoselov, L. A. Ponomarenko, A. K. Geim, and R. Gorbachev. Cross-sectional imaging of individual layers and buried interfaces of graphene-based heterostructures and superlattices. *Nature Materials*, 11:764–767, 2012.

[55] A. K. Geim and I. V. Grigorieva. Van der Waals heterostructures. *Nature*, 499:419, 2013.

[56] Lei Wang, Fan Ye, Filippo Pizzocchero, Bjarke S. Jessen, Kenji Watanabe, Takashi Taniguchi, David A. Muller, Tony Low, Philip Kim, and James Hone. Multi-terminal transport measurements of MoS_2 using a van der Waals heterostructure device platform. *Nature Nanotechnology*, 10:534–540, 2015.

[57] Andres Castellanos-Gomez, Michele Buscema, Rianda Molenaar, Vibhor Singh, Laurens Janssen, Herre van der Zant, and Gary A Steele. Deterministic transfer of two-dimensional materials by all-dry viscoelastic stamping. *2D Materials*, 1(1), Apr 2014.

[58] A. V. Kretinin, Y. Cao, J. S. Tu, G. L. Yu, R. Jalil, K. S. Novoselov, S. J. Haigh, A. Gholinia, A. Mishchenko, M. Lozada, T. Georgiou, C. R. Woods, F. Withers, P. Blake, G. Eda, A. Wirsig, C. Hucho, K. Watanabe, T. Taniguchi, A. K. Geim, and R. V. Gorbachev. Electronic properties of graphene encapsulated with different two-dimensional atomic crystals. *Nano Letters*, 14(6):3270–3276, 2014.

[59] Achint Jain, Palash Bharadwaj, Sebastian Heeg, Markus Parzefall, Takashi Taniguchi, Kenji Watanabe, and Lukas Novotny. Minimizing residues and strain in 2d materials transferred from PDMS. *Nanotechnology*, 29(26):265203, 2018.

[60] E. Khestanova, F. Guinea, L. Fumagalli, A. K. Geim, and I. V. Grigorieva. Universal shape and pressure inside bubbles appearing in van der Waals heterostructures. *Nature Communications*, 7:12587, 2016.

[61] Filippo Pizzocchero, Lene Gammelgaard, Bjarke S. Jessen, José M. Caridad, Lei Wang, James Hone, Peter Bøggild, and Timothy J. Booth. The hot pick-up technique for batch assembly of van der Waals heterostructures. *Nature Communications*, 7(11894), 2016.

[62] Jakob Zabel, Rahul R. Nair, Anna Ott, Thanasis Georgiou, Andre K. Geim, Kostya S. Novoselov, and Cinzia Casiraghi. Raman spectroscopy of graphene and bilayer under biaxial strain: Bubbles and balloons. *Nano Letters*, 12(2):617–621, 2012. PMID: 22149458.

[63] Zhuo-Zhi Zhang, Xiang-Xiang Song, Gang Luo, Guang-Wei Deng, Vahid Mosallanejad, Takashi Taniguchi, Kenji Watanabe, Hai-Ou Li, Gang Cao, Guang-Can Guo, Franco Nori, and Guo-Ping Guo. Electrotunable artificial molecules based on van der Waals heterostructures. *Science Advances*, 3(10), 2017.

[64] Riccardo Pisoni, Zijin Lei, Patrick Back, Marius Eich, Hiske Overweg, Yongjin Lee, Kenji Watanabe, Takashi Taniguchi, Thomas Ihn, and Klaus Ensslin. Gate-tunable quantum dot in a high quality single layer MoS_2 van der Waals heterostructure. *Applied Physics Letters*, 112(12):123101, 2018.

[65] Ke Wang, Kristiaan De Greve, Luis A. Jauregui, Andrey Sushko, Alexander High, You Zhou, Giovanni Scuri, Takashi Taniguchi, Kenji Watanabe, Mikhail D. Lukin, Hongkun Park, and Kim. Electrical control of charged carriers and excitons in atomically thin materials. *Nature Nanotechnology*, 13:128, 2018.

[66] Marius Eich, Riccardo Pisoni, Alessia Pally, Hiske Overweg, Annika Kurzmann, Yongjin Lee, Peter Rickhaus, Kenji Watanabe, Takashi Taniguchi, Klaus Ensslin, and Thomas Ihn. Coupled quantum dots in bilayer graphene. *Nano Letters*, 18(8):5042–5048, 2018.

[67] L. Banszerus, B. Frohn, A. Epping, D. Neumaier, K. Watanabe, T. Taniguchi, and C. Stampfer. Gate-defined electron–hole double dots in bilayer graphene. *Nano Letters*, 18(8):4785–4790, 2018.

[68] J. R. Petta, A. C. Johnson, J. M. Taylor, E. A. Laird, A. Yacoby, M. D. Lukin, C. M. Marcus, M. P. Hanson, and A. C. Gossard. Coherent manipulation of coupled electron spins in semiconductor quantum dots. *Science*, 309(5744):2180–2184, 2005.

[69] R. Hanson, L. P. Kouwenhoven, J. R. Petta, S. Tarucha, and L. M. K. Vandersypen. Spins in few-electron quantum dots. *Rev. Mod. Phys.*, 79:1217–1265, Oct 2007.

[70] J. L. Verble and T. J. Wieting. Lattice mode degeneracy in MoS_2 and other layer compounds. *Phys. Rev. Lett.*, 25:362–365, Aug 1970.

[71] Hong Li, Qing Zhang, Chin Chong Ray Yap, Beng Kang Tay, Teo Hang Tong Edwin, Aurelien Olivier, and Dominique Baillargeat. From bulk to monolayer MoS_2: Evolution of Raman scattering. *Advanced Functional Materials*, 22(7):1385–1390.

[72] Xin Zhang, Xiao-Fen Qiao, Wei Shi, Jiang-Bin Wu, De-Sheng Jiang, and Ping-Hen Tan. Phonon and Raman scattering of two-dimensional transition metal dichalcogenides from monolayer, multilayer to bulk material. *Chemical Society Reviews*, 44:2757–2785.

[73] Yanyuan Zhao, Xin Luo, Hai Li, Jun Zhang, Paulo T. Araujo, Chee Kwan Gan, Jumiati Wu, Hua Zhang, Su Ying Quek, Mildred S. Dresselhaus, and Qihua Xiong. Interlayer breathing and shear modes in few-trilayer MoS_2 and WSe_2. *Nano Letters*, 13(3):1007–1015, 2013.

[74] J. Ribeiro-Soares, R. M. Almeida, E. B. Barros, P. T. Araujo, M. S. Dresselhaus, L. G. Cançado, and A. Jorio. Group theory analysis of phonons in two-dimensional transition metal dichalcogenides. *Phys. Rev. B*, 90:115438, Sep 2014.

[75] A.G. Bagnall, W.Y. Liang, E.A. Marseglia, and B. Welber. Raman studies of MoS_2 at high pressure. *Physica B+C*, 99(1):343 – 346, 1980.

[76] T. J. Wieting and J. L. Verble. Interlayer bonding and the lattice vibrations of β-gase. *Phys. Rev. B*, 5:1473–1479, Feb 1972.

[77] A. Luican, Guohong Li, A. Reina, J. Kong, R. R. Nair, K. S. Novoselov, A. K. Geim, and E. Y. Andrei. Single-layer behavior and its breakdown in twisted graphene layers. *Phys. Rev. Lett.*, 106:126802, Mar 2011.

[78] Marco Bernardi, Maurizia Palummo, and Jeffrey C. Grossman. Extraordinary sunlight absorption and one nanometer thick photovoltaics using two-dimensional monolayer materials. *Nano Letters*, 13(8):3664–3670, 2013. PMID: 23750910.

[79] Shengxi Huang, Xi Ling, Liangbo Liang, Jing Kong, Humberto Terrones, Vincent Meunier, and Mildred S. Dresselhaus. Probing the interlayer coupling of twisted bilayer MoS_2.

[80] Kaihui Liu, Liming Zhang, Ting Cao, Chenhao Jin, Diana Qiu, Qin Zhou, Alex Zettl, Peidong Yang, Steve G. Louie, and Feng Wang. Evolution of interlayer coupling in twisted molybdenum disulfide bilayers. *Nature Communications*, 5:4966, 2014.

[81] Andres Castellanos-Gomez, Herre S. J. van der Zant, and Gary A. Steele. Folded MoS_2 layers with reduced interlayer coupling. *Nano Research*, 7(4):572–578, Apr 2014.

[82] Arend M. van der Zande, Jens Kunstmann, Alexey Chernikov, Daniel A. Chenet, Yu-Meng You, XiaoXiao Zhang, Pinshane Y. Huang, Timothy C. Berkelbach, Lei Wang, Fan Zhang, Mark S. Hybertsen, David A. Muller, David R. Reichman, Tony F. Heinz, and James C. Hone. Tailoring the electronic structure in bilayer molybdenum disulfide via interlayer twist. *Nano Letters*, 14(7):3869–3875, 2014. PMID: 24933687.

[83] Sachin M Shinde, Krishna P Dhakal, Xiang Chen, Won Seok Yun, JaeDong Lee, Hyunmin Kim, and Jong-Hyun Ahn. Stacking-controllable interlayer coupling and symmetric configuration of multilayered MoS_2. *Npg Asia Materials*, 10:e468, 2018.

[84] X. Zhang, W. P. Han, J. B. Wu, S. Milana, Y. Lu, Q. Q. Li, A. C. Ferrari, and P. H. Tan. Raman spectroscopy of shear and layer breathing modes in multilayer MoS_2. *Phys. Rev. B*, 87:115413, Mar 2013.

[85] Arend M. van der Zande, Pinshane Y. Huang, Daniel A. Chenet, Timothy C. Berkelbach, YuMeng You, Gwan-Hyoung Lee, Tony F. Heinz, David R. Reichman, David A. Muller, and James C. Hone. Grains and grain boundaries in highly crystalline monolayer molybdenum disulphide. *Nature Materials*, 12:554, 2013.

[86] Rebeca Ribeiro-Palau, Changjian Zhang, Kenji Watanabe, Takashi Taniguchi, James Hone, and Cory R. Dean. Twistable electronics with dynamically rotatable heterostructures. *arXiv*, 2018.

[87] D. E. Aspnes and A. A. Studna. Dielectric functions and optical parameters of Si, Ge, GaP, GaAs, GaSb, InP, InAs, and InSb from 1.5 to 6.0 ev. *Phys. Rev. B*, 27:985–1009, Jan 1983.

[88] I. H. Malitson. Interspecimen comparison of the refractive index of fused silica. *J. Opt. Soc. Am.*, 55(10):1205–1209, Oct 1965.

[89] C.Z. Tan. Determination of refractive index of silica glass for infrared wavelengths by ir spectroscopy. *Journal of Non-Crystalline Solids*, 223(1):158 – 163, 1998.

[90] Hiroshi Shioyama. The interactions of two chemical species in the interlayer spacing of graphite. *Synthetic Metals*, 114(1):1 – 15, 2000.

[91] Aleksandra B. Djurišić and E. Herbert Li. Optical properties of graphite. *Journal of Applied Physics*, 85(10):7404–7410, 1999.

[92] Gerrit A. Luinstra and Endres Borchardt. *Material Properties of Poly(Propylene Carbonates)*, volume 245, pages 29–48. Jan 1970.